ABSTRACT

Title of dissertation: The Optical Response of Strongly Coupled Quantum Dot- Metal Nanoparticle Hybrid Systems

Ryan Domenick Artuso, Doctor of Philosophy, 2012

Dissertation directed by: Dr. Garnett W. Bryant
National Institute of Standards and Technology

In this thesis, we study, theoretically, hybrid systems composed of semiconducting quantum dots (SQDs) and metallic nanoparticles (MNPs) which are coupled by means of an applied optical field. Systems composed of SQDs and MNPs have recently been a very active area of research. Such structures are considered to be viable candidates for use in nanodevices in quantum information and nanoscale excitation transfer. The goal of this thesis is to investigate the interactions of the constituent particles and predict the hybrid response of SQD/MNP systems.

We first study a single SQD coupled to a spherical MNP, and explore the relationship between the size of the constituents and the response of the system. We identify four distinct regimes of behavior in the strong field limit that each exhibit novel properties, namely, the Fano regime, exciton induced transparency, suppression and bistability. In chapter 3, we will explore these four regimes in detail and set bounds on each.

In chapter 4, we then show that the response of the system can be tailored by

engineering metal nanoparticle shape and the exciton resonance of SQDs to control the local-fields that couple the MNPs and SQDs. We identify regimes where dark modes and higher order multipolar modes can influence hybrid response. External fields do not directly drive MNP dark modes, so SQD/MNP coupling is dominated by the local induced coupling, providing a situation in which the induced self-interaction could be probed using near field techniques.

Finally, we consider a system of two SQDs coupled to a MNP. In particular, we identify and address issues in modeling the system using a semiclassical approach, which can lead to unstable and chaotic behavior in a strong SQD-SQD coupling regime. When we model the system using a more quantum mechanical approach, this chaotic regime is absent. Finally, we compare the two models on a system with a strong plasmon-mediated interaction between the SQDs and a weak direct interaction between them.

The Optical Response of Strongly Coupled Quantum Dot- Metal Nanoparticle Hybrid Systems

by

Ryan Domenick Artuso

Dissertation submitted to the Faculty of the Graduate School of the
University of Maryland, College Park in partial fulfillment
of the requirements for the degree of
Doctor of Philosophy
2012

Advisory Committee:
Doctor Garnett W. Bryant, Advisor
Professor Christopher J. Lobb, Chair
Doctor Eite Tiesinga
Professor Mario Dagenais
Professor Jeremy N. Munday

Acknowledgments

I would like to thank my advisor Garnett Bryant for his guidance and support, and for the opportunities he has given me. I would also like to thank the committee members for taking time from their busy schedules to read and review my work, and for their invaluable feedback. I'd also like to acknowledge our collaborators Javier Aizpurua and Aitzol Garcia-Etxarri for their help and excellent discussions. Finally, I'd like to thank Sarah Roosa for all her help, support, and encouragement.

Table of Contents

List of Figures

Chapter 1

Background and Motivation

1.1 Introduction

On December 29, 1959, Richard Feynman gave his now famous talk "There's Plenty of Room at the Bottom" at the APS annual meeting at the California Institute of Technology [1]. He spoke of the possibilities that miniaturization could bring to data storage, atomic and molecular manipulation and synthesis, and even nanomachines and nanorobotics. He challenged scientists of the day to improve upon the 1 nm resolution size of the scanning electron microscope (SEM). He also made the prediction that a single bit of information could someday be stored with the use of only 100 atoms, meaning that less than 1000 atoms would be needed to store a single alphanumeric character in 8-bit binary.

The scanning tunneling microscope (STM) was developed by Binnig and Rohrer in 1981 [2] with a resolution size approximately ten times smaller than that of an SEM. By the end of the decade, Eigler and Schweizer [3] used an STM to demonstrate a single atom manipulation technique that allowed them to write out "IBM" using letters that were approximating 5 nm in height, and all three letters consisted of only 35 atoms, surpassing even Feynman's bold prediction. With this not so humble beginning, the advent of nanotechnology truly began.

Nanotechnology is more than just the imaging and manipulation of objects on a

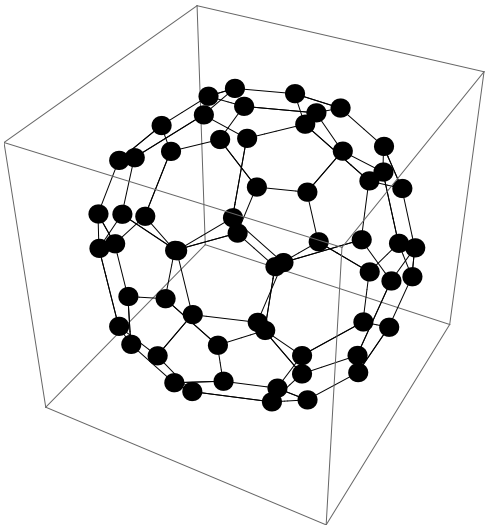

Figure 1.1: An artist's rendition of a C60 buckminsterfullerene. Each of the black dots represents a single carbon atom. Graphic generated using *Mathematica* software.

nanometer scale. Also included under this broad heading is the development of new, novel, nanoscale structures and materials, which due to their size and composition can possess unique properties. In 1985, Kroto, et. al. discovered C60 buckminsterfullerene, a molecule consisting solely of 60 carbon atoms with each atom bound to three others and forming a spherical shell [4] (see Figure 1.1). This pattern of bonding forms a structure of pentagons and hexagons that alternate throughout the object in a familiar soccer ball pattern. This molecule turned out to be just one member in a larger family of molecules which are now known as fullerenes. The most common of the fullerenes are the buckyballs (which includes the aforementioned C60, as well as the similar structures C24, C28, C32, C36, C50, C70, etc [5]).

Another type of fullerene is the carbon nanotube [6]. These objects are the two-dimensional analog of buckyballs. A carbon nanotube has the same pattern

of carbon binding as the buckyballs, however, instead of having a spherical shape, they are rolled up in a cylinder- like a cigar. These nanotubes often have a diameter around 1 nm with a length that can reach a million times that, and contain millions of carbon atoms.

One thing that makes carbon nanotubes particularly interesting is that one dimension (the circumference of the cylinder) is very small and very quantum mechanical, and the other dimension (its length) is very large, reaching millimeter scales, i.e. the macroscopic world. So from the scale of a few atoms to that of a 30 cm long carbon nanotube, we can say that the study of nanoscale physics is the study of the boundary between classical and quantum mechanics.

1.2 Nanoparticles

The focus of this thesis will be hybrid systems made from semiconducting nanoparticles [7, 8] and metal nanoparticles [9, 10]. These systems can often exhibit characteristics of both the quantum and classical regimes. Furthermore, the boundary between classical and quantum can be defined by the particles, i.e. the semiconducting nanoparticles can behave more quantum mechanically and the metal nanoparticles can behave more classically. Such nanoparticles are objects typically $1-100$ nm in size, often approximately spherical in shape, and composed of atoms in the bulk form for the material rather than the highly ordered and hollow structure of the fullerenes. Nanoparticles can have novel properties due to their extremely small size. First, there can be confinement effects once the size of the nanoparticle

is on the order of the wavelength of its excitation energy. Second, as a particle is made increasingly small, the ratio of the number of surface atoms of the particle to those that make up the bulk grows larger. As such, surface effects can come to dominate the physics of a nanoparticle, whereas they might be ignored in a larger object of the same composition.

Metal nanoparticles (MNPs) are typically made of a single metal such as gold, silver or platinum. If an MNP has an oblong shape, like a rod or cylinder, with a length on the order of $10 - 1000\,\text{nm}$ then it is commonly known as a nanorod. If a nanorod has a nearly infinite length (on the order of $1\,\mu\text{m}$), it could then be considered as a nanowire.

A nanoparticle made out of a semiconductor material (most typically InAs, GaAs, ZnS, ZnSe, CdS, CdSe, CdTe, or HgS) is referred to as a semiconductor nanoparticle. If the size of a semiconductor nanoparticle is small enough to confine an electron in the conduction band and also a hole in the valence band, in all three spatial directions, it is known as a semiconducting quantum dot (SQD). If the nanorod or nanowire is made from a semiconducting material, then it would be a quantum wire and would have excitations that were confined in two of the three directions, while the excitations would be free to propagate in the third.

In this thesis, the metallic nanoparticles that we will consider will range in size from just a few nanometers to 100 nm or more. Metals of this size consist of very many electrons. Due to this, it will be valid to treat the MNPs we consider to be classical in nature. The SQDs that we will consider will be slightly smaller in size than the MNPs. However, the size of the SQD has little effect on how it is

modeled. Most important is the confinement of the electron inside the SQD, which requires the SQD to be modeled quantum mechanically.

1.3 Nanosuperstructures

A structure made from a few or many nanoscale objects is often called a nanosuperstructure [11, 12, 13]. Such a physical system could have unique properties, and they could be engineered to suit a particular task. Recent advances in nanoscience have already allowed for the construction and study of such nanosuperstructures. By using various combinations of the available building blocks (nanowires, semiconductor quantum dots, metal nanoparticles, biolinkers, etc.) to create hybrid molecules, novel physical phenomena may be explored. Such structures will allow the study of physics at the interface of classical and quantum mechanics and could provide the technology for a number of devices in the field of quantum information. These structures should allow for the physical transportation of excitations as well as the transportation of coherent states.

Experiments have already demonstrated the plausibility of creating and studying such superstructures. Recently, researchers have shown that using a lithographic process, it is possible to control the deposition of quantum dots near nanowires [14]. This two step process, one of which results in a polymer template, should make more complicated structures accessible in the near future.

Recently, hybrid structures consisting of a quantum dot and a metal nanoparticle joined by a biolinker have been assembled and studied [15]. Experimental

investigations have shown efficient exciton-plasmon-photon conversion and an enhanced emission rate with the coupling of a CdSe quantum dot to a silver nanowire [16, 17]. Furthermore, when coupled to elongated MNPs, the photoluminescence intensity of SQDs is enhanced in a polarization-selective way [18], and when coupled with a nano-optical Yagi Uda antenna the SQD emission can be made unidirectional [19].

Hybrid structures consisting of an SQD and an MNP are a very active area of research in theoretical physics [15, 20, 21, 22, 23, 24, 25, 26, 27, 28, 29, 30]. By coupling the broad continuous plasmonic response of the MNP to the discrete excitons of the SQD, these structures allow the study of systems at the interface between classical and quantum physics. Furthermore, such structures could allow for the directed nanoscale transmission of information and excitations.

In this thesis, we will examine the physics of nanohybrid molecules, in particular those formed with metallic nanoparticles and semiconductor quantum dots. We hope to learn how the presence of a nearby SQD affects the response of an MNP. The MNP, with its ability to enhance local fields, will certainly have a large effect on a nearby quantum dot. We will study how the behavior of these nanoparticles changes when they are combined in hybrid structures in Chapters 3 and 4 of this thesis.

1.4 Transmission of Quantum Information

Once we allow for systems consisting of more than one nanoparticle, we must then consider how excitations are transferred between nanoparticles. The nanoscale transmission of quantum information and excitations between qubits for quantum communication, quantum computing and quantum measurement will require transfer where the quantum character of the information can be maintained.

At submicrometer distances, this means directed transmission must be carried out with better than wavelength scale resolution. One possible solution to this limitation is coupling qubits, for example in quantum dots, to plasmonic structures. It has been predicted that below the diffraction limit, highly efficient directed energy transfer over plasmonic wires consisting of chains of closely spaced metal nanoparticles could be achieved [31]. And at larger distances, strong, coherent coupling between emitters should be possible by means of guided plasmons that are evanescently coupled with a nearby dielectric waveguide[32]. Furthermore, it has been predicted that large entanglement, either spontaneously formed or in a continuously driven steady state, would be possible between qubits coupled to a plasmonic waveguide over distances exceeding a wavelength [33].

Several recent experiments have already shown very promising results in these structures. It has been shown that quantum coherence can survive in plasmonic structures, such as the transportation of entangled photons by surface plasmons [34] and the energy-time entanglement of a pair of photons following a photon-plasmon-photon conversion [35]. Furthermore, it has been demonstrated that during plasmon

propagation in metallic waveguides, losses appear to follow a linear, uncorrelated Markovian model of damping at the single quanta level, showing the quantum regime of plasmonics is realistic [36]. In related work, the quantum statistics of the light from a quantum emitter (in this case the color center of a nanodiamond) was shown to be preserved after conversion to plasmons and propagation in a polycrystalline gold film [37].

To exploit this paradigm for quantum, nanoscale communication, one must understand how metallic nanoparticles act as nanoantennas and nanoguides. One must understand the coupling between dots and plasmons in metallic nanoparticles. One must also understand how dot-to-dot quantum communication is modified by transfer via plasmons. Finally, one must understand how transfer is further modified if the metal nanoparticles are small and quantum effects can influence their response. To this end, we will consider systems in which the interaction between two spatially separated quantum dots is mediated by plasmons. This is the subject of Chapter 5.

The layout of the thesis is as follows. In Chapter 2, we discuss how we will be modeling the MNP and SQD as physical objects, and then we review the necessary physics and math that we will need to model the interacting system. We then examine some toy models to highlight some of the technical issues involved in the study of these systems and to illustrate the manner in which modeling was done for the work presented in this thesis. In Chapter 3, we model a realistic hybrid system consisting of an SQD coupled to a nearly spherical MNP. The two particles are driven by an oscillating electric field which in turn causes a dipole-dipole coupling. We will examine the optical response of the system in both the weak field regime

and in the strong field regime. Furthermore, we will discover four distinct regimes of behavior that depend on the strength of the SQD-MNP coupling, as we first reported in [21] and expanded upon in [22]. In Chapter 4, we will see how the dependence of local field enhancement strength on MNP shape could be exploited to engineer MNP-SQD hybrids that are biased towards a desired type of hybrid response. These results were first reported by us in [38]. In Chapter 5, we look beyond two particle MNP-SQD systems and look at the ways in which we can model a more complicated SQD-MNP-SQD system. Finally, in Chapter 6, I present my conclusions and briefly discuss the outlook and future work to be done to further our knowledge on these and similar systems.

Chapter 2

Tools and Toys

The system we wish to study consists of an SQD and an MNP separated by some distance with both particles subject to an applied optical field (as shown in Figure 2.1). We imagine that both particles have resonances near the energy of the applied field, and we will then model how the presence of the one effects the response of the other. To this end, we will describe techniques needed to model hybrid nanoparticle systems. Although we are focused on systems consisting of MNPs and SQDs, much of what will be discussed here is applicable to a much broader group of systems, especially those that operate in the visible or near-visible spectrum and in which losses and decoherence must be accounted for.

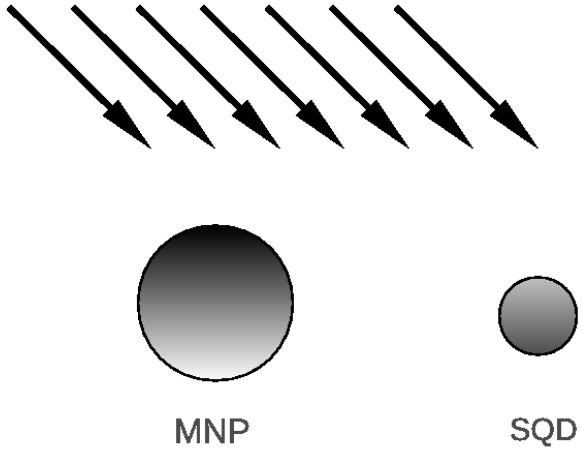

Figure 2.1: An MNP and an SQD subject to an applied optical field.

We begin this chapter with brief descriptions of MNPs. We then proceed to

model their plasmonic resonances using a Drude model, and we then show how to use experimental data to build a response function. We then discuss SQDs and confinement effects, and show how SQDs can be treated like atoms. In the next section, we look at open quantum systems. In order to study our MNP-SQD system, we will need to account for the interaction of our system with its environment. With this as motivation we introduce the density matrix formalism of quantum mechanics. We next concern ourselves with the interaction of light and matter in order to better understand the interaction of the SQD with the field. We develop the dynamical equations that govern the time evolution of the system. After a first attempt to model the interaction, we see that allowing for spontaneous emission is necessary for the interaction. We then build a quantum theory of open systems in the Lindblad formalism. The use of the theory is illustrated with a simple system prior to it being generalized for the quantum optics regime. We then use the tools we have just developed to model a system consisting of an atom in an oscillating electromagnetic field. Finally, the chapter is concluded with a discussion on how numerical calculations were performed to evaluate the set of dynamical equations we study.

2.1 Metallic Nanoparticles

Although metallic nanoparticles have been used since ancient times to color glazed pottery and stained glass, it wasn't until Faraday's work with gold particles in an aqueous solution in the 1850s [39] that this effect was attributed to the particles'

small size. Although Farady was the first to show that these small particles of gold could have very different optical properties than those of bulk gold, a full understanding of the process was not presented until 1908 when Mie published his seminal paper on the scattering of such small objects [40]. This scattering process later became known as Mie scattering. By considering the scattering of an incident planewave of light off of a sphere, Mie was able find a series solution to Maxwell's equations in the regime where the particle's size is on the same order as in the incident light. This is in contrast to Rayleigh scattering which assumes the particle to be much smaller than the wavelength of incident light [41].

A key feature of MNPs is that they can support surface plasmons. Surface plasmons are the quasi-particle of coherent oscillations of electron density on the surface of a metal and were originally studied by Ritchie on the surface of thin films [42]. On a film or other bulk material, the plasmons propagate along the surface when excited by incident radiation via a coupler, e.g. a grating. In an MNP however, because the size of the metal is smaller than the wavelength of the incident light (often by an order of magnitude or more), the plasmons are unable to propagate and are thus confined. Because of this confinement, the response of a MNP is highly dependent on the wavelength of incident light. For a spherical gold MNP, the response has a maximal peak in the vicinity of $2.3 - 2.5\,\mathrm{eV}$. This resonance is the dipolar plasmon peak. This resonance causes a build up of charge on the surface of the particle, enhancing not only the scattering and absorption of the incident light, but also producing a dipolar response field (in the small particle limit, in general higher orders of the multipolar expansion are also present). This

dipole field can display very large enhancement of the incident field near the surface of the MNP.

2.1.1 Modeling the MNP response to a planewave

To understand how an MNP reacts to an applied optical field, we start with a simple model. Consider a spherical MNP, of radius a, and we imagine that this small metallic ball is being driven by an electromagnetic field. We'll take our driving field to be an electromagnetic wave propagating in the $\hat{x}$–direction, with the electric field in the $\hat{z}$–direction. We assume that the particle is solid, homogeneous and isotropic. Furthermore, we will assume that our particle is a linear dielectric, i.e. $\mathbf{D} = \epsilon\mathbf{E}$. We place the center of our sphere at the origin of our coordinate system as shown in Figure 2.2.

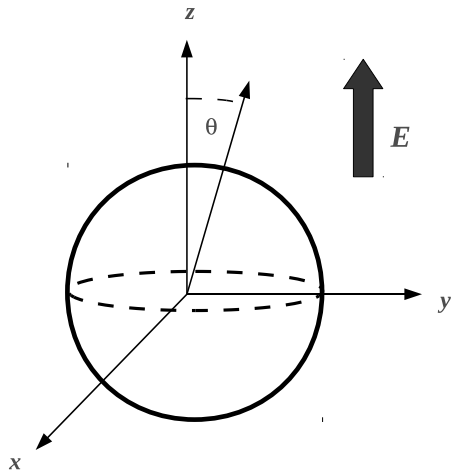

Figure 2.2: Spherical MNP in an applied driving field.

Since our particle is very small, on the order of 10 nm or so, much smaller than the wavelength of visible light (390–750 nm), we assume that the field, at any particular moment in time, is approximately constant throughout the MNP. This 'quasi-static' approximation allows us to ignore retardation effects. Thus, we must calculate the electric field produced by a spherical dielectric particle, $\mathbf{E}_{response}(x, y, z)$, by a constant applied electric field, $\mathbf{E}_{applied}(x, y, z) = E_0\hat{z}$.

Now, if our particle is not a magnetic material, and we are using the quasi-static approximation, we solve Gauss' law in the absence of charges, $\boldsymbol{\nabla} \cdot \epsilon\mathbf{E} = 0$. To do so, we first define the scalar potential, $\mathcal{V}$, such that $\mathbf{E} = -\boldsymbol{\nabla}\mathcal{V}$. In terms of $\mathcal{V}$ then, we have $\boldsymbol{\nabla}^2\mathcal{V} = 0$, which is simply Laplace's equation. Solving Laplace's equation in this case is best done in spherical coordinates. The solution to Laplace's equations with azimuthal symmetry is a sum of Legendre polynomials [43],

$$\mathcal{V}(r, \theta) = \sum_{n=0}^{\infty} \left[A_n r^n + B_n \left(\frac{1}{r} \right)^{n+1} \right] P_n(\cos\theta) \tag{2.1}$$

where the coefficients A_n and B_n are determined by the boundary conditions. Therefore, we can write our solution like this:

$$\mathcal{V} = \begin{cases} \sum_{n=0}^{\infty} \left[A_n \left(\frac{r}{a} \right)^n + B_n \left(\frac{a}{r} \right)^{n+1} \right] P_n(\cos\theta) & \text{for } \; r < a \; , \\ \sum_{n=0}^{\infty} \left[A'_n \left(\frac{r}{a} \right)^n + B'_n \left(\frac{a}{r} \right)^{n+1} \right] P_n(\cos\theta) & \text{for } \; r \geqslant a. \end{cases} \tag{2.2}$$

Inside the MNP, nonzero values for the B_n would lead to an unphysical infinite potential at $r = 0$, so we can take $B_n = 0$ for all n. We also require that far from the MNP, the potential approaches that of the applied field, $\mathbf{E}_{applied}$, so $\mathcal{V} \to -E_0 r\cos\theta$ for $r >> a$. Therefore, for $r \geqslant a$ we must have $A'_1 = -aE_0$ and, $A'_n = 0$ for $n \neq 1$.

Our potential is now

$$\mathcal{V} = \begin{cases} \sum_{n=0}^{\infty} A_n \left(\frac{r}{a}\right)^n P_n(\cos\theta) & \text{for } \; r < a \; , \\ \sum_{n=0}^{\infty} B'_n \left(\frac{a}{r}\right)^{n+1} P_n(\cos\theta) - E_0 r\cos\theta & \text{for } \; r \geqslant a. \end{cases} \tag{2.3}$$

Further boundary conditions that must be met are the continuity of $\mathcal{V}$ and the normal component of $\mathbf{D}$ at the dielectric interface. From the first we have

$$\sum_{n=0}^{\infty} A_n P_n(\cos\theta) = \sum_{n=0}^{\infty} B'_n P_n(\cos\theta) - E_0 a\cos\theta. \tag{2.4}$$

In regards to the latter, the normal component of D at the MNP surface is proportional to $\frac{\partial \mathcal{V}}{\partial r}$. So, we must have $\frac{\partial \mathcal{V}}{\partial r}\big|_{outside} = \frac{\epsilon}{\epsilon_0}\frac{\partial \mathcal{V}}{\partial r}\big|_{inside}$, where ϵ is the dielectric constant of the material the MNP is composed of, and ϵ_0 is the vacuum dielectric constant. From this we can write

$$\frac{\epsilon}{\epsilon_0}\sum_{n=1}^{\infty} nA_n \frac{1}{a} P_n(\cos\theta) = \sum_{n=1}^{\infty} -(n+1)B'_n \frac{1}{a} P_n(\cos\theta) - E_0\cos\theta. \tag{2.5}$$

Using the orthogonality of the Legendre polynomials, our boundary conditions term by term become

$$\begin{aligned} A_0 &= B'_0 \\ A_1 &= B'_1 - E_0 a \\ A_n &= B'_n \, , \quad n > 1 \end{aligned}$$

and

$$\begin{aligned} \frac{\epsilon}{\epsilon_0} A_1 &= -2B'_1 - E_0 a \\ n\frac{\epsilon}{\epsilon_0} A_n &= -(n+1)B'_n \, , \quad n > 1 \end{aligned}$$

Since A_0 is just the value of the potential at the center of the MNP, we can arbitrarily set this to zero. Therefore, we can finally write

$$\begin{aligned} A_0 =& B_0' = 0 \\ A_1 =& \frac{-3\epsilon_0}{2\epsilon_0 + \epsilon} E_0 a \\ B_1' =& \frac{\epsilon - \epsilon_0}{2\epsilon_0 + \epsilon} E_0 a \\ \frac{n+1}{n} A_n =& -\frac{\epsilon}{\epsilon_0} A_n \,, \qquad n > 1 \end{aligned}$$

If we assume that ϵ is complex, then the relation $\frac{n+1}{n} = -\frac{\epsilon}{\epsilon_0}$ does not hold for any n. Therefore, we must have $A_n = 0$ for $n > 1$. Thus our solution is

$$\mathcal{V} = \begin{cases} -\frac{1}{\epsilon_{eff}} E_0 r \cos\theta & \text{for } \; r < a \;, \\ \gamma a^3 E_0 \frac{1}{r^2} \cos\theta - E_0 r \cos\theta & \text{for } \; r \geqslant a, \end{cases} \tag{2.6}$$

where we have defined $\epsilon_{eff} \equiv \frac{2\epsilon_0 + \epsilon}{3\epsilon_0}$ and $\gamma \equiv \frac{\epsilon - \epsilon_0}{2\epsilon_0 + \epsilon}$.

We now calculate the total electric field, $\mathbf{E} = \mathbf{E}_{applied} + \mathbf{E}_{response}$,

$$\mathbf{E} = \begin{cases} \frac{1}{\epsilon_{eff}} E_0 \left(\cos\theta \; \hat{r} - \sin\theta \; \hat{\theta} \right) & \text{for } \; r < a \;, \\ \left(1 + 2\frac{\gamma a^3}{r^3} \right) E_0 \cos\theta \; \hat{r} + \left(\frac{\gamma a^3}{r^3} - 1 \right) E_0 \sin\theta \; \hat{\theta} & \text{for } \; r \geqslant a. \end{cases} \tag{2.7}$$

which can be rewritten

$$\mathbf{E} = \begin{cases} \frac{1}{\epsilon_{eff}} E_0 \hat{z} & \text{for } \; r < a \;, \\ 2\frac{\gamma a^3}{r^3} E_0 \cos\theta \; \hat{r} + \frac{\gamma a^3}{r^3} E_0 \sin\theta \; \hat{\theta} + E_0 \hat{z} & \text{for } \; r \geqslant a. \end{cases} \tag{2.8}$$

with use of the identity $\hat{z} = \cos\theta \; \hat{r} - \sin\theta \; \hat{\theta}$ in spherical coordinates. In this form, it is easy to see that the total field inside the MNP is spatially constant, and equal to the value of the applied electric field at the center of the MNP, multiplied by a

'screening' factor, $\frac{1}{\epsilon_{eff}}$. Outside the MNP, the total electric field easily splits into $\mathbf{E}_{response} + \mathbf{E}_{applied}$, and we see that $\mathbf{E}_{response}$ in this region is

$$\mathbf{E}_{response}(r \geqslant a) = 2\frac{\gamma a^3}{r^3} E_0 \cos\theta\ \hat{r} + \frac{\gamma a^3}{r^3} E_0 \sin\theta\ \hat{\theta}. \tag{2.9}$$

We can rewrite this as

$$\begin{aligned}
\mathbf{E}_{response}(r \geqslant a) =& \frac{\gamma a^3}{r^3} E_0 \left(2\cos\theta\ \hat{r} + \sin\theta\ \hat{\theta}\right) \\
=& \frac{\gamma a^3}{r^3} E_0 \left(2\cos\theta\ \hat{r} + \sin\theta\ \hat{\theta} + \cos\theta\ \hat{r} - \cos\theta\ \hat{r}\right) \\
=& \frac{\gamma a^3}{r^3} E_0 \left(3\cos\theta\ \hat{r} - \ \hat{z}\right) \\
=& \frac{1}{r^3}\left(3(\boldsymbol{\mu}_{\mathrm{MNP}} \cdot \hat{r}) - \boldsymbol{\mu}_{\mathrm{MNP}}\right)
\end{aligned} \tag{2.10}$$

where we have defined $\boldsymbol{\mu}_{\mathrm{MNP}} = \gamma a^3 \mathbf{E}_{applied}$. The astute reader will recognize that equation (2.10) is identical to the field produced by a dipole located at the origin, with dipole moment equal to $\boldsymbol{\mu}_{\mathrm{MNP}}$. This means the applied field induces a polarization in the MNP, equal to $\gamma a^3 \mathbf{E}_{applied}$.

Therefore, we have shown that in this limit, for a particular driving field, the field inside the MNP is determined by the screening factor $\frac{1}{\epsilon_{eff}}$. Outside of the MNP, for a particular driving field and particle radius, the response is determined by γ. Thus when we speak of the response of an MNP, what we really need to know are these two functions. Because ϵ_{eff} determines the field inside the MNP, we can also say that it determines the absorption of the MNP. Likewise, since γ determines the field external to the MNP, it determines the scattering of the MNP.

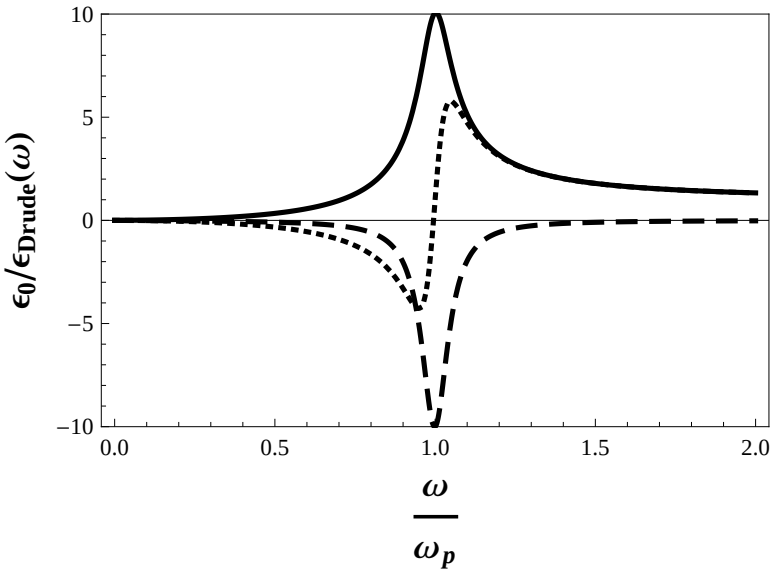

Figure 2.3: The magnitude (solid line), the real part (dotted line) and the imaginary part (dashed line) of $\frac{\epsilon_0}{\epsilon_{\text{Drude}}}$ plotted as a function of $\frac{\omega}{\omega_p}$ with $\Gamma = 0.1\,\omega_p$. The plasmon peak (the peak in the magnitude of $\frac{\epsilon_0}{\epsilon_{\text{Drude}}}$) appears at a dip in the imaginary part at $\frac{\omega}{\omega_p} = 1$, where the real part crosses zero.

2.1.2 The Drude Model

Both γ and ϵ_{eff} are determined by the dielectric of the MNP, ϵ. What makes this particularly interesting is that ϵ is a function of the driving field frequency ω. A well-known way to model this dependence of $\epsilon(\omega)$ is with a Drude model for metal [44],

$$\begin{aligned}\frac{\epsilon_{\text{Drude}}(\omega)}{\epsilon_0} &= 1 - \frac{\omega_p^2}{\omega^2 + i\omega\Gamma} \\ &= 1 - \frac{\omega_p^2}{\omega^2 + \Gamma^2} + i\frac{\Gamma\omega_p^2}{\omega(\omega^2 + \Gamma^2)}\end{aligned}$$

The bulk plasmon frequency, ω_p, is defined as $\omega_p = \sqrt{\frac{ne^2}{m_e\epsilon_0}}$, where e and m_e are the electron charge and mass respectively and n is the density of electrons in the metal. Damping in the model is accounted for by Γ which is related to the mean free path

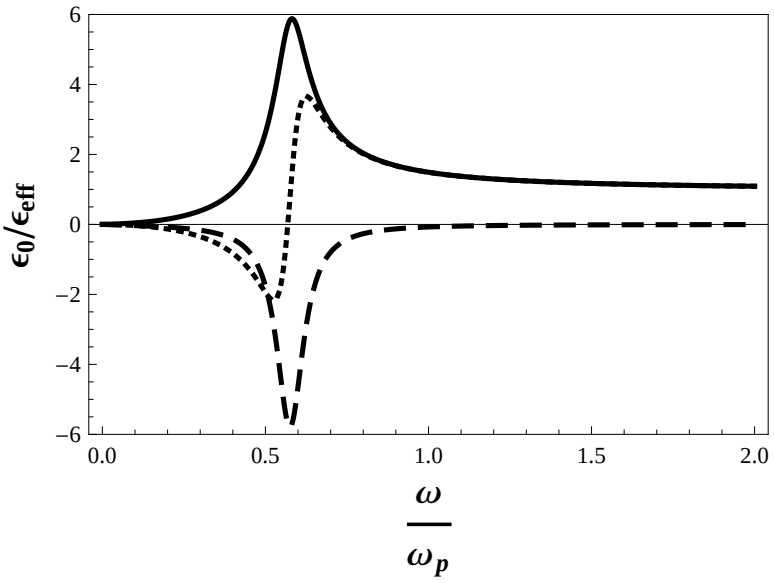

Figure 2.4: The magnitude (solid line), the real part (dotted line) and the imaginary part (dashed line) of $\frac{\epsilon_0}{\epsilon_{\text{eff}}}$ plotted as a function of $\frac{\omega}{\omega_p}$ with $\Gamma = 0.1\,\omega_p$. The plasmon peak (the peak in the magnitude of $\frac{\epsilon_0}{\epsilon_{\text{eff}}}$) is easily seen as a dip in the imaginary part near $\frac{\omega}{\omega_p} = 0.6$, where the real part crosses zero.

of the electrons in the metal and their Fermi velocity.

The Drude model is plotted in Figure 2.3. Shown are the real and imaginary parts of the dimensionless quantity $\frac{\epsilon_0}{\epsilon_{\text{Drude}}}$, plotted as a function of $\frac{\omega}{\omega_p}$. We have chosen the relaxation rate to be an order of magnitude less than the rate of plasmon oscillations, i.e. $\Gamma = 0.1\,\omega_p$. In the plot, we see that an electric field scaled by a factor of $\frac{\epsilon_0}{\epsilon_{\text{Drude}}}$, would have very large enhancement (about an order of magnitude) near $\omega = \omega_p$, where the magnitude of this quantity reaches a resonance peak.

We can now use the Drude model for $\epsilon(\omega)$ in order to model γ and $\frac{1}{\epsilon_{\text{eff}}}$. When we do, we see that the resonance peak in the response of both (see Figures 2.4 and 2.5) occurs at a lower frequency, near $\omega = 0.6\omega_p$, as opposed to that of $\frac{1}{\epsilon_{\text{Drude}}}$ which peaks at $\omega = \omega_p$. This is a general feature of MNPs, the plasmon peak of

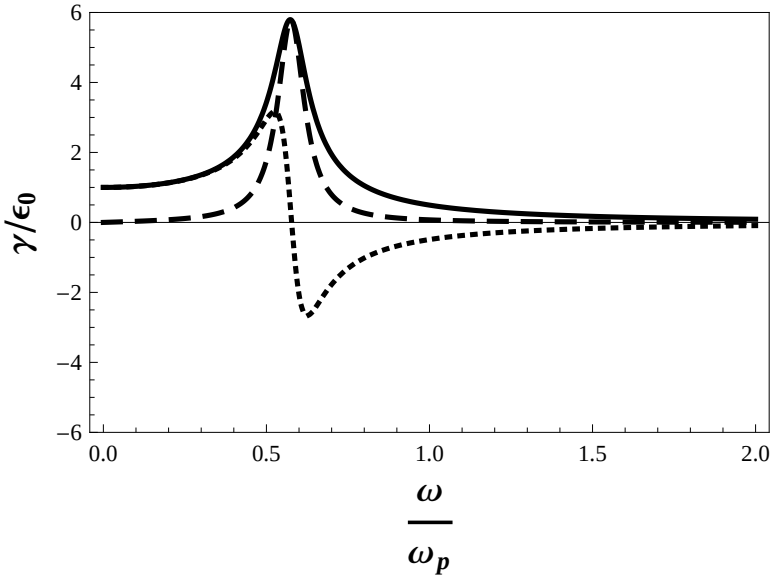

Figure 2.5: The magnitude (solid line), the real part (dotted line) and the imaginary part (dashed line) of $\frac{\gamma}{\epsilon_0}$ plotted as a function of $\frac{\omega}{\omega_p}$ with $\Gamma = 0.1\,\omega_p$. The plasmon peak (the peak in the magnitude of $\frac{\gamma}{\epsilon_0}$) is easily seen as a dip in the imaginary part near $\frac{\omega}{\omega_p} = 0.6$, where the real part crosses zero.

an MNP will appear at a lower energy than the bulk plasmon of the same material. In fact, it can be shown [44] that for ellipsoidal MNPs, the plasmon peak occurs at $\omega = \sqrt{L}\,\omega_p$, where L is a geometrical constant that is easily calculated. For a sphere (which itself is an ellipsoidal), this geometric factor is $L = \frac{1}{3}$, which would mean that the resonance should be at $\omega = 0.58\,\omega_p$, in good agreement with Figures 2.4 and 2.5.

2.1.3 Numerical Methods

The Drude model is very handy at approximating the response of simple, free electron-like metals. To go beyond the Drude model and produce more accurate results specific to a particular metal, we can use experimental data of the dielectric

constant of bulk metals for various values of the driving frequency. Once this data is obtained for a particular metal, we can interpolate the data to extend the domain into the regions between data points, to produce a continuous function, $\epsilon(\omega)$. Once $\epsilon(\omega)$ is known, it is a simple matter to calculate γ and ϵ_{eff}.

To model structures more complicated than just spheres, solving Maxwell's equations in closed form in order to calculate γ and ϵ_{eff} is often not possible. To calculate the optical response of such structures, numerical methods of solving Maxwell's equations must be employed. Numerical approaches commonly used include the finite element method (FEM) [45], finite difference time domain method (FDTD) [46], and boundary element method (BEM) [47], amongst many others.

In this thesis, when modeling the response of nanorods, we will use the BEM, which has the advantage that it requires less computing resources than volume-discretization methods such as the FEM or the FDTD. The BEM begins with the surfaces that form the interface between regions of differing dielectric materials. Each surface is divided up into small sections by means of a grid. Solutions to Maxwell's equations inside each region impose boundary conditions on the interface surfaces in terms of surface charges and currents. The surface charges and currents for each element are then matched in a self-consistent way by inverting a very large matrix. Once the surface charges and currents are known, Green's functions allow for the solution to be propagated away from the surface to any point of interest.

Actual numerical calculations performed for the research presented in this thesis were done using software written by our collaborators at the Donostia International Physics Center in San Sebastian, Spain. The software, written in C++,

consists of two main programs, the first calculates the response due to a planewave and the second does the same for a dipole. In both programs, the user specifies the locations of boundaries between materials of differing dielectric constant. The location where the resultant field should be calculated is also input. Additionally, the dipole program requires the location and direction of the test dipole that will induce the response. Various parameters control the accuracy (and thus run-time) of the result. Once the BEM software has calculated the response, the fields can then be used in our models.

2.1.4 Modeling the MNP Response to a Dipole Source

A planewave is not the only type of electromagnetic radiation that our MNP will be subject to. The field emitted by the SQD will resemble that of a dipole. To calculate the response of the MNP to a dipole field, we could proceed as before, by solving Maxwell's equations in the quasi-static limit. However, the response can also be quickly approximated using our previous results. If we assume that our MNP is very small and sufficiently far away from the dipole, then the electric field has a small variation over the volume of the MNP. If we assume that the field is approximately constant, then we can approximate the total field inside the MNP to be $E_{\text{dipole}}/\epsilon_{\text{eff}}$, where E_{dipole} is the value of the dipole field at the location of the center of the MNP. Likewise, the response field outside the MNP will scale with γ.

In making this approximation, we are only allowing the MNP to have a dipole response to this dipolar field, but higher order modes in the MNP would be excited

by the dipole. However, in cases where we need to account for these additional modes, and go beyond a dipole limit, we can do so by using a multipole expansion or by the BEM, as we will discuss in Chapter 4.

2.2 Semiconducting Quantum Dots

We begin our examination of the SQD by first looking at semiconductors. A semiconductor is characterized by the existence of a band gap in its allowed electron energy levels. Physically, the band gap is the difference in energy between the valence and conduction electrons. When energy is added to the semiconducting material, for example when an electric field is applied across it, electrons from the valence band may move up into the conduction band and can flow through the material, i.e. they conduct. However, as a semiconductor is made increasingly small, conduction band electrons increasingly find less room in which to flow. Thus the electrons become confined.

Since we are imagining that our nanoparticle is very small, we can model the conduction band as an electron trapped in an infinite square well. Then the electron's wavefunction for the state with quantum numbers (n_x, n_y, n_z) is

$$\Psi(n_x, n_y, n_z) = \sqrt{\frac{8}{l_x\, l_y\, l_z}}\ \sin\frac{n_x \pi x}{l_x}\ \sin\frac{n_y \pi y}{l_y}\ \sin\frac{n_z \pi z}{l_z} \tag{2.11}$$

with energy

$$E(n_x, n_y, n_z) = \frac{\pi^2 \hbar^2}{2m}\left[\left(\frac{n_x}{l_x}\right)^2 + \left(\frac{n_y}{l_y}\right)^2 + \left(\frac{n_z}{l_z}\right)^2\right]. \tag{2.12}$$

Thus we see that as $l_x\,, l_y\,,$ and l_z are made ever smaller, the spacing between the energy levels increases (this holds true regardless of particle shape). This allows

for us to create a quantum dot in which only the lowest energy level is effectively reachable, with all higher energy levels beyond typical electron energies for the system. For example, if we irradiate a quantum dot with a field that is on resonance with the energy gap between the valence and first conduction band state, then once the first electron is knocked into the conduction band, ignoring the degeneracy of the electron spin, no further electrons will be excited since the energy gap between the valence band and the second conduction band state will be far detuned from wavelength of the applied field.

Once we have a single electron in the conduction band, there is a hole that is left behind in the valence band, which is also quantized, where the electron once was. Since the electron has negative charge, the hole has a positive charge and thus they are attracted to one another and can form a bound state. This bound pair of an electron and its hole is called an exciton. As this is an attractive force, it contributes a negative energy to the energy of the excited state. Additionally, there is an effective confinement energy for both the electron and the hole. Thus we have three sources of energy contributing to the exciton energy, the band gap, the confinement and the electron-hole coulomb interaction.

To model an SQD, we assume that it possesses some excitonic energy level, which is determined by its size and the actual material it is composed of. This energy is typically in the range of $1-4\,\mathrm{eV}$ which makes the quantum dot an excellent candidate to study in quantum optics. Furthermore, we will assume that any laser or source of radiation that our SQD is in contact with will be very close in resonance to this exciton energy. As long as that is the case, we assume that higher energy

levels are not excited and we effectively have a two level quantum system, i.e. there is an exciton, or there is not.

2.3 Quantum Open Systems

In order to study realistic quantum systems, it is often necessary to restrict the size of the system under study. In our case, we will be modeling the interactions of the MNP and SQD, as they respond to the applied electric field, and to each other. However, there are other interactions that would have an effect on our system if such a system were studied in a lab. Both the MNP and SQD would have phonon modes that could influence behavior. Most importantly, the exciton has a finite lifetime. It spontaneously decays. In order to account for these effects, all other physical interactions and processes that are not included in our system are then given as properties of a reservoir or a "bath". We will define an open quantum system to be a quantum system that is found to interact with several other quantum systems, which we will call the baths. A quantum system which is not influenced by any outside forces is said to be closed.

One can always take an open system and effectively "close" it by considering a larger system, consisting of the original system along with its bath, as well as anything that influences that bath, and continuing that process until the system is closed. However, this is most often not practical. Typically, the system we wish to study, an atom for example, will be influenced by its environment through thermal, vibrational or radiative noise. Including all of the sources of noise in the dynamics

of our system could drastically increase the complexity of the calculation. Thus, we need to use techniques to handle open systems in a more reasonable manner.

When an open quantum system interacts with a bath, we will assume this to be a thermodynamically irreversible process. One effect of such a process on a quantum system is the loss of information. Specifically, it introduces decoherence into the system. To proceed further, we need to make clear the distinction between classical and quantum probabilities. To illustrate the difference, consider a simple spin-$\frac{1}{2}$ system. Let $|\uparrow\rangle_x$ and $|\downarrow\rangle_x$ be the spin up and spin down eigenvectors of the $\hat{x}$-direction spin projection operator, σ_x, and similarly define the basis vectors for σ_y and σ_z. If we initially prepare our system in the state $|\uparrow\rangle_z$, then we can write that state in terms of the x component spin eigenvectors as $|\uparrow\rangle_z = \frac{1}{\sqrt{2}}|\uparrow\rangle_x + \frac{1}{\sqrt{2}}|\downarrow\rangle_x$. Thus, in this case, a measurement of σ_z will always result in a value of $\frac{1}{2}$ (letting $\hbar = 1$), whereas a measurement of σ_x will yield $\frac{1}{2}$ or $-\frac{1}{2}$ with equal probability.

Now contrast that with the following. Suppose instead that we initially prepare our state as $|\uparrow\rangle_x$. Further suppose that our system has some probability to decay from $|\uparrow\rangle_x$ into $|\downarrow\rangle_x$, and let the rate of this transition be γ. Then, after a period time equal to $t_{\frac{1}{2}} = \frac{ln(2)}{\gamma}$ (called the half-life), there will be equal probability that a measurement of σ_x will yield $\frac{1}{2}$ or $-\frac{1}{2}$. We might be tempted to write the state of our system as $\frac{1}{\sqrt{2}}|\uparrow\rangle_x + \frac{1}{\sqrt{2}}|\downarrow\rangle_x$, like we did before. However, this would be incorrect. To see why, let's work in the σ_z basis, so we can write our initial state as $|\uparrow\rangle_x = \frac{1}{\sqrt{2}}|\uparrow\rangle_z + \frac{1}{\sqrt{2}}|\downarrow\rangle_z$ and spin down state as $|\downarrow\rangle_x = \frac{1}{\sqrt{2}}|\uparrow\rangle_z - \frac{1}{\sqrt{2}}|\downarrow\rangle_z$. Now, after a half-life of the initial state has passed, and the particle has equal probability to be in either of these two states, we ask what the result of a σ_z measurement would give.

If the particle is in the $|\uparrow\rangle_x$ state, which it is 50% of the time, then a measurement in the $\hat{z}$-direction yields $|\uparrow\rangle_z$ and $|\downarrow\rangle_z$ each with probability of $\frac{1}{2}$. On the other hand, if the particle is in the $|\downarrow\rangle_x$ state, which it is 50% of the time, then a measurement in the $\hat{z}$-direction will also yield $|\uparrow\rangle_z$ and $|\downarrow\rangle_z$ each with probability of $\frac{1}{2}$. Thus in this case, our system is equally likely to either spin up or spin down in both the $\hat{x}$ and $\hat{z}$ directions, as opposed the previous case, in which the spin of the system was uncertain in the $\hat{x}$ direction, but always spin up in $\hat{z}$.

In the previous example, the spontaneous decay from $|\uparrow\rangle_x$ into $|\downarrow\rangle_x$ introduces a classical uncertainty which is fundamentally different than the quantum mechanical uncertainty inherent between non-commuting operators (such as σ_x and σ_z). In fact, the final state of that system can not be written as a conventional wave function. We call such a state a mixed state, because it consists of a classical mixture of two quantum states. Conversely, if a state can be written as a single state vector, it is said to be pure. In order to properly handle such processes in a consistent way, we need to learn how to do quantum mechanics when mixed states are included, which will require a more complicated mathematical object to describe the state of our system. In the quantum mechanics of pure states, the state of the system is typically described as a vector. However, for an open system, we will see that the quantum state is most conveniently described as a matrix.

2.4 The Density Matrix

In the basic formulations of quantum mechanics, the state of the system under study is assumed to be a pure state, i.e., we may assume that our system can be fully described by a ket in our Hilbert space, namely, $|\Psi\rangle$, and the evolution of our state is governed by Schrödinger's Equation,

$$i\hbar\frac{\partial}{\partial t}|\Psi\rangle = \hat{\mathcal{H}}|\Psi\rangle . \tag{2.13}$$

Furthermore, if $\hat{A}$ is an observable, then the expectation value of $\hat{A}$ when our system is in the state $|\Psi\rangle$ can be calculated as

$$\langle\bar{A}\rangle = \left\langle\Psi\right|\hat{A}\left|\Psi\right\rangle . \tag{2.14}$$

If we expand $|\Psi\rangle$ in an orthonormal basis as $|\Psi\rangle = \sum_n c_n|\psi_n\rangle$, this becomes,

$$\langle\bar{A}\rangle = \sum_{n\,m} c_m^* c_n \left\langle\psi_m\right|\hat{A}\left|\psi_n\right\rangle = \sum_{n\,m} c_m^* c_n A_{mn}. \tag{2.15}$$

We now suppose, as we did in the previous section, that our system has some probability, p_1, to be in the state $|\Psi_1\rangle$ and a probability, p_2, to be in the state $|\Psi_2\rangle$, with $p_1 + p_2 = 1$, and $|\Psi_1\rangle$ and $|\Psi_2\rangle$ both separately satisfy (2.13). We can then calculate the expectation value of $\hat{A}$ as

$$\begin{aligned}\langle\bar{A}\rangle &= p_1\left\langle\Psi_1\right|\hat{A}\left|\Psi_1\right\rangle + p_2\left\langle\Psi_2\right|\hat{A}\left|\Psi_2\right\rangle \\ &= \sum_{n\,m}\left(p_1\big(c_m^{(1)}\big)^* c_n^{(1)} + p_2\big(c_m^{(2)}\big)^* c_n^{(2)}\right)A_{mn}\end{aligned}$$

where $|\Psi_1\rangle = \sum_n c_n^{(1)}|\psi_n\rangle$, and similarly for $|\Psi_2\rangle$. Since this holds for all $\hat{A}$, we can thus identify

$$p_1\big(c_m^{(1)}\big)^* c_n^{(1)} + p_2\big(c_m^{(2)}\big)^* c_n^{(2)}$$

as the object that allows us to calculate expectation values of mixed states.

We now extend this to include mixtures of more than two pure states. In doing so, we define the density matrix, ρ, in terms of its components as

$$\rho_{mn} = \sum_i p_i \left(c_m^{(i)}\right)^* c_n^{(i)} \tag{2.16}$$

where p_i is the probability that our system is in the pure state $|\Psi_i\rangle$, and the coefficients of our expansion are given by $|\Psi_i\rangle = \sum_j c_j^{(i)} |\psi_j\rangle$. Alternatively, we can also write this definition in matrix form as

$$\rho = \sum_i p_i |\Psi_i\rangle \langle\Psi_i| . \tag{2.17}$$

As a quick check to ensure that this definition is what we want, we calculate $\langle\bar{A}\rangle$ as the sum of expectation values of pure states, as follows,

$$\begin{aligned}
\langle\bar{A}\rangle &= \sum_i p_i \langle\bar{A}\rangle_i \\
&= \sum_i p_i \left\langle \Psi_i \middle| \hat{A} \middle| \Psi_i \right\rangle \\
&= \sum_{i\,m\,n} p_i \left(c_m^{(i)}\right)^* c_n^{(i)} A_{mn}.
\end{aligned}$$

Because of the cyclic property of the trace, we can also write this as,

$$\begin{aligned}
\langle\bar{A}\rangle &= Tr[\rho\hat{A}] \\
&= Tr\left[\sum_i p_i |\Psi_i\rangle \langle\Psi_i| \hat{A}\right] \\
&= \sum_i p_i \langle\Psi_i| \hat{A} |\Psi_i\rangle \ .
\end{aligned} \tag{2.18}$$

We now need to determine the time evolution of the density matrix. In order

to do so, lets calculate the quantity $\dot{\rho}$,

$$\begin{aligned}
\dot{\rho} &= \sum_i p_i \frac{\partial}{\partial t}\Big(\left|\Psi_i\right\rangle \left\langle\Psi_i\right| \Big) \\
&= \sum_i p_i \Big(\frac{\partial \left|\Psi_i\right\rangle}{\partial t} \left\langle\Psi_i\right| + \left|\Psi_i\right\rangle \frac{\partial \left\langle\Psi_i\right|}{\partial t} \Big) \\
&= -\frac{i}{\hbar} \sum_i p_i \Big(\hat{\mathcal{H}} \left|\Psi_i\right\rangle \left\langle\Psi_i\right| - \left|\Psi_i\right\rangle \left\langle\Psi_i\right| \hat{\mathcal{H}} \Big) \\
&= -\frac{i}{\hbar} \Big(\hat{\mathcal{H}}\rho - \rho\hat{\mathcal{H}} \Big)
\end{aligned}$$

or written in a more familiar form,

$$\dot{\rho} = -\frac{i}{\hbar}\Big[\hat{\mathcal{H}}, \rho\Big] \tag{2.19}$$

where $[\hat{A}, \hat{B}]$ is the commutator and we have used (2.13) and its Hermitian conjugate.

2.5 The Interaction of Light and Matter

We will now investigate the physical processes involved in the interaction of light and matter, which is central to the study of the behavior of the SQD in the presence of a field. We first consider the simplest system, that of a single two level "atom", isolated from all other matter, and subject to an oscillating electric field. We will assume that the electric field is spatially constant in the region of space in which our atom is located, thus we can write the field solely as a function of time, $E = E_0 \cos(\omega t + \phi)$, where ϕ is an arbitrary phase that we will typically take to be zero. Our Hamiltonian consists of three parts, the energy of the atomic system completely unperturbed, the energy inherent in the electric field and lastly

the interaction energy between the two. So we can write this as

$$\mathcal{H} = \mathcal{H}_{atom} + \mathcal{H}_{light} + \mathcal{H}_{int} \,. \tag{2.20}$$

For our two level atomic system, we assume the energy levels of interest to be $\hbar\omega_{ground}$ and $\hbar\omega_{excited}$. Since only differences in energy are of interest, we can take the ground state energy to be zero, then the energy of the excited state relative to the ground is $\hbar\omega_0 = \hbar(\omega_{excited} - \omega_{ground})$. Thus, in the number basis, defined by the population of the ground and excited states, $\{|g\rangle\,, |e\rangle\}$, we can write $\mathcal{H}_{atom}$ as

$$\mathcal{H}_{atom} = \hbar\omega_0 \hat{a}^\dagger \hat{a}\,, \tag{2.21}$$

where $\hat{a}$ is the excited state annihilation operator, and conversely, $\hat{a}^\dagger$ is the creation operator. In reality, an atom will have many more energy levels than two. However, as long as the frequency of the driving electric field that we consider is close to the spacing between these two levels, then all other energy levels will be far detuned and we will populate only these two levels. In this case, ignoring all other atomic levels is a reasonable approximation.

We next consider the photon energy term, $\mathcal{H}_{light}$. Throughout this thesis, the effect of this term is ignored. This study is focused on the large photon limit, where the electric field can be modeled as a classical field. Including this term would require quantizing the electric field and its coupling to the emitters. However, the goal of this project was to fully explore the regimes of behavior possible in MNP-SQD hybrid structures when in the classical limit for the field. We treat electric fields classically, while treating the atom as a quantum system. This is called a semiclassical approximation, and we make use of it throughout this thesis.

Lastly, we look at the interaction term of the Hamiltonian, $\mathcal{H}_{int}$. In systems that we are most concerned with, the typical size of our atoms, whether true atoms or effective atomic systems (quantum dots, dyes, etc), will be much smaller than the wavelength of light we will be concerned with ($\approx 100 - 1000\,nm$). In such a case, we can make use of the dipole approximation for our interaction term. The classical expression for the energy of a dipole, with dipole moment $\boldsymbol{\mu}$, in an electric field $\mathbf{E}$, is just

$$E_{classical} = -\boldsymbol{\mu} \cdot \mathbf{E} \tag{2.22}$$

In our case, we do not have a permanent dipole but rather a neutral atom that can undergo a dipole transition. Thus to arrive at a quantum mechanical version of (2.22), we replace $\boldsymbol{\mu}$ with the dipole operator $\hat{\boldsymbol{\mu}}$ [48]. In the position basis, the dipole operator is just $\hat{\boldsymbol{\mu}} = q \cdot \hat{\mathbf{r}}$, where $\hat{\mathbf{r}}$ is the usual position operator and q is the charge.

We now need to calculate $\hat{\boldsymbol{\mu}}$ in the number basis. First consider $\langle g| \hat{\boldsymbol{\mu}} |g\rangle$ and $\langle e| \hat{\boldsymbol{\mu}} |e\rangle$. For systems, such as atoms or spherical quantum dots, the energy eigenvectors, written as $|g\rangle$ and $|e\rangle$, are either even or odd functions of their spatial coordinates, and thus have definite parity. However, since $\hat{\boldsymbol{\mu}}$ has odd parity, these diagonal matrix elements must be zero. For the other two matrix elements we set $\boldsymbol{\mu_{ge}} = \langle g| \hat{\boldsymbol{\mu}} |e\rangle$ and note that $\boldsymbol{\mu_{eg}} = \boldsymbol{\mu_{ge}}^*$. Thus we can write the matrix representation of $\hat{\boldsymbol{\mu}}$ in the $\{|g\rangle, |e\rangle\}$ basis as,

$$\hat{\boldsymbol{\mu}} = \begin{pmatrix} 0 & \boldsymbol{\mu_{ge}} \\ \boldsymbol{\mu_{ge}}^* & 0 \end{pmatrix}. \tag{2.23}$$

Since the annihilation operator has the matrix representation $\left(\begin{smallmatrix} 0 & 1 \\ 0 & 0 \end{smallmatrix}\right)$, we can write this as

$$\hat{\boldsymbol{\mu}} = \boldsymbol{\mu_{ge}}\hat{a} + \boldsymbol{\mu_{ge}}^{*}\hat{a}^{\dagger} = \boldsymbol{\mu_{ge}}\hat{a} + h.c., \tag{2.24}$$

and we can now write $\mathcal{H}_{int}$ as

$$\mathcal{H}_{int} = -(\boldsymbol{\mu_{ge}} \cdot \mathbf{E})\ \hat{a} - (\boldsymbol{\mu_{ge}}^{*} \cdot \mathbf{E})\ \hat{a}^{\dagger}. \tag{2.25}$$

Now, we wish to diagonalize our Hamiltonian in the semiclassical approximation, $\mathcal{H} = \mathcal{H}_{atom} + \mathcal{H}_{int}$. We take $\mathbf{E} = E_0 \cos\omega t\ \hat{z}$ as the form of our driving field, where $\hat{z}$ is the unit vector in the z-direction, and set $(\mu_{ge})_z \equiv \mu$ We then calculate $\mathcal{H}_{int}$ as

$$\begin{aligned}
\mathcal{H}_{int} &= -\mu E_0 \cos\omega t\ \hat{a} - \mu^{*} E_0 \cos\omega t\ \hat{a}^{\dagger} \\
&= -\frac{\mu E_0}{2}\left(e^{i\omega t} + e^{-i\omega t}\right)\ \hat{a} + h.c. \\
&\equiv -\hbar\ \Omega\left(e^{i\omega t} + e^{-i\omega t}\right)\ \hat{a} + h.c.,
\end{aligned}$$

where we have defined $\Omega = \frac{\mu E_0}{2\hbar}$, which will be shown to be the usual Rabi frequency.

We now switch over to work in the interaction picture. In the interaction picture, we transform all of our operators such that

$$A_S \rightarrow A_{int}(t) = e^{i\mathcal{H}_{atom}t/\hbar}\ A_S\ e^{-i\mathcal{H}_{atom}t/\hbar}$$

where we have used an S subscript to denote the operator in the Schrödinger picture. Because $\mathcal{H}_{atom}$ commutes with $e^{i\mathcal{H}_{atom}t/\hbar}$, it takes the same form in both pictures,

however $\mathcal{H}_{int}$ is now

$$\begin{aligned}\mathcal{H}_{int} &= -\hbar\ \Omega \left(e^{i\omega t} + e^{-i\omega t}\right)\ e^{i\omega_0 \hat{a}_S^\dagger \hat{a}_S t}\ \hat{a}_S\ e^{-i\omega_0 \hat{a}_S^\dagger \hat{a}_S t} + h.c. \\ &= -\hbar\ \Omega \left(e^{i\omega t} + e^{-i\omega t}\right)\ e^{-i\omega_0 t}\ \hat{a}_S + h.c. \\ &= -\hbar\ \Omega \left(e^{i(\omega-\omega_0)t} + e^{-i(\omega+\omega_0)t}\right)\ \hat{a}_S + h.c.\end{aligned}$$

where we have used the relation $e^{i\omega_0 \hat{a}_S^\dagger \hat{a}_S t}\ \hat{a}_S\ e^{-i\omega_0 \hat{a}_S^\dagger \hat{a}_S t} = e^{-i\omega_0 t}\ \hat{a}_S$. Near resonance, we can assume $(\omega + \omega_0) >> (\omega - \omega_0)$. Therefore, the $e^{\pm i(\omega+\omega_0)t}$ terms, will oscillate much faster than the $e^{\pm i(\omega-\omega_0)t}$ terms. Thus on the time scales that we are interested in, $t \sim \frac{2\pi}{(\omega-\omega_0)}$, the effect of the fast oscillating term averages to zero and can be neglected. This is the rotating wave approximation. Dropping these terms and moving back to the Schrödinger picture, our interaction Hamiltonian is,

$$\mathcal{H}_{int} = -\hbar\ \Omega\ e^{i\omega t}\ \hat{a} - \hbar\ \Omega^*\ e^{-i\omega t}\ \hat{a}^\dagger. \tag{2.26}$$

Now, we solve the master equation,

$$\dot{\rho} = -\frac{i}{\hbar}\Big[\mathcal{H}_{atom} + \mathcal{H}_{int}, \rho\Big]. \tag{2.27}$$

Working in the basis that diagonalizes $\mathcal{H}_{atom}$, we can write down the following differential equations for the components of ρ,

$$\begin{aligned}\dot{\rho}_{gg} &= i\ \Omega\ e^{it\omega}\ \rho_{eg} - i\ \Omega^*\ e^{-it\omega}\ \rho_{ge} \\ \dot{\rho}_{ge} &= i\ \Omega\ e^{it\omega}\ (\ \rho_{ee} - \ \rho_{gg}) + i\omega_0 \rho_{ge} \\ \dot{\rho}_{ee} &= i\ \Omega^*\ e^{-it\omega}\ \rho_{ge} - i\ \Omega\ e^{it\omega}\ \rho_{eg}.\end{aligned}$$

It is important to remember that because $\rho_{eg} = \rho_{ge}^*$, the equation for $\dot{\rho}_{eg}$ is redundant. However, we do have an additional restraint from the normalization of

the density matrix, $\rho_{ee} + \rho_{gg} = 1$. The factors of $e^{-it\omega}$ paired with ρ_{ge}, as well as the $i\omega_0\rho_{ge}$ term in the equation for $\dot{\rho}_{ge}$ suggests a solution of the form $\rho_{ge}(t) = \widetilde{\rho}_{ge}(t)\, e^{i\omega t}$, where we have explicitly factored out the fast oscillating component of ρ_{ge} by moving to a rotating frame. Our equations are now,

$$\begin{aligned}
\dot{\rho}_{gg} &= i\ \Omega\ \widetilde{\rho}^{*}_{ge} - i\ \Omega^{*}\ \widetilde{\rho}_{ge} \\
\dot{\widetilde{\rho}}_{ge} &= i\ \Omega\ \ (\ \rho_{ee} - \ \rho_{gg}) + i\,(\omega_0 - \omega)\,\widetilde{\rho}_{ge} \\
\dot{\rho}_{ee} &= i\ \Omega^{*}\ \widetilde{\rho}_{ge} - i\ \Omega\ \widetilde{\rho}^{*}_{ge}.
\end{aligned}$$

Now, let $\widetilde{\rho}_{ge} = A + iB$ and $\Omega = \Omega_R + i\ \Omega_I$, and also define $\Delta_{ge} = \rho_{gg} - \rho_{ee}$. Then we have,

$$\begin{aligned}
\dot{\Delta}_{ge} &= -4\ \Omega_I\ A + 4\ \Omega_R\ B \\
\dot{A} &= (\omega - \omega_0)\ B + \Omega_I\ \Delta_{ge} \\
\dot{B} &= -(\omega - \omega_0)\ A - \Omega_R\ \Delta_{ge}\,.
\end{aligned} \tag{2.28}$$

The first equation is the result of taking the difference of the first and third equations of the previous set of equations.

We can solve these equations for the steady state solution by taking the left hand side of (2.28) to be zero and solving the resulting homogeneous system of equations. However, this set of equations for the steady state limit, as a system of linear homogeneous equations will have either only the null solution (i.e., $A = B = \Delta_{ge} = 0$), or, the null solution along with infinitely more solutions. Thus this model is rather unphysical. In order to make our model more accurate, we need to discuss spontaneous and stimulated emission, which evidently must be present in any real

physical system.

2.6 Stimulated and Spontaneous Emission

As shown in the previous section, an electric field can cause transitions in an atom system. It also turns out to be true even in the absence of an applied electric field. This is due to the fact that the atom can emit into the vacuum modes of the electric field. This interaction with the vacuum (as well as any noise that is also present) can be modeled by assuming that our atomic system is also interacting with a reservoir.

Consider the situation in which our (atomic) system is in contact with a reservoir which we call the "bath". The bath may simply be the vacuum fluctuations of the electric field, or a particularly noisy mode that can induce transitions in our system. Regardless of the origin of the bath, we first make a few assumptions about the nature of the bath.

(a) The bath is much larger than the system of interest, i.e., the bath is much more influential on our system, than our system is on the bath. Thus we take the statistical properties of the bath to be unaffected by the interaction with the system.

(b) The bath and our system are weakly correlated (or more precisely, the coherence between the bath and system can be neglected). From this assumption, we mean that the density matrix describing the combination of the bath and our system can be factored and we can write $\rho_{total} = \rho_B \otimes \rho_S$.

(c) The bath has no memory. Thus the interaction between our system and the bath is a Markov process, i.e., the future evolution of bath is not dependent on the past configuration of the bath. Since "memory" in the quantum sense is given by correlation functions, this means that the correlation time of the bath is much shorter than the time scales that we are interested in for our system.

We begin our analysis by writing the Hamiltonian for the combined system,

$$\mathcal{H} = \mathcal{H}_B + \mathcal{H}_S + \mathcal{H}_{int} \tag{2.29}$$

where the B subscript denotes the bath, S denotes our system and "*int*" is the interaction between the two. We denote the density matrix for the combined system as ρ_{total}, and now move to the interaction picture and write

$$\begin{aligned} \rho_I(t) &= e^{i(H_S+H_B)/\hbar}\ \rho_{total}\ e^{-i(H_S+H_B)/\hbar} \\ \mathcal{H}_I(t) &= e^{i(H_S+H_B)/\hbar}\ \mathcal{H}_{int}\ e^{-i(H_S+H_B)/\hbar} \end{aligned}$$

where $\mathcal{H}_I(t)$ is the interaction Hamiltonian in the interaction picture. The density matrix and Hamiltonian must satisfy the relation

$$\dot{\rho}_I(t) = -\frac{i}{\hbar}[\mathcal{H}_I(t), \rho_I(t)]\,. \tag{2.30}$$

Integrating equation (2.30) from 0 to t, we have

$$\rho_I(t) = \rho_I(0) - \frac{i}{\hbar}\int_0^t dt'[\mathcal{H}_I(t'), \rho_I(t')]\,. \tag{2.31}$$

We now iterate this equation for $\rho_I(t)$ by taking $t \to t'$ and $t' \to t''$ and substituting

for $\rho_I(t')$ on the RHS of (2.31) which gives us,

$$\begin{aligned}\rho_I(t) =&\rho_I(0) - \frac{i}{\hbar}\int_0^t dt'[\mathcal{H}_I(t'), \rho_I(0)] \\ &- \frac{1}{\hbar^2}\int_0^t dt' \int_0^{t'} dt''[\mathcal{H}_I(t'), [\mathcal{H}_I(t''), \rho_I(t'')]]\,.\end{aligned}$$

Finally, differentiating with respect to t, we arrive at

$$\dot{\rho}_I(t) = -\frac{i}{\hbar}[\mathcal{H}_I(t), \rho_I(0)] - \frac{1}{\hbar^2}\int_0^t d\tau[\mathcal{H}_I(t), [\mathcal{H}_I(\tau), \rho_I(\tau)]]\,, \tag{2.32}$$

where the integration variable t'' has been renamed as τ.

We pause here for a moment to recall that ρ_{tot} and $\rho_I(t)$ are operators on the combined space of the bath and system variables. This is not a very useful quantity. The quantity we are actually interested in finding is the reduced density matrix which is obtained by taking ρ_{tot} and tracing over the bath variables,

$$\widetilde{\rho}_{total} \equiv \mathrm{Tr}_B[\rho_{total}]\,. \tag{2.33}$$

We similarly define the reduced interaction picture density matrix

$$\widetilde{\rho}_I(t) \equiv \mathrm{Tr}_B[\rho_I(t)]\,. \tag{2.34}$$

Now, performing a trace over the bath variables on both sides of (2.32), we have,

$$\dot{\widetilde{\rho}}_I(t) = -\frac{i}{\hbar}\mathrm{Tr}_B\Big[[\mathcal{H}_I(t), \rho_I(0)]\Big] - \frac{1}{\hbar^2}\int_0^t d\tau\ \mathrm{Tr}_B\Big[[\mathcal{H}_I(t), [\mathcal{H}_I(\tau), \rho_I(\tau)]]\Big]\,. \tag{2.35}$$

First, we assume that initially, the bath and system are uncorrelated. Thus, $\rho_I(0) = \rho_{total}(0) = \rho_B \otimes \rho_S(0)$. Next, consider the first term. We can assume that this term is zero if $\mathcal{H}_{int}$ has no diagonal elements over the bath variables (i.e., H_{int} always

changes the bath quantum numbers). Although there is no reason to expect that $\mathcal{H}_{int}$ will not contain any terms with factors of $b^\dagger b$, for example, we assume that we can do so with a suitable redefinition of $\mathcal{H}_{sys}$ and $\mathcal{H}_{int}$. By now invoking our assumption that the bath is relatively unchanged by the interaction with the system, we can approximate the interaction picture density matrix as the tensor product of the bath density matrix and the reduced interaction picture density matrix,

$$\rho_I(t) \approx \rho_B \otimes \widetilde{\rho}_I(t)\,. \tag{2.36}$$

These approximations now allow us to write (2.35) as

$$\dot{\widetilde{\rho}}_I(t) = -\frac{1}{\hbar^2}\int_0^t d\tau\ \mathrm{Tr}_B\Big[[\mathcal{H}_I(t),[\mathcal{H}_I(t-\tau),\rho_B\otimes\widetilde{\rho}_I(t-\tau)]]\Big]\,. \tag{2.37}$$

where we have also made the change in integration variable $\tau \to t-\tau$.

Lastly, we invoke the Markov approximation which allows us to assume that over the time scale of the bath correlation time, $\widetilde{\rho}_I(t)$ is relatively unchanged compared to the bath variables. This allows us to take $\widetilde{\rho}_I(t-\tau) \approx \widetilde{\rho}_I(t)$. Furthermore, if we assume that t is much larger than the bath correlation time, then we can time the limit of our integral to infinity and we can write (2.37) now in its usual form [49],

$$\dot{\widetilde{\rho}}_I(t) = -\frac{1}{\hbar^2}\int_0^\infty d\tau\ \mathrm{Tr}_B\Big[[\mathcal{H}_I(t),[\mathcal{H}_I(t-\tau),\rho_B\otimes\widetilde{\rho}_I(t)]]\Big]\,, \tag{2.38}$$

which is a first order differential equation in time, showing the Markovian property of the combined system.

2.7 Toy Model: Two Level System Interacting with a Single Bosonic Mode

We now use the formalism we just developed to model the spontaneous emission from an atomic system. We again consider a two level atom, but now we allow the atom to interact with a bath consisting of a single bosonic mode. We begin with the following Hamiltonians,

$$\mathcal{H}_S = \hbar\omega_s \hat{s}^\dagger \hat{s}$$

$$\mathcal{H}_B = \hbar\omega_b \hat{b}^\dagger \hat{b}$$

$$\mathcal{H}_{int} = \mu \left(\hat{s}^\dagger \hat{b} + \hat{b}^\dagger \hat{s} \right)$$

where $\hat{s}^\dagger$ and $\hat{s}$ are the (fermionic) raising and lowering operators for the atomic system, and $\hat{b}^\dagger$ and $\hat{b}$ are the (bosonic) raising and lowering operators for the bath. Then

$$\begin{aligned}
\dot{\tilde{\rho}}_I(t) &= -\frac{1}{\hbar^2}\int_0^\infty d\tau \ \mathrm{Tr}_B\Big[[\mathcal{H}_I(t),[\mathcal{H}_I(t-\tau),\rho_B\otimes\tilde{\rho}_I(t)]]\Big] \\
&= -\frac{1}{\hbar^2}\int_0^\infty d\tau \sum_B \Big(\ \langle B| \ \mathcal{H}_I(t)\ \mathcal{H}_I(t-\tau)\ \rho_B\otimes\tilde{\rho}_I(t) \ |B\rangle \\
&\qquad\qquad - \langle B| \ \mathcal{H}_I(t)\ \rho_B\otimes\tilde{\rho}_I(t)\ \mathcal{H}_I(t-\tau) \ |B\rangle \\
&\qquad\qquad - \langle B| \ \mathcal{H}_I(t-\tau)\ \rho_B\otimes\tilde{\rho}_I(t)\ \mathcal{H}_I(t) \ |B\rangle \\
&\qquad\qquad + \langle B| \ \rho_B\otimes\tilde{\rho}_I(t)\ \mathcal{H}_I(t-\tau)\ \mathcal{H}_I(t) \ |B\rangle \Big) \\
&\equiv -\frac{1}{\hbar^2}\int_0^\infty d\tau \, (\ \mathcal{T}_1 + \mathcal{T}_2 + \mathcal{T}_3 + \mathcal{T}_4 \ ) \, .
\end{aligned} \tag{2.39}$$

We now evaluate each term in turn.

$$
\begin{aligned}
\mathcal{T}_1 =& \sum_B \ \langle B| \ \mathcal{H}_I(t) \ \mathcal{H}_I(t-\tau) \ \rho_B \otimes \widetilde{\rho}_I(t) \ \ |B\rangle \\
=& \mu \sum_B \ e^{i(\mathcal{H}_S + E_B)t/\hbar} \Big(\ \hat{s}^\dagger \ \sqrt{B+1} \ \langle B+1| + \ \hat{s} \ \sqrt{B} \ \langle B-1| \ \Big) \times \\
& \qquad \times e^{-i(\mathcal{H}_S+\mathcal{H}_B)\tau/\hbar} \ \mathcal{H}_{int} \ e^{-i(\mathcal{H}_S+\mathcal{H}_B)(t-\tau)/\hbar} \ \rho_B \otimes \widetilde{\rho}_I(t) \ \ |B\rangle \\
=& \mu \sum_B \ e^{iB\omega_b t} \Big(e^{-i\omega_b(B+1)\tau} \ e^{i\omega_s t} \ \hat{s}^\dagger \ e^{-i\mathcal{H}_S\tau/\hbar} \ \sqrt{B+1} \ \langle B+1| \\
& \qquad + e^{-i\omega_b(B-1)\tau} \ \hat{s} \ e^{-i\mathcal{H}_S\tau/\hbar} \ \sqrt{B} \ \langle B-1| \Big) \times \\
& \qquad \times \ \mathcal{H}_{int} \ e^{-i(\mathcal{H}_S+\mathcal{H}_B)(t-\tau)/\hbar} \ \rho_B \otimes \widetilde{\rho}_I(t) \ \ |B\rangle \\
\mathcal{T}_1 =& \mu^2 \sum_B \ e^{iB\omega_b(t-\tau)} \Big(e^{-i\omega_b\tau} \ e^{i\omega_s t} \ \hat{s}^\dagger \ \sqrt{B+1} \ \langle B+1| \\
& \qquad + e^{i\omega_b\tau} \ e^{-i\omega_s\tau} \ \hat{s} \ \sqrt{B} \ \langle B-1| \Big) \times \\
& \qquad \times \Big(\hat{s}^\dagger \hat{b} + \hat{b}^\dagger \hat{s} \Big) \ e^{-i(\mathcal{H}_S+\mathcal{H}_B)(t-\tau)/\hbar} \ \rho_B \otimes \widetilde{\rho}_I(t) \ \ |B\rangle \\
=& \mu^2 \sum_B \ e^{iB\omega_b(t-\tau)} \Big(e^{-i\omega_b\tau} \ e^{i\omega_s t} \ \hat{s}^\dagger \ \hat{s} \ (B+1) + e^{i\omega_b\tau} \ e^{-i\omega_s\tau} \ \hat{s} \ \hat{s}^\dagger \ B \Big) \times \\
& \qquad \times \ \ \langle B| \ e^{-i(\mathcal{H}_S+\mathcal{H}_B)(t-\tau)/\hbar} \ \rho_B \otimes \widetilde{\rho}_I(t) \ \ |B\rangle \\
=& \mu^2 \sum_B \Big(e^{-i\omega_b\tau} \ e^{i\omega_s\tau} \ \hat{s}^\dagger \ \hat{s} \ (B+1) + e^{i\omega_b\tau} \ e^{-i\omega_s\tau} \ \hat{s} \ \hat{s}^\dagger \ B \Big) \times \\
& \qquad \times \langle B| \, \rho_B \, |B\rangle \otimes \widetilde{\rho}_I(t) \\
=& \mu^2 \Big(e^{-i\omega_b\tau} \ e^{i\omega_s\tau} \ \ \big(\ \bar{B}+1 \big) \ \ \hat{s}^\dagger \ \hat{s} \ \widetilde{\rho}_I(t) + e^{i\omega_b\tau} \ e^{-i\omega_s\tau} \ \ \bar{B} \ \hat{s} \ \hat{s}^\dagger \ \widetilde{\rho}_I(t) \Big)
\end{aligned}
$$

where we have repeatedly used identities like $\hat{s} \ e^{\alpha \, \hat{s}^\dagger \hat{s}} = e^{\alpha} \hat{s}$ and $e^{\alpha \, \hat{s}^\dagger \hat{s}} \ \hat{s} = \hat{s}$, and we have used $\bar{B}$ to denote the average population of the bosonic mode, $\bar{B} = \sum_B \langle B| \, \rho_B \, |B\rangle$.

Now turning our attention to $\mathcal{T}_2$,

$$
\begin{aligned}
\mathcal{T}_2 =& -\sum_B \langle B|\ \mathcal{H}_I(t)\ \rho_B \otimes \widetilde{\rho}_I(t)\ \mathcal{H}_I(t-\tau)\ \ |B\rangle \\
=& -\mu^2 \sum_B\ e^{iB\omega_b t}\Big(e^{i\omega_s t}\ e^{-i(B+1)\omega_b t}\ \hat{s}^\dagger\ \sqrt{B+1}\ \ \langle B+1| \\
&\qquad\qquad +\ \ e^{-i\omega_s t}\ e^{-i(B-1)\omega_b t}\ \hat{s}\ \sqrt{B}\ \ \langle B-1|\ \Big)\times \\
&\qquad \times \rho_B \otimes \widetilde{\rho}_I(t)\Big(e^{i\omega_s(t-\tau)}\ e^{i(B-1)\omega_b(t-\tau)}\ \hat{s}^\dagger\sqrt{B}\,|B-1\rangle \\
&\qquad\qquad +\ \ e^{-i\omega_s(t-\tau)}\ e^{i(B+1)\omega_b(t-\tau)}\ \hat{s}\sqrt{B+1}\,|B+1\rangle\ \Big)\ e^{-iB\omega_b(t-\tau)} \\
=& -\mu^2\Big(e^{i\omega_s\tau}\ e^{-i\omega_b\tau}\ \bar{B}\ \hat{s}^\dagger\ \widetilde{\rho}_I(t)\ \hat{s} +\ \ e^{-i\omega_s\tau}\ e^{i\omega_b\tau}(\bar{B}+1)\ \hat{s}\ \widetilde{\rho}_I(t)\ \hat{s}^\dagger\ \Big)
\end{aligned}
$$

where we have we have used that $\sum_B B\,\langle B-1|\,\rho_B\,|B-1\rangle = \bar{B}+1$. Also, we have assumed that terms like $\sum_B \langle B+1|\,\rho_B\,|B-1\rangle$ can be taken to be zero, which is a safe assumption if our bath is in a thermal state (i.e. has no correlation). However, this would not hold if our bath was in a squeezed state. The calculation for $\mathcal{T}_3$ is similar,

$$
\begin{aligned}
\mathcal{T}_3 =& -\sum_B \langle B|\ \mathcal{H}_I(t-\tau)\ \rho_B \otimes \widetilde{\rho}_I(t)\ \mathcal{H}_I(t)\ \ |B\rangle \\
=& -\mu^2 \sum_B\ e^{iB\omega_b(t-\tau)}\Big(e^{i\omega_s(t-\tau)}\ e^{-i(B+1)\omega_b(t-\tau)}\ \hat{s}^\dagger\ \sqrt{B+1}\ \ \langle B+1| \\
&\qquad\qquad +\ \ e^{-i\omega_s(t-\tau)}\ e^{-i(B-1)\omega_b(t-\tau)}\ \hat{s}\ \sqrt{B}\ \ \langle B-1|\ \Big)\times \\
&\qquad \times \rho_B \otimes \widetilde{\rho}_I(t)\Big(e^{i\omega_s t}\ e^{i(B-1)\omega_b t}\ \hat{s}^\dagger\sqrt{B}\,|B-1\rangle \\
&\qquad\qquad +\ \ e^{-i\omega_s t}\ e^{i(B+1)\omega_b t}\ \hat{s}\sqrt{B+1}\,|B+1\rangle\ \Big)\ e^{-iB\omega_b t} \\
=& -\mu^2\Big(\ e^{-i\omega_s\tau}\ e^{i\omega_b\tau}\ \bar{B}\ \hat{s}^\dagger\ \widetilde{\rho}_I(t)\ \hat{s} +\ \ e^{i\omega_s\tau}\ e^{-i\omega_b\tau}(\bar{B}+1)\ \hat{s}\ \widetilde{\rho}_I(t)\ \hat{s}^\dagger\ \Big).
\end{aligned}
$$

Lastly, a calculation for $\mathcal{T}_4$ yields,

$$\begin{aligned}\mathcal{T}_4 =& \sum_B \ \langle B| \ \rho_B \otimes \widetilde{\rho}_I(t) \ \mathcal{H}_I(t-\tau) \ \mathcal{H}_I(t) \ |B\rangle \\ =& \mu^2 \Big(e^{i\omega_s \tau} \ e^{-i\omega_b \tau} \ \bar{B} \ \widetilde{\rho}_I(t) \ \hat{s} \ \hat{s}^\dagger + \ e^{-i\omega_s \tau} \ e^{i\omega_b \tau} (\ \bar{B} + 1) \ \widetilde{\rho}_I(t) \ \hat{s}^\dagger \ \hat{s} \ \Big).\end{aligned}$$

Returning to (2.39) and putting this together,

$$\begin{aligned}\dot{\widetilde{\rho}}_I(t) =& -\frac{1}{\hbar^2} \int_0^\infty d\tau \ (\ \mathcal{T}_1 + \mathcal{T}_2 + \mathcal{T}_3 + \mathcal{T}_4 \ ) \\ =& -\frac{\mu^2}{\hbar^2} \int_0^\infty d\tau \Big(e^{i\omega_b \tau} \ e^{-i\omega_s \tau} \ \bar{B} \ \hat{s} \ \hat{s}^\dagger \ \widetilde{\rho}_I(t) + e^{-i\omega_b \tau} \ e^{i\omega_s \tau} \ \Big(\ \bar{B} + 1 \Big) \ \hat{s}^\dagger \ \hat{s} \ \widetilde{\rho}_I(t) \\ & - e^{i\omega_s \tau} \ e^{-i\omega_b \tau} \ \bar{B} \ \hat{s}^\dagger \ \widetilde{\rho}_I(t) \ \hat{s} - \ e^{-i\omega_s \tau} \ e^{i\omega_b \tau} (\bar{B} + 1) \ \hat{s} \ \widetilde{\rho}_I(t) \ \hat{s}^\dagger \\ & - e^{-i\omega_s \tau} \ e^{i\omega_b \tau} \ \bar{B} \ \hat{s}^\dagger \ \widetilde{\rho}_I(t) \ \hat{s} - \ e^{i\omega_s \tau} \ e^{-i\omega_b \tau} (\bar{B} + 1) \ \hat{s} \ \widetilde{\rho}_I(t) \ \hat{s}^\dagger \\ & + e^{i\omega_s \tau} \ e^{-i\omega_b \tau} \ \bar{B} \ \widetilde{\rho}_I(t) \ \hat{s} \ \hat{s}^\dagger + \ e^{-i\omega_s \tau} \ e^{i\omega_b \tau} (\ \bar{B} + 1) \ \widetilde{\rho}_I(t) \ \hat{s}^\dagger \ \hat{s} \ \Big) \\ =& -\frac{\mu^2}{\hbar^2} \int_0^\infty d\tau \Big(e^{i(\omega_b - \omega_s)\tau} \ \bar{B} \big(\ \hat{s} \ \hat{s}^\dagger \ \widetilde{\rho}_I(t) - \ \hat{s}^\dagger \ \widetilde{\rho}_I(t) \ \hat{s} \big) \\ & + \ e^{-i(\omega_b - \omega_s)\tau} \ \bar{B} \big(\ \widetilde{\rho}_I(t) \ \hat{s} \ \hat{s}^\dagger \ - \hat{s}^\dagger \ \widetilde{\rho}_I(t) \ \hat{s} \big) \\ & + e^{i(\omega_b - \omega_s)\tau} \ (\bar{B} + 1) \big(\ \widetilde{\rho}_I(t) \ \hat{s}^\dagger \ \hat{s} - \ \hat{s} \ \widetilde{\rho}_I(t) \ \hat{s}^\dagger \big) \\ & + e^{-i(\omega_b - \omega_s)\tau} \ (\bar{B} + 1) \big(\ \hat{s}^\dagger \ \hat{s} \ \widetilde{\rho}_I(t) - \ \hat{s} \ \widetilde{\rho}_I(t) \ \hat{s}^\dagger \big) \\ =& -\gamma \ \bar{B} \Big(\ \hat{s} \ \hat{s}^\dagger \ \widetilde{\rho}_I(t) + \ \widetilde{\rho}_I(t) \ \hat{s} \ \hat{s}^\dagger - 2 \ \hat{s}^\dagger \ \widetilde{\rho}_I(t) \ \hat{s} \big) \\ & - \gamma \ (\bar{B} + 1) \Big(\ \hat{s}^\dagger \ \hat{s} \ \widetilde{\rho}_I(t) + \ \widetilde{\rho}_I(t) \ \hat{s}^\dagger \ \hat{s} - 2 \ \hat{s} \ \widetilde{\rho}_I(t) \ \hat{s}^\dagger \big) \\ & - i \ \epsilon \ \bar{B} \ [\ \hat{s} \ \hat{s}^\dagger, \ \widetilde{\rho}_I(t)] - i \ \epsilon \ (\bar{B} + 1) \ [\ \hat{s}^\dagger \ \hat{s}, \ \widetilde{\rho}_I(t)]\end{aligned}$$

where we have defined $\frac{\mu^2}{\hbar^2} \int_0^\infty d\tau e^{i(\omega_b - \omega_s)\tau} = \gamma + i\epsilon$. The terms proportional to $\epsilon \ \bar{B}$ and $\epsilon \ (\bar{B}+1)$ are the Stark and Lamb shifts respectively. They represent small shifts in the energy levels of the system and can often be neglected. The term proportional

to γ ($\bar{B}$) goes to zero as the average excitation population of the bath goes to zero, and thus would not be present at zero temperature. However, the $\gamma(\bar{B}+1)$ term is present even at zero temperature and represents transitions in our system from a state with a higher energy to a lower energy state, while the previous must represent a transition from a lower energy state to one that is higher.

2.8 Lindblad Master Equation

In this thesis, we will model interactions at optical frequencies. We can further develop our framework of modeling open systems in such a case. To do so, we return to the case of an atomic system in an arbitrary bath, at optical frequencies. We assume only that our interaction Hamiltonian can be written as

$$\mathcal{H}_{int} = \hbar \sum_j \left(\hat{s}_j^\dagger \ \hat{b}_j + \hat{s}_j \ \hat{b}_j^\dagger \right) \tag{2.40}$$

where the $\hat{b}_j$ are some set of bath operators, and the $\hat{s}_j$ are operators on the system Hilbert space and satisfy

$$[\mathcal{H}_{sys}, \ \hat{s}_j] = -\hbar\omega_j \ \hat{s}_j \, . \tag{2.41}$$

For example, interaction terms with $\hat{s} = \hat{a}$, where $\hat{a}$ is an annihilation operator would represent an excitation transfer with the bath. Additionally, terms where $\hat{s} = \hat{a}^\dagger\hat{a}$ (noting that $[\mathcal{H}_{sys}, \ \hat{a}^\dagger\hat{a}] = 0$ trivially satisfies (2.41)) would be indicative of bath induced scattering processes and would give rise to dephasing in our system.

From (2.41) we can work out the following identity that will be very useful in

the derivation that follows. Consider the quantity, $e^{\alpha \mathcal{H}_{sys}}\ \hat{s}_j$,

$$\begin{aligned} e^{\alpha \mathcal{H}_{sys}}\ \hat{s}_j &= \left(1 +\ \alpha\ \mathcal{H}_{sys} + \frac{1}{2!}\ (\alpha\ \mathcal{H}_{sys})^2 + \dots \right)\ \hat{s}_j \\ &= \left(\ \hat{s}_j +\ \hat{s}_j\ \alpha(\ \mathcal{H}_{sys} - \hbar\omega_j) +\ \hat{s}_j\ \frac{1}{2!}(\ \alpha(\ \mathcal{H}_{sys} - \hbar\omega_j))^2 + \dots \right) \\ &=\ \hat{s}_j\ e^{\alpha(\mathcal{H}_{sys} - \hbar\omega_j)}\,. \end{aligned}$$

Thus, in the interaction picture,

$$\begin{aligned} \hat{s}_j(t) &= e^{i\mathcal{H}_{sys}t/\hbar}\ \hat{s}_j\ e^{-i\mathcal{H}_{sys}t/\hbar} \\ &= e^{-i\omega_j t}\ \hat{s}_j \end{aligned} \tag{2.42}$$

and similarly,

$$\begin{aligned} \hat{s}_j^\dagger(t) &= e^{i\mathcal{H}_{sys}t/\hbar}\ \hat{s}_j\ e^{-i\mathcal{H}_{sys}t/\hbar} \\ &= e^{i\omega_j t}\ \hat{s}_j^\dagger\,. \end{aligned} \tag{2.43}$$

Now, we return our attention to (2.40) and substitute this interaction Hamiltonian into (2.38), our master equation for the reduced density matrix. We again have many terms to evaluate and define $\mathcal{T}_1, \mathcal{T}_2, \mathcal{T}_3$, and $\mathcal{T}_4$ as before. Thus,

$$\begin{aligned} \mathcal{T}_1 =& \frac{1}{\hbar^2}\ \mathrm{Tr}_B[\ \mathcal{H}_I(t)\ \mathcal{H}_I(t-\tau)\ \rho_B \otimes \widetilde{\rho}_I(t)] \\ =& \sum_j \sum_k\ \mathrm{Tr}_B\Bigg[\left(e^{i\omega_j t}\ \hat{s}_j^\dagger\ \hat{b}_j(t) + e^{-i\omega_j t}\ \hat{s}_j\ \hat{b}_j^\dagger(t)\right) \\ & \qquad \times \left(e^{i\omega_k(t-\tau)}\ \hat{s}_k^\dagger\ \hat{b}_k(t-\tau) + e^{-i\omega_k(t-\tau)}\ \hat{s}_k\ \hat{b}_k^\dagger(t-\tau)\right)\ \rho_B \otimes \widetilde{\rho}_I(t)\Bigg] \\ =& \sum_j \sum_k\ \mathrm{Tr}_B\Bigg[\Big(e^{i\omega_j\tau}\ e^{i(\omega_j-\omega_k)t}\ \hat{s}_j^\dagger\ \hat{s}_k\ \hat{b}_j(t)\ \hat{b}_k^\dagger(t-\tau) \\ & \qquad + e^{-i\omega_j\tau}\ e^{-i(\omega_j-\omega_k)t}\ \hat{s}_j\ \hat{s}_k^\dagger\ \hat{b}_j^\dagger(t)\ \hat{b}_k(t-\tau)\ \Big)\ \rho_B \otimes \widetilde{\rho}_I(t)\Bigg]\,, \end{aligned}$$

where we have again dropped terms like $\mathrm{Tr}_B[\ \hat{b}_j(t)\ \hat{b}_k(t-\tau)\ \rho_B]$, assuming that our bath is in a thermal state. We now make the rotating wave approximation by neglecting terms with $j \neq k$. We can do so because if $\omega_j \neq \omega_k$, then $e^{\pm i(\omega_j - \omega_k)t}$ is a quickly varying function over the time scale of the correlation time, and thus will make only a minor contribution compared to the term with $j = k$. However, if j and k are degenerate energy eigenstates, then this would not hold and care would need to be taken. Returning to $\mathcal{T}_1$, we have

$$\begin{aligned}\mathcal{T}_1 = \sum_j \Big(& e^{i\omega_j \tau}\ \mathrm{Tr}_B\ \big[\ \hat{b}_j(t)\ \hat{b}_j^\dagger(t-\tau)\ \rho_B\big]\ \hat{s}_j^\dagger\ \hat{s}_j\ \widetilde{\rho}_I(t) \\ & + e^{-i\omega_j \tau}\ \mathrm{Tr}_B\ \big[\ \hat{b}_j^\dagger(t)\ \hat{b}_j(t-\tau)\ \rho_B\big]\ \hat{s}_j\ \hat{s}_j^\dagger\ \widetilde{\rho}_I(t)\Big)\end{aligned}$$

Proceeding to $\mathcal{T}_2$, we find,

$$\begin{aligned}\mathcal{T}_2 &= -\sum_j \Big(e^{i\omega_j \tau}\ \mathrm{Tr}_B\ \big[\ \hat{b}_j(t)\ \rho_B\ \hat{b}_j^\dagger(t-\tau)\big]\ \hat{s}_j^\dagger\ \widetilde{\rho}_I(t)\ \hat{s}_j \\ &\qquad + e^{-i\omega_j \tau}\ \mathrm{Tr}_B\ \big[\ \hat{b}_j^\dagger(t)\ \rho_B\ \hat{b}_j(t-\tau)\big]\ \hat{s}_j\ \widetilde{\rho}_I(t)\ \hat{s}_j^\dagger\Big) \\ &= -\sum_j \Big(e^{i\omega_j \tau}\ \mathrm{Tr}_B\ \big[\ \hat{b}_j^\dagger(t-\tau)\ \hat{b}_j(t)\ \rho_B\big]\ \hat{s}_j^\dagger\ \widetilde{\rho}_I(t)\ \hat{s}_j \\ &\qquad + e^{-i\omega_j \tau}\ \mathrm{Tr}_B\ \big[\ \hat{b}_j(t-\tau)\ \hat{b}_j^\dagger(t)\ \rho_B\big]\ \hat{s}_j\ \widetilde{\rho}_I(t)\ \hat{s}_j^\dagger\Big),\end{aligned}$$

where we have used the cyclic property of the trace. Similarly for $\mathcal{T}_3$ and $\mathcal{T}_4$ we

have,

$$\mathcal{T}_3 = -\sum_j \Big(e^{-i\omega_j\tau}\ \mathrm{Tr}_B\left[\ \hat{b}_j^\dagger(t)\ \hat{b}_j(t-\tau)\ \rho_B\right]\ \hat{s}_j^\dagger\ \widetilde{\rho}_I(t)\ \hat{s}_j + e^{i\omega_j\tau}\ \mathrm{Tr}_B\left[\ \hat{b}_j(t)\ \hat{b}_j^\dagger(t-\tau)\ \rho_B\right]\ \hat{s}_j\ \widetilde{\rho}_I(t)\ \hat{s}_j^\dagger \Big)$$

$$\mathcal{T}_4 = \sum_j \Big(e^{-i\omega_j\tau}\ \mathrm{Tr}_B\left[\ \hat{b}_j(t-\tau)\ \hat{b}_j^\dagger(t)\ \rho_B\right]\ \widetilde{\rho}_I(t)\ \hat{s}_j^\dagger\ \hat{s}_j + e^{i\omega_j\tau}\ \mathrm{Tr}_B\left[\ \hat{b}_j^\dagger(t-\tau)\ \hat{b}_j(t)\ \rho_B\right]\ \widetilde{\rho}_I(t)\ \hat{s}_j\ \hat{s}_j^\dagger \Big).$$

We now make the Markov approximation and assume that factors like

$$\mathrm{Tr}_B\left[\ \hat{b}_j(t-\tau)\ \hat{b}_j^\dagger(t)\ \rho_B\right]$$

are functions of τ only as the bath has very short memory. This allows us to write this factor as $\mathrm{Tr}_B\left[\ \hat{b}_j(0)\ \hat{b}_j^\dagger(\tau)\ \rho_B\right]$. Upon transforming all of the terms we've accumulated, our correlation factors all take one of four possible forms,

$$e^{-i\omega_j\tau}\ \mathrm{Tr}_B\left[\ \hat{b}_j^\dagger(\tau)\ \hat{b}_j(0)\ \rho_B\right]$$

$$e^{i\omega_j\tau}\ \mathrm{Tr}_B\left[\ \hat{b}_j^\dagger(0)\ \hat{b}_j(\tau)\ \rho_B\right]$$

$$e^{-i\omega_j\tau}\ \mathrm{Tr}_B\left[\ \hat{b}_j(0)\ \hat{b}_j^\dagger(\tau)\ \rho_B\right]$$

$$e^{i\omega_j\tau}\ \mathrm{Tr}_B\left[\ \hat{b}_j(\tau)\ \hat{b}_j^\dagger(0)\ \rho_B\right].$$

Noting that the first two of these terms are complex conjugates of each other, and that the same can be said for the third and fourth terms, we make the following

definitions,

$$\int_0^t d\tau\ e^{i\omega_j\tau}\ \mathrm{Tr}_B\ \big[\ \hat{b}_j^\dagger(0)\ \hat{b}_j(\tau)\ \rho_B\big] \equiv \Gamma_j + i\epsilon_j$$
$$\int_0^t d\tau\ e^{-i\omega_j\tau}\ \mathrm{Tr}_B\ \big[\ \hat{b}_j^\dagger(\tau)\ \hat{b}_j(0)\ \rho_B\big] \equiv \Gamma_j - i\epsilon_j$$
$$\int_0^t d\tau\ e^{i\omega_j\tau}\ \mathrm{Tr}_B\ \big[\ \hat{b}_j(\tau)\ \hat{b}_j^\dagger(0)\ \rho_B\big] \equiv \gamma_j + i\delta_j$$
$$\int_0^t d\tau\ e^{-i\omega_j\tau}\ \mathrm{Tr}_B\ \big[\ \hat{b}_j(0)\ \hat{b}_j^\dagger(\tau)\ \rho_B\big] \equiv \gamma_j - i\delta_j\,.$$

If the $\hat{b}_j$ are creation operators, then at zero temperature both γ and δ are non zero due to the ordering of $\hat{b}_j(\tau)$ and $\hat{b}_j^\dagger(\tau)$, and are thus the result of vacuum fluctuations.

Now returning to our master equation,

$$\begin{aligned}
\dot{\widetilde{\rho}}_I(t) &= -\frac{1}{\hbar^2}\int_0^t d\tau\ (\ \mathcal{T}_1 + \mathcal{T}_2 + \mathcal{T}_3 + \mathcal{T}_4\ ) \\
&= -\sum_j \Big(\ (\gamma_j + i\delta_j)\ \hat{s}_j^\dagger\ \hat{s}_j\ \widetilde{\rho}_I(t) + (\Gamma_j - i\epsilon_j)\ \hat{s}_j\ \hat{s}_j^\dagger\ \widetilde{\rho}_I(t) \\
&\qquad - (\Gamma_j + i\epsilon_j)\ \hat{s}_j^\dagger\ \widetilde{\rho}_I(t)\ \hat{s}_j - (\gamma_j - i\delta_j)\ \hat{s}_j\ \widetilde{\rho}_I(t)\ \hat{s}_j^\dagger \\
&\qquad - (\Gamma_j - i\epsilon_j)\ \hat{s}_j^\dagger\ \widetilde{\rho}_I(t)\ \hat{s}_j - (\gamma_j + i\delta_j)\ \hat{s}_j\ \widetilde{\rho}_I(t)\ \hat{s}_j^\dagger \\
&\qquad + (\gamma_j - i\delta_j)\ \widetilde{\rho}_I(t)\ \hat{s}_j^\dagger\ \hat{s}_j + (\Gamma_j + i\epsilon_j)\ \widetilde{\rho}_I(t)\ \hat{s}_j\ \hat{s}_j^\dagger\ \Big) \\
&= -\sum_j \Big\{\ \gamma_j\ \big(\ \hat{s}_j^\dagger\ \hat{s}_j\ \widetilde{\rho}_I(t) + \ \widetilde{\rho}_I(t)\ \hat{s}_j^\dagger\ \hat{s}_j - 2\hat{s}_j\ \widetilde{\rho}_I(t)\ \hat{s}_j^\dagger\big) \\
&\qquad + \Gamma_j\big(\ \hat{s}_j\ \hat{s}_j^\dagger\ \widetilde{\rho}_I(t) + \widetilde{\rho}_I(t)\ \hat{s}_j\ \hat{s}_j^\dagger - 2\hat{s}_j^\dagger\ \widetilde{\rho}_I(t)\ \hat{s}_j\big) \\
&\qquad + i\delta_j\ \big(\ \hat{s}_j^\dagger\ \hat{s}_j\ \widetilde{\rho}_I(t) - \ \widetilde{\rho}_I(t)\ \hat{s}_j^\dagger\ \hat{s}_j\big) \\
&\qquad + i\epsilon_j\ \big(\ \widetilde{\rho}_I(t)\ \hat{s}_j\ \hat{s}_j^\dagger - \ \hat{s}_j\ \hat{s}_j^\dagger\ \widetilde{\rho}_I(t)\ \big)\ \Big\}\,.
\end{aligned}$$

We again identify ϵ_j and δ_j as the Lamb and Stark shifts, and note that they play little role in the analysis that follows and will be neglected from here on out.

Thus, for each term in our interaction Hamiltonian, $\hat{s}_j^\dagger\ \hat{b}_j$ or $\hat{s}_j\ \hat{b}_j^\dagger$, we have a term in our master equation, like

$$\hat{s}_j^\dagger\ \hat{s}_j\ \widetilde{\rho}_I(t) + \ \widetilde{\rho}_I(t)\ \hat{s}_j^\dagger\ \hat{s}_j - 2\hat{s}_j\ \widetilde{\rho}_I(t)\ \hat{s}_j^\dagger\,,$$

or

$$\hat{s}_j\ \hat{s}_j^\dagger\ \widetilde{\rho}_I(t) + \widetilde{\rho}_I(t)\ \hat{s}_j\ \hat{s}_j^\dagger - 2\hat{s}_j^\dagger\ \widetilde{\rho}_I(t)\ \hat{s}_j$$

which are both of similar form. With this as motivation, we define the Lindblad operator [50, 51] such that its action on an arbitrary operator $\hat{s}$ and density matrix ρ is,

$$\mathcal{L}(\hat{s})\ \rho = \ \hat{s}^\dagger\ \hat{s}\ \rho + \ \rho\ \hat{s}^\dagger\ \hat{s} - 2\hat{s}\ \rho\ \hat{s}^\dagger\,. \tag{2.44}$$

Using this definition allows us to write down the master equation in the following form,

$$\dot{\widetilde{\rho}}_I(t) = -\sum_j\ \lambda_j\ \mathcal{L}(\hat{s}_j)\ \widetilde{\rho}_I(t) \tag{2.45}$$

with our interaction Hamiltonian now written as

$$\mathcal{H}_{int} = \hbar \sum_j \hat{s}_j\ \hat{b}_j^\dagger\,. \tag{2.46}$$

In both (2.45) and (2.46) the summation is expected to now cover over Hermitian conjugates as necessary.

Having now successfully traced over the bath, we can now return to the

Schrödinger picture. Since,

$$\begin{aligned}
\dot{\tilde{\rho}}_I(t) =& \frac{\partial}{\partial t}\left(e^{i\mathcal{H}_{sys}t/\hbar}\ \rho_S\ e^{-i\mathcal{H}_{sys}t/\hbar}\right) \\
=& \frac{i}{\hbar}\ e^{i\mathcal{H}_{sys}t/\hbar}\ \mathcal{H}_{sys}\ \rho_S\ e^{-i\mathcal{H}_{sys}t/\hbar} - \frac{i}{\hbar}\ e^{i\mathcal{H}_{sys}t/\hbar}\ \rho_S\ \mathcal{H}_{sys}\ e^{-i\mathcal{H}_{sys}t/\hbar} \\
&+\ e^{i\mathcal{H}_{sys}t/\hbar}\ \dot{\rho}_S\ e^{-i\mathcal{H}_{sys}t/\hbar} \\
=& \frac{i}{\hbar}\ e^{i\mathcal{H}_{sys}t/\hbar}\ [\ \mathcal{H}_{sys},\ \rho_S\ ]\ e^{-i\mathcal{H}_{sys}t/\hbar} +\ e^{i\mathcal{H}_{sys}t/\hbar}\ \dot{\rho}_S\ e^{-i\mathcal{H}_{sys}t/\hbar}
\end{aligned}$$

therefore,

$$\dot{\rho}_S = -\frac{i}{\hbar}\ [\ \mathcal{H}_{sys},\ \rho_S\ ] +\ e^{-i\mathcal{H}_{sys}t/\hbar}\ \dot{\tilde{\rho}}_I(t)\ e^{i\mathcal{H}_{sys}t/\hbar}\,. \tag{2.47}$$

Now using our expression for $\dot{\tilde{\rho}}_I(t)$, (2.45),

$$\begin{aligned}
\dot{\rho}_S =& -\frac{i}{\hbar}\ [\ \mathcal{H}_{sys},\ \rho_S\ ] \\
&- \sum_j \lambda_j e^{-i\mathcal{H}_{sys}t/\hbar}(\hat{s}_j^\dagger\ \hat{s}_j\ \tilde{\rho}_I(t) +\ \tilde{\rho}_I(t)\ \hat{s}_j^\dagger\ \hat{s}_j - 2\hat{s}_j\ \tilde{\rho}_I(t)\ \hat{s}_j^\dagger)\ e^{i\mathcal{H}_{sys}t/\hbar} \\
=& -\frac{i}{\hbar}\ [\ \mathcal{H}_{sys},\ \rho_S\ ] \\
&- \sum_j \lambda_j \Big(e^{-i\mathcal{H}_{sys}t/\hbar}\hat{s}_j^\dagger\ \hat{s}_j\ e^{i\mathcal{H}_{sys}t/\hbar}\ \rho_S +\ \rho_S\ e^{-i\mathcal{H}_{sys}t/\hbar}\ \hat{s}_j^\dagger\ \hat{s}_j\ e^{i\mathcal{H}_{sys}t/\hbar} \\
&\qquad - 2\ e^{-i\mathcal{H}_{sys}t/\hbar}\ \hat{s}_j\ e^{i\mathcal{H}_{sys}t/\hbar}\ \rho_S\ e^{-i\mathcal{H}_{sys}t/\hbar}\ \hat{s}_j^\dagger\ e^{i\mathcal{H}_{sys}t/\hbar}\Big) \\
=& -\frac{i}{\hbar}\ [\ \mathcal{H}_{sys},\ \rho_S\ ] - \sum_j \lambda_j \Big(\hat{s}_j^\dagger\ \hat{s}_j\ \rho_S +\ \rho_S\ \hat{s}_j^\dagger\ \hat{s}_j - 2\ \hat{s}_j\ \rho_S\ \hat{s}_j^\dagger\Big)\,,
\end{aligned} \tag{2.48}$$

where we have used (2.42) and (2.43) to eliminate factors of $e^{\pm i\mathcal{H}_{sys}t/\hbar}$. Comparing this expression to that of a closed system, equation (2.19), we see that the effect of the interaction with the bath is a contribution to the master equation of $-\sum_j \lambda_j\ \mathcal{L}(\hat{s}_j)\ \rho_S$.

2.9 The Interaction of Light and Matter: Revisited

To better illustrate the formalism developed in the last section, we now return to the case of a two level atom interacting with an electromagnetic field. Previously we found that when treated as a closed system, with no interactions with its environment, unphysical solutions arise. We now attack the problem as an open system. We allow our atom to have three interactions with the bath, the first of which is the decay of the excited state into the ground state. The second interaction allows the bath to excite the atom from the ground state to the excited state. Lastly, we allow for elastic scattering processes between the bath and the atom. Our interaction Hamiltonian takes the form,

$$\mathcal{H}_{int} = \hbar(g_1\,\hat{a}\hat{b}^\dagger + g_3\,\hat{a}^\dagger\hat{a}\hat{b}^\dagger\hat{b}) + h.c. \tag{2.49}$$

where $\hat{a}$ is the annihilation operator for the two level atom, and $\hat{b}$ is the bath annihilation operator for the background electromagnetic field, and the g_i are yet undetermined coupling constants. Since the third term in our interaction Hamiltonian conserves the number of excitations in our system and in the bath separately, it represents scattering and will be shown to give rise to dephasing in the system (analogous to T_2 relaxation in nuclear magnetic resonance, NMR).

We begin by writing down the master equation in the Schrödinger picture, equation (2.48), with three Lindblad terms, one for each term in our interaction

Hamiltonian,

$$\begin{aligned}\dot{\rho} &= -\frac{i}{\hbar}\,[\,\mathcal{H}_{sys},\ \rho\,] - \lambda_1\,\mathcal{L}(\hat{a})\,\rho - \lambda_2\,\mathcal{L}(\hat{a}^\dagger)\,\rho - \lambda_3\,\mathcal{L}(\hat{a}^\dagger\hat{a})\,\rho \\ &= -\frac{i}{\hbar}\,[\,\mathcal{H}_{sys},\ \rho\,] - \lambda_1(\,\hat{a}^\dagger\,\hat{a}\,\rho + \,\rho\,\hat{a}^\dagger\,\hat{a} - 2\hat{a}\,\rho\,\hat{a}^\dagger) \\ &\qquad - \lambda_2(\,\hat{a}\,\hat{a}^\dagger\,\rho + \,\rho\,\hat{a}\,\hat{a}^\dagger - 2\,\hat{a}^\dagger\,\rho\,\hat{a}) - \lambda_3(\,\hat{a}^\dagger\,\hat{a}\,\rho + \,\rho\,\hat{a}^\dagger\,\hat{a} - 2\,\hat{a}^\dagger\,\hat{a}\,\rho\,\hat{a}^\dagger\,\hat{a}),\end{aligned}$$

where we have used $(\hat{a}^\dagger\,\hat{a})(\hat{a}^\dagger\,\hat{a}) = \hat{a}^\dagger\,\hat{a}$ to simplify the last term. Working in the representation of ρ defined by our basis vectors $|g\rangle\,, |e\rangle$, for the ground and excited states respectively, and once again invoking the rotating wave approximation, the commutator term of the master equation yields,

$$\frac{-i}{\hbar}\,[\,\mathcal{H}_{sys},\ \rho\,] = i\begin{pmatrix} (\Omega\rho_{\rm eg}e^{it\omega} - \Omega^*\ e^{-it\omega}\rho_{\rm ge}) & (\omega_0\rho_{\rm ge} + \Omega e^{it\omega}\,(\rho_{\rm ee} - \rho_{\rm gg})) \\ (\Omega^* e^{-it\omega}\,(\rho_{\rm gg} - \rho_{\rm ee}) - \omega_0\rho_{\rm eg}) & (\Omega^*\rho_{\rm ge}e^{-it\omega} - \Omega\rho_{\rm eg}e^{it\omega}) \end{pmatrix}$$

while the Lindblad terms result in,

$$\begin{aligned}-\lambda_1\,\mathcal{L}(\hat{a})\,\rho - \lambda_2\,\mathcal{L}(\hat{a}^\dagger)\,\rho - \lambda_3\,\mathcal{L}(\hat{a}^\dagger\hat{a})\,\rho = \\ = \begin{pmatrix} 2\lambda_1\rho_{\rm ee} - 2\lambda_2\rho_{\rm gg} & -(\lambda_1+\lambda_2+\lambda_3)\,\rho_{\rm ge} \\ -(\lambda_1+\lambda_2+\lambda_3)\,\rho_{\rm eg} & 2\lambda_2\rho_{\rm gg} - 2\lambda_1\rho_{\rm ee}\,, \end{pmatrix}.\end{aligned}$$

This second matrix is usually referred to as the relaxation matrix, as it describes dissipative processes, and we will often denote it as Γ or $\Gamma(\rho)$. We again assume a solution of the form $\rho_{ge}(t) = \widetilde{\rho}_{ge}(t)\ e^{i\omega t}$ for the off-diagonal components, and we have

$$\begin{aligned}\dot{\rho}_{gg} &= i\Omega\widetilde{\rho}_{\rm eg} - i\Omega^*\widetilde{\rho}_{\rm ge} + 2\lambda_1\rho_{\rm ee} - 2\lambda_2\rho_{\rm gg} \\ \dot{\rho}_{ee} &= -i\Omega\widetilde{\rho}_{\rm eg} + i\Omega^*\widetilde{\rho}_{\rm ge} - 2\lambda_1\rho_{\rm ee} + 2\lambda_2\rho_{\rm gg} \\ \dot{\rho}_{ge} &= i\Omega\,(\rho_{\rm ee} - \rho_{\rm gg}) - (\lambda_1+\lambda_2+\lambda_3 + i(\omega-\omega_0))\,\widetilde{\rho}_{\rm ge}\end{aligned} \tag{2.50}$$

We now examine (2.50) in the absence of a driving field ($\Omega \to 0$), and in the steady state limit ($\dot{\rho} \to 0$). By taking the difference of the first two equations, we have

$$\lambda_1 \rho_{\rm ee}^{(eq)} = \lambda_2 \rho_{\rm gg}^{(eq)} \,, \tag{2.51}$$

where the (eq) superscript is to remind us that this is really an equilibrium equation. However, if the system is in equilibrium at some temperature, T, the ratio N_e/N_g, can also be calculated from the Boltzmann factor as $N_e/N_g = e^{-\hbar\omega_0/k_B T}$. Thus we must have,

$$\frac{\lambda_2}{\lambda_1} = e^{-\hbar\omega_0/k_B T}. \tag{2.52}$$

We see here, as was mentioned in the previous section, that as $T \to \infty$, $\lambda_2 \to 0$. λ_2 arises from an interaction Hamiltonian term of the form $\hat{a}^\dagger\, \hat{b}$, i.e. excitation from the bath. At optical frequencies $\hbar\omega_0 \approx 1$eV, and thus even at room temperature, $k_B T \approx \frac{1}{40}$, this factor is vanishingly small and λ_2 can be taken to be zero.

Returning to (2.50) in the general case, we make the following definitions, let $\frac{1}{\tau} = 2\lambda_1$ and $\frac{1}{T} = (\lambda_1 + \lambda_3)$, and as before define $\Delta_{ge} = \rho_{gg} - \rho_{ee}$. Now, we have,

$$\begin{aligned}
\dot{\Delta}_{ge} &= 2i\Omega\widetilde{\rho}_{\rm eg} - 2i\Omega^*\widetilde{\rho}_{\rm ge} - \frac{\Delta_{\rm ge} - 1}{\tau} \\
\dot{\widetilde{\rho}}_{ge} &= -\left(\frac{1}{T} + i\,(\omega - \omega_0)\right)\widetilde{\rho}_{\rm ge} - i\Omega\Delta_{\rm ge}\,,
\end{aligned}$$

or working in components, $\widetilde{\rho}_{ge} \equiv A + iB$, and assuming that Ω is real,

$$\begin{aligned}
\dot{\Delta}_{ge} &= 4\ \Omega\ B - \frac{\Delta_{\rm ge} - 1}{\tau} \\
\dot{A} &= (\omega - \omega_0)\ B - \frac{A}{T} \\
\dot{B} &= -(\omega - \omega_0)\ A - \Omega\ \Delta_{ge} - \frac{B}{T}\,.
\end{aligned} \tag{2.53}$$

We can solve these equations for the steady state solution by taking the LHS of (2.53) to be zero, and with some straightforward algebra we find,

$$\Delta_{\mathrm{ge}} = \frac{T^2 \left(\omega - \omega_0\right)^2 + 1}{T^2 \left(\omega - \omega_0\right)^2 + 4\tau T \Omega^2 + 1}$$
$$B = -\frac{\Omega\ \Delta_{\mathrm{ge}}}{T\left(\frac{1}{T^2} + \left(\omega - \omega_0\right)^2\right)}$$
$$A = -\frac{\left(\omega - \omega_0\right)\Omega\Delta_{\mathrm{ge}}}{\frac{1}{T^2} + \left(\omega - \omega_0\right)^2}\,.$$

When ρ is viewed as a function of ω, the driving field frequency, we see that both B and Δ_{ge} are peaked at $\omega = \omega_0$ while A changes sign here. This is the resonance condition for the system and comparing these expressions to the well known Lorentzian line shape function, T is evidently the half-width at half-maximum.

We now solve (2.53) in the case where the driving field is on resonance with the atomic transition, so $\omega = \omega_0$,

$$\dot{\Delta}_{ge} = 4\ \Omega\ B - \frac{\Delta_{\mathrm{ge}} - 1}{\tau}$$
$$\dot{A} = -\frac{A}{T}$$
$$\dot{B} = -\Omega\ \Delta_{ge} - \frac{B}{T}\,. \tag{2.54}$$

In this case A becomes uncoupled from the other components and we can solve for it immediately,

$$A(t) = A(0)e^{-t/T}\,.$$

We see that an effect of the elastic scattering interaction with the bath is to cause an exponential decay in the real component of the off-diagonal density matrix element. Since this a measurement of the quantum mixing of the ground and excited states,

then this is indicative of the system losing quantum coherence, i.e. we can say that T leads to decoherence as a pure state will decay into a mixed state at a rate of $\frac{1}{T}$.

Although (2.54) can be solved for B and Δ_{ge} in closed form, the solutions are not very instructive. Instead, we examine the solution in two limits, namely that of a strong field $\Omega >> \tau, T$ and a weak field $\Omega << \tau, T$. In the weak field limit, we neglect the 4 Ω B and Ω Δ_{ge} terms and we find

$$\Delta_{\mathrm{ge}}(t) = \Delta_{\mathrm{ge}}(0)e^{-t/\tau}$$

$$B(t) = B(0)e^{-t/T}\,.$$

Here, because the damping is so much larger than the driving field, the system no longer has the opportunity to oscillate, and B and Δ_{ge} exponentially decay to zero. We say that the system in overdamped.

In strong field limit, we instead neglect the terms $\frac{\Delta_{\mathrm{ge}}-1}{\tau}$ and $\frac{B}{T}$ in (2.54), and take $|g\rangle$ to be the initial state our system is prepared in, and find,

$$\Delta_{\mathrm{ge}}(t) = \cos(2\Omega t)$$

$$B(t) = -\frac{1}{2}\sin(2\Omega t)\,.$$

Here we see that B and Δ_{ge} oscillate at the frequency $2\,\Omega$, which is twice the Rabi frequency (we could have equivalently chosen $\Omega = \frac{\mu E}{\hbar}$ instead of $\Omega = \frac{\mu E}{2\hbar}$). In particular, Δ_{ge} alternates between the values of 0 and 1, which implies that the system oscillates between being fully in the ground state ($\Delta_{ge} = 1$) and fully in the excited state ($\Delta_{ge} = -1$), and between these points, in a 50/50 split between the ground and excited state ($\Delta_{ge} = 0$). At the times when $\Delta_{ge} = 0$, B takes on its

maximal/minimal value of $\pm\frac{1}{2}$ which implies that the system is in a pure state which is consistent with the relaxation terms in (2.54) being ignored. As these oscillations would continue ad infinitum, we say that the system is underdamped in this limit.

In chapter 3, we will model the response of an SQD (an effective two level system), in the presence of an MNP and an applied driving field, both of which will act as a source of electromagnetic radiation incident on the SQD. There, we will see that many features of this simple model will appear with only slight modification when we model SQD-MNP system.

2.10 Computational Technique

We finish this chapter with a few words on how calculations performed for this research were carried out. First, choices are made for the various system parameters. The next step is to calculate, either with a dipole approximation, or with the BEM, the response fields of the MNP, at the location of the SQD. With these fields, along with the Lindblad terms included to model losses, we can write down a master equation for the SQD. This set of coupled differential equations is then solved numerically using Mathematica, usually in both the dynamical limit, as well as the steady state limit. Once these equations are solved, and ρ_{SQD} is found in the desired limit, observable quantities, such as the absorption, can then be calculated. By then varying the parameters that we are free to choose while repeatedly solving the master equation, the system behavior can be fully explored.

Chapter 3

The Optical Response of Strongly Coupled SQD-MNP Systems

In this chapter we are finally ready to theoretically discuss the response of a hybrid nanostructure molecule consisting of a semiconductor quantum dot (SQD) and a metal nanoparticle (MNP) subject to an applied electric field (see Figure 3.1). This system has been studied in the weak coupling regime [20] and in the strong coupling regime [21]. Similar systems have been studied with multiple metal nanoparticles [25, 52], with a nanowire instead of the spherical MNP [26] and also with a metal-dielectric nanoshell [53]. The dipole-dipole coupling between two fluorescent molecules mediated by a chain of silver nanoparticles has also been studied [28]. Plasmon induced transparency has been studied in a system consisting of a three level SQD interacting with a spherical MNP [29].

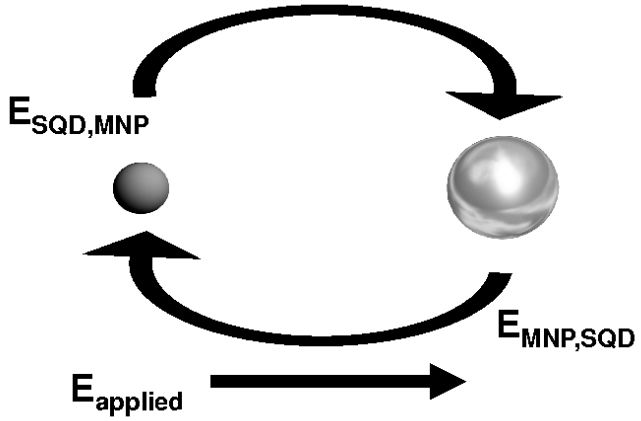

Figure 3.1: An applied field polarizes both the MNP and SQD which in turn allows for a dipole-dipole coupling.

3.1 Introduction

The optical excitations of the SQD are the excitons, with a sharp, discrete response. The SQD acts as a quantum emitter. The strong local plasmonic excitations of the MNP offer a continuous spectrum of response. Local field enhancement in the vicinity of the MNP should provide strong coupling to the neighboring SQD. There is no direct tunneling of charge carriers between the MNP and SQD. However, due to the long-range Coulomb interaction, there is a dipole-dipole interaction that will allow them to couple and will lead to excitation transfer.

The discrete excitons coupled with the broad response of the plasmons should allow for the appearance of exotic hybrid states and clear signatures for their optical response. We will see that as a damped driven oscillator, the SQD response to driving fields changes rapidly from in-phase to out-of-phase near the SQD resonance. Rapid variations in hybrid response are expected near the SQD resonance. Effects depending on the interference between applied and induced fields are extremely sensitive to this change from in-phase to out-of-phase SQD response, providing dramatic signatures from the hybrid response.

Previously, the weak coupling regime was studied in [20]. In the weak field/weak coupling limit (driving field of $1\mathrm{W/cm^2}$), a shift and broadening of the peak in the energy absorption spectrum due to the coupling between the exciton in the SQD and the plasmon in the MNP was found. In the strong field/weak coupling limit, an asymmetrical Fano shape, develops in the energy absorption spectrum.

Here, we will examine the strong coupling regimes, in particular probing fur-

ther the strong applied field limit. We find that the behavior is much more complex than previously determined [20]. When we explore the relationship between the size of the constituents and the response of the system, we find that in addition to the regime for weak coupling which was previously explored, there are three new regimes of system behavior in the strong coupling limit. These four (in total) distinct regimes of behavior in the strong field limit each exhibit novel properties and we will look at each.

In the first regime the energy absorption spectrum displays an asymmetrical Fano shape (as previously predicted in [20]). It occurs when there is interference between the applied field and the induced field produced by the SQD at the MNP. As the SQD is increased in size (thus the coupling is increased), the asymmetrical Fano effect of region I is modified by the appearance of an additional peak with a deep minimum between the peaks [21]. Here, the induced local field at the MNP becomes larger than the applied field, for frequencies near the SQD resonance. As such, the interference of the the response field of the SQD, with the applied electric field, now results in a sign change in the net electric field at the MNP above resonance where the two fields are out-of-phase. An exciton induced transparency (EXIT) arises in the MNP response when there is nearly complete destructive interference between these two fields acting on the MNP.

When the MNP and SQD are further increased in size, the hybrid behavior transitions between regions II and III. In this regime, there is a discontinuous jump in response of the system (in both the diagonal and off-diagonal density matrix elements) as the driving frequency is varied [22]. Moreover, the response of the SQD

is highly suppressed above resonance in this transition region. The discontinuous response and suppression arise because the SQD acts as a driven (quantum) oscillator. Below resonance the dipole moment of the SQD is in phase with the driving field and above resonance it is 180° out of phase. The phase change at resonance drastically alters the hybrid response when crossing the resonance.

Finally, in region III, the system response becomes nonlinear. This nonlinearity is due to significant self interaction of the SQD (feedback through the MNP). In this regime, there exists multiple steady state solutions leading to a bistability with one of the stable solutions having a discontinuous absorption spectrum [21]. In this chapter will explore these four regimes in detail and set bounds on each.

The layout of this chapter is as follows. In section 2, we discuss the system in detail. We use a density matrix approach to treat the SQD, while the MNP is taken as a classical dielectric. We also calculate the energy absorption of the MNP and provide details on how numerical calculations were carried out. In section 3 the Fano-like behavior of the system in region I will be discussed. In section 4, the exciton induced transparency of region II is introduced. We then discuss the suppressed response of the SQD that occurs in the transition region, in section 5. In section 6, we look at region III, where the system response is dominated by nonlinear effects and bistability can occur. In section 7, we will investigate the roll that the phasors and interaction strengths play in determining which regime of system behavior is present. In section 8, we examine how the polarization of the incident light effects the system behavior. Finally, a summary of findings is presented in section 8.

3.2 Setup

As in [20], we consider a spherical SQD with radius r interacting with a spherical MNP of radius a, separated by a distance R (as shown in Figure 3.1). The entire system is subject to an applied electric field $E = E_0 \cos(\omega t)$. We assume that all distances are small enough that retardation effects can be ignored and that the applied field is large enough to be treated classically.

The SQD is modeled as a spherical semiconductor with dielectric constant ϵ_S, and a 2-level atom-like quantum system at the center of it. This dielectric constant will produce a screening of the field incident on the SQD. We treat the exciton quantum mechanically in the density matrix formalism with exciton energy $\hbar\omega_0$, and transition dipole moment μ. In the dipole limit for a spherical dot, only the three bright excitons (one for each optical axis) participate in the interaction. By choosing the direction of the applied field to be either perpendicular or parallel to the axis of our system, we in turn only excite the exciton polarized perpendicular or parallel to the system axis. Dark excitons do contribute to the exciton lifetime however. We treat the MNP as a classical spherical dielectric particle with dielectric function $\epsilon_M(\omega)$.

The Hamiltonian for the two level SQD, $\mathcal{H}_{SQD}$, is

$$\mathcal{H}_{SQD} = \hbar\omega_0 \hat{a}^\dagger \hat{a} - \mu E_{SQD} \left(\hat{a} + \hat{a}^\dagger\right) , \tag{3.1}$$

where $\hat{a}$ and $\hat{a}^\dagger$ are the exciton creation and annihilation operators. E_{SQD} is the total electric field felt by the SQD and consists of the applied, external field, E, and the induced, internal field, produced by the polarization of the MNP, $E_{MNP,SQD}$. In

the dipole limit, E_{SQD} is

$$E_{SQD} = \frac{1}{\epsilon_{\text{effS}}}\big(E + \frac{1}{4\pi\epsilon_B}\frac{s_\alpha P_{MNP}}{R^3}\big) \ , \tag{3.2}$$

where $s_\alpha = 2(-1)$ when the applied field is parallel (perpendicular) to the major axis of the system and $\epsilon_{\text{effS}} = \frac{2\epsilon_B+\epsilon_S}{3\epsilon_B}$ accounts for the screening of the dielectric material. ϵ_B is a background dielectric constant which we could assume to be from the material that our system in embedded in. Being careful to separate out the negative and positive frequency contributions, the polarization of the MNP is (see [54]),

$$P_{MNP} = (4\pi\epsilon_B)a^3\Big[\gamma\ \widetilde{E}^{(+)}_{MNP}\ e^{-i\omega t} + \gamma^*\ \widetilde{E}^{(-)}_{MNP}\ e^{i\omega t}\Big] \ .$$

$\widetilde{E}^{(+)}_{MNP}$ and $\widetilde{E}^{(-)}_{MNP}$ are the positive and negative frequency parts of the electric field felt by the MNP. Note that the choice of the sign convention is such that $\text{Im}[\epsilon_m(\omega)] > 0$ for $\omega > 0$. The total field acting on the MNP, E_{MNP}, is just

$$E_{MNP} = (E + \frac{1}{4\pi\epsilon_B}\frac{s_\alpha P_{SQD}}{\epsilon_{\text{effS}} R^3}) \ , \tag{3.3}$$

where $\gamma = \frac{\epsilon_M(\omega)-\epsilon_B}{2\epsilon_B+\epsilon_M(\omega)}$.

We make use of the density matrix ρ to calculate the polarization of the SQD. We label the ground state of our SQD (no exciton) as level 1 and the excited state (one exciton) we label as level 2. We then have $P_{SQD} = \mu(\rho_{12} + \rho_{21})$ (as we saw in chapter 2, see also [48]). Factoring out the high frequency time dependence of the off-diagonal terms of the density matrix, we write

$$\begin{aligned} \rho_{12} &= \widetilde{\rho}_{12}\ e^{i\omega t} \\ \rho_{21} &= \widetilde{\rho}_{21}\ e^{-i\omega t} \ . \end{aligned} \tag{3.4}$$

Putting this into E_{MNP}, we have

$$\begin{aligned} E_{MNP} &= (\frac{E_0}{2} + \frac{1}{4\pi\epsilon_B}\frac{s_\alpha \mu}{\epsilon_{\text{effS}} R^3}\widetilde{\rho}_{21})\ e^{-i\omega t} \\ &\quad +(\frac{E_0}{2} + \frac{1}{4\pi\epsilon_B}\frac{s_\alpha \mu}{\epsilon_{\text{effS}} R^3}\widetilde{\rho}_{12})\ e^{i\omega t}\ . \end{aligned}$$

Returning to P_{MNP},

$$\begin{aligned} P_{MNP} &= (4\pi\epsilon_B)a^3\Bigg[\gamma\ \left(\frac{E_0}{2} + \frac{1}{4\pi\epsilon_B}\frac{s_\alpha \mu}{\epsilon_{\text{effS}} R^3}\widetilde{\rho}_{21}\right)\ e^{-i\omega t} \\ &\quad + \gamma^*\ \left(\frac{E_0}{2} + \frac{1}{4\pi\epsilon_B}\frac{s_\alpha \mu}{\epsilon_{\text{effS}} R^3}\widetilde{\rho}_{12}\right)\ e^{i\omega t}\ \Bigg]. \end{aligned}$$

We can now write the field acting on the SQD as,

$$E_{SQD} = \frac{\hbar}{\mu}\Big\{(\Omega + G\,\widetilde{\rho}_{21})\,e^{-i\omega t} + (\Omega^* + G^*\,\widetilde{\rho}_{12})\,e^{i\omega t}\Big\}\ , \tag{3.5}$$

where we have defined

$$\begin{aligned} G &= \frac{s_\alpha^2 \gamma a^3 \mu^2}{4\pi\ \epsilon_B \hbar\ \epsilon_{\text{effS}}^2\ R^6} \\ \Omega &= \frac{E_0 \mu}{2\hbar\epsilon_{\text{effS}}}(1 + \frac{\gamma a^3 s_\alpha}{R^3}). \end{aligned}$$

G arises when the applied field polarizes the SQD, which in turn polarizes the MNP and then produces a field to interact with the SQD. Note that it is proportional to μ^2 rather than μ as for Ω. Thus, this can be thought of as the self-interaction of the SQD because this coupling to the SQD depends on the polarization of the SQD. The first term in Ω is just the direct coupling to the applied field and the second term is the field from the MNP that is induced by the applied field.

Furthermore, we can see that both of these terms depend on γ, as we first saw in chapter 2. There, we saw that γ determined the response field outside of the

MNP, in the case of a planewave source, and in the case of a dipole source. As we begin to explore the parameter space of this system, it's important to keep in mind that these coupling constants, G and Ω, are determined by the product of the MNP response fields, and the SQD dipole moment.

We solve the master equation,

$$\dot{\rho} = \frac{i}{\hbar}[\rho, \mathcal{H}_{SQD}] + \Gamma(\rho) \ , \tag{3.6}$$

where $\Gamma(\rho)$ is the relaxation matrix. To obtain an expression for $\Gamma(\rho)$, we will assume two bath interactions for our SQD. First, we assume the exciton will interact with phonons inside the SQD through elastic electron-phonon coupling. As this is a scattering process where energy is conserved, the minimal SQD-phonon coupling must be of the form $\hat{a}^\dagger \, \hat{a} \ \hat{b}^\dagger \, \hat{b}$. We saw in chapter 2 that this requires a Lindlad term of $\mathcal{L}(\hat{a}^\dagger \, \hat{a})$. Next, we assume a photon bath can induce emission in the SQD. Similarly, this leads to a Lindlad term of $\mathcal{L}(\hat{a})$. As we're considering an optical system at low temperatures, we can ignore bath induced excitation.

Thus, we can write our relaxation matrix as

$$\begin{aligned}\Gamma(\rho) =& \lambda_1 \mathcal{L}(\hat{a}) + \lambda_2 \mathcal{L}(\hat{a}^\dagger \, \hat{a}) \\ =& \begin{pmatrix} 2\lambda_1 \rho_{22} & -(\lambda_1 + \lambda_2)\, \rho_{12} \\ -(\lambda_1 + \lambda_2)\, \rho_{21} & -2\lambda_1 \rho_{22} \, , \end{pmatrix}.\end{aligned}$$

To put this in more familiar form, we take $\tau_0 = \frac{1}{2\lambda_1}$ and $T_0 = \frac{1}{\lambda_1 + \lambda_2}$. This then becomes,

$$\Gamma(\rho) = \begin{pmatrix} \frac{1-\rho_{11}}{\tau_0} & -\frac{\rho_{12}}{T_0} \\ -\frac{\rho_{21}}{T_0} & -\frac{\rho_{22}}{\tau_0} \, , \end{pmatrix}.$$

where $\rho_{11} + \rho_{22} = 1$ has been used in order to write $(\Gamma(\rho))_{11}$ in terms of ρ_{11} for the sake of convenience. From this we see that τ_0 will lead to a mixing between ρ_{11} and ρ_{22}. This is spontaneous decay of the exciton. Also, we see that T_0 will cause losses in the off-diagonal density matrix elements, and thus causes dephasing. Both processes contribute to a loss of coherence in the system.

We now write the density matrix elements as

$$\widetilde{\rho}_{12} = A + iB$$

$$\widetilde{\rho}_{21} = A - iB$$

$$\Delta = \rho_{11} - \rho_{22} \ ,$$

where Δ is the population difference between the ground and excited states. To solve (3.6), we make the rotating wave approximation. When changing the Hamiltonian to the interaction picture we keep terms that oscillate like $e^{i(\omega-\omega_0)t}$ and neglect terms that oscillate like $e^{i(\omega+\omega_0)t}$. Making use of our definitions and the rotating wave approximation, we come to the set of coupled differential equations,

$$\begin{aligned}
\dot{A} &= -\frac{A}{T_0} + (\omega - \omega_0)B - \Big(\Omega_I + G_I A - G_R B\Big)\Delta \\
\dot{B} &= -\frac{B}{T_0} - (\omega - \omega_0)A - \Big(\Omega_R + G_R A + G_I B\Big)\Delta \\
\dot{\Delta} &= \frac{1-\Delta}{\tau_0} + 4\Omega_I A + 4\Omega_R B + 4G_I(A^2 + B^2),
\end{aligned} \tag{3.7}$$

where G_R, G_I, Ω_R and Ω_I are the real and imaginary parts of G and Ω respectively.

In the steady state limit we set the left hand side of (3.7) to zero. Due to the nonlinear nature of these equations, more than one steady state solution can exist for certain values of the parameters. In these regions we must solve the full set of

dynamical equations (3.7), allowing them to evolve from the initial conditions for times on the order of 10 ns to reach the steady state. This allows us to identify the dependence of the steady state on the starting conditions. Except where noted, evolution for 10 ns was sufficient to reach steady state in cases considered.

3.2.1 Energy

The rate at which energy is absorbed by our system consists of two parts, Q_{SQD} and Q_{MNP}. The SQD absorbs energy by the creation of an exciton which is followed by a decay. The absorption rate is then just $Q_{SQD} = \hbar\omega_0\rho_{22}/\tau_0$. To calculate the energy absorbed by the MNP, we take the time average of the volume integral, $\int \mathbf{j}\cdot\mathbf{E}\, dv$, where $\mathbf{j}$ is the current density and $\mathbf{E}$ is the electric field inside the MNP. The electric field incident on the MNP is the applied field plus the field due to the polarization of the SQD,

$$\begin{aligned} E_{MNP}^{(outside)} &= E + \frac{1}{4\pi\epsilon_B}\frac{s_\alpha\mu}{\epsilon_{\text{effS}}R^3}(\rho_{12}+\rho_{21}) \\ &= (E_0 + \frac{s_\alpha\mu\, A}{2\pi\epsilon_B\epsilon_{\text{effS}}R^3})\,\cos\omega t - \frac{s_\alpha\mu\, B}{2\pi\epsilon_B\epsilon_{\text{effS}}R^3}\,\sin\omega t \\ &= E_C\, cos(\omega t) - E_S\,\sin(\omega t)\ , \end{aligned} \tag{3.8}$$

where

$$E_C = E_0 + \frac{s_\alpha\mu}{2\pi\epsilon_B\epsilon_{\text{effS}}R^3}A$$

is the component of the field that is in phase with the applied field and

$$E_S = \frac{s_\alpha\mu}{2\pi\epsilon_B\epsilon_{\text{effS}}R^3}B$$

is 90° out of phase with the applied field. Separating the positive and negative frequency parts of the field, we can write the field inside the MNP as

$$E_{MNP}^{(inside)} = \frac{E_C - iE_S}{2\epsilon_{\text{effM}}} e^{-i\omega t} + \frac{E_C + iE_S}{2\epsilon_{\text{effM}}^*} e^{i\omega t} \ ,$$

where $\epsilon_{\text{effM}} = \frac{2\epsilon_B + \epsilon_M}{3\epsilon_B}$.

We calculate the current density of the MNP from the derivative of its polarization, P_{MNP}. Written in terms of E_C and E_S, P_{MNP} is

$$P_{MNP} = 2\pi a^3 \epsilon_B \Big(\gamma \left(E_C - iE_S \right) e^{-i\omega t} + \gamma^* \left(E_C + iE_S \right) e^{i\omega t} \Big) \ .$$

Since we are assuming that we have factored out the fast varying part of the density matrix in (3.4) and we are in the steady state limit, we take the time derivatives of A and B to be zero and we then have for the current density, j,

$$j = \frac{2\pi i \omega \epsilon_B a^3}{\mathcal{V}} \Big(\gamma^* \left(E_C + iE_S \right) e^{i\omega t} - \gamma \left(E_C - iE_S \right) e^{-i\omega t} \Big) \ ,$$

where $\mathcal{V}$ is the volume of the MNP.

We can now calculate $Q_{MNP}(t)$,

$$\begin{aligned} Q_{MNP}(t) &= \int \mathbf{j} \cdot \mathbf{E} \ dv \\ &= i\pi \epsilon_B \omega a^3 \Big(\frac{\gamma^*}{\epsilon_{\text{effM}}} (E_C + iE_S)^2 e^{2i\omega t} - \frac{\gamma}{\epsilon_{\text{effM}}^*} (E_C + iE_S)^2 e^{-2i\omega t} \\ &\qquad - 2iIm\Big[\frac{\gamma}{\epsilon_{\text{effM}}^*} \Big] (E_C + iE_S)(E_C - iE_S) \Big) \ . \end{aligned}$$

Taking the time average of this result over the period of fast oscillation yields Q_{MNP},

$$Q_{MNP} = 2\pi \epsilon_B \omega a^3 Im\Big[\frac{\gamma}{\epsilon_{\text{effM}}^*} \Big] (E_C^2 + E_S^2) \ . \tag{3.9}$$

Thus, E_C and E_S are key in determining the shape of the response. Since E_S is out of phase with the applied field, it will typically be substantially smaller

than E_C. However, in the strongest coupling regime we will look at, E_C and E_S are comparable.

3.2.2 Numerical Calculations and Parameter Values

We now focus on the large field limit as defined in [20] (intensity of 10^3 W/cm^2) with E parallel to the axis of our SQD-MNP molecule i.e., $s_\alpha = 2$ and we take the dielectric constant of the background to be $\epsilon_B = \epsilon_0$. In this limit, most of the energy of the system is concentrated in the MNP so our focus will be on the field felt by the MNP. However, at strong coupling, the self-interaction of the SQD is relatively large and thus will become important in determining the behavior of the system.

For the MNP, we take $\epsilon_M(\omega)$ as the bulk dielectric constant of gold as found experimentally [55]. For a small, spherical, gold MNP, the response has a broad plasmon peak near 2.4 eV with a width of approximately 0.25 eV. We will let the radius of the MNP vary between 3 and 8 nm.

For the SQD, we take the relaxation times to be $\tau_0 = 0.8$ ns and $T_0 = 0.3$ ns, and we take $\epsilon_S = 6\,\epsilon_0$. For the exciton resonance frequency we take it to be 2.5 eV which is near the broad plasmon frequency of gold and will allow for strong coupling between them. For the MNP size regime we will consider, the plasmon resonance for a sphere varies little with particle size. However, the size, shape and material of the SQD strongly determine both the exciton energy level and its dipole moment. We consider the simplest model and ignore this size dependence. While this is clearly an oversimplification, it will allow us to identify the range of optical signatures which

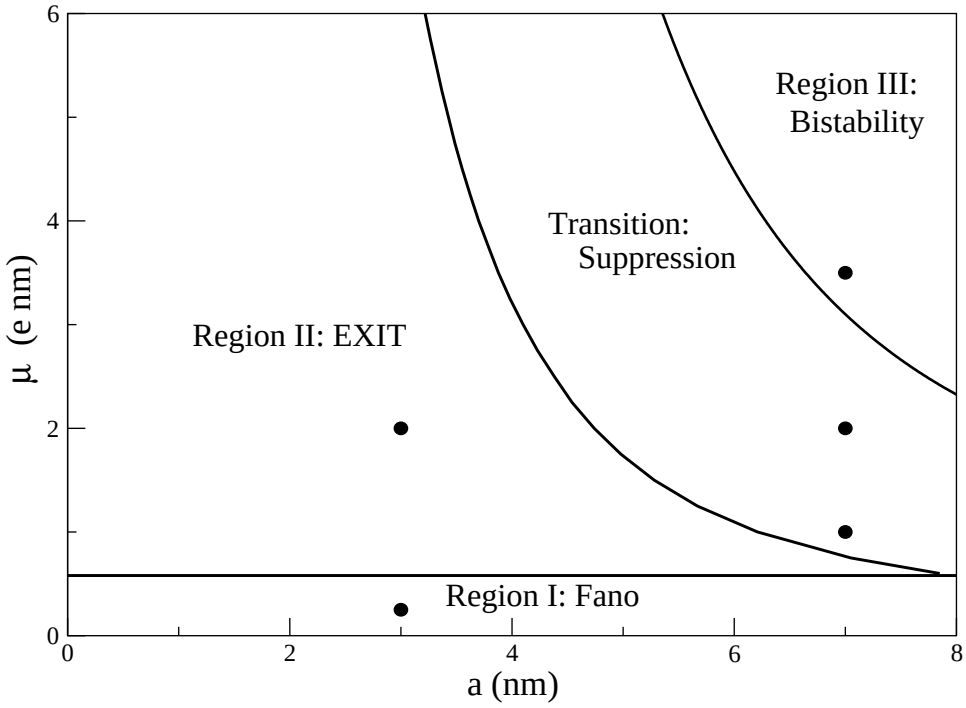

Figure 3.2: μ vs. a phase diagram for $R = 13\,\text{nm}$ in the strong field limit. Outlined are the four distinct regions of system response, namely Fano, EXIT, Suppression and Bistability. Points denote parameter values for which the system response is plotted in Figures 3.3, 3.4, 3.6, 3.8, and 3.9.

are possible in the strong-field limit.

Recent measurements of SQD dipole moments have yielded values of $\approx 1\,\text{e}\cdot\text{nm}$ for self-assembled QDs[56] and several times that for interface fluctuation QDs[57]. For the dipole moment of the SQD, we let it vary between 0.25 and $6.0\,\text{e}\cdot\text{nm}$, corresponding to a SQD size of 2 to 30 nm. For the purposes of our investigation, this range is a reasonable coverage of the observed values that allows us to test the full spectrum of behavior.

By manipulating a and μ, which are the sizes of the MNP and SQD respectively, we can change the relative strengths of the local fields, and thus change the

strengths of the three different couplings (G and the two terms that make up Ω). Looking at the solutions to the differential equations, (3.7), both dynamically and in the steady state limit, there are four distinct regimes of behavior in the a vs. μ parameter space (see Figure 3.2). We now discuss each of these regimes in turn.

3.3 Region I: Nonlinear Fano Effect

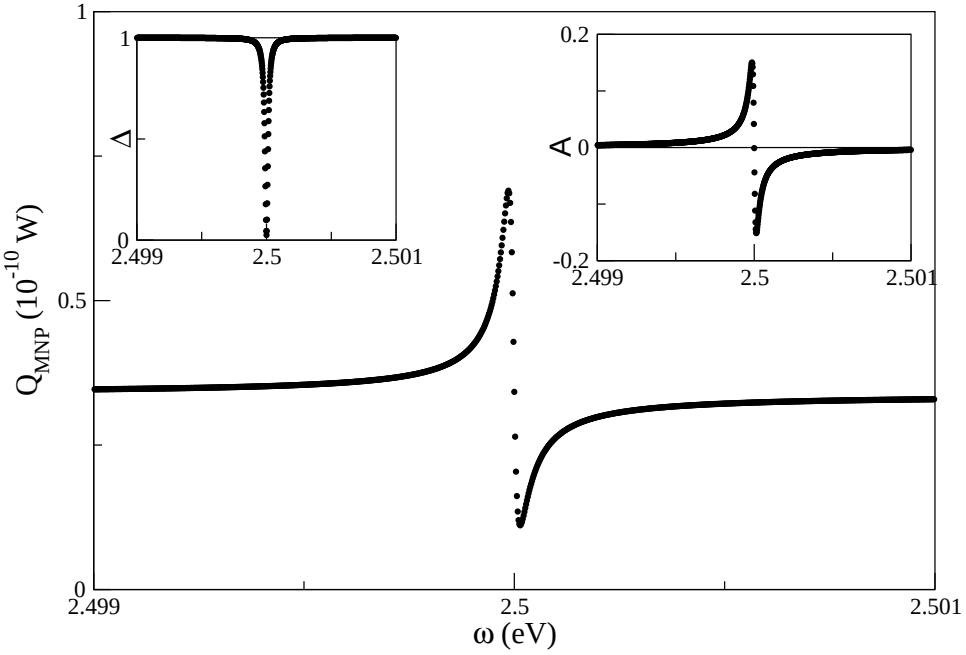

Figure 3.3: Region I. Absorption rate of the MNP, Q_{MNP}, shows a Fano shape in the response due to the phase change in dipole moment of the SQD. This phase change is shown in the real part of the SQD dipole moment in the right inset. Left inset shows the sharp dip in the population difference at resonance. Parameter values used in the calculation were $R = 13$ nm, $a = 3\,\text{nm}$, and $\mu = 0.25\,\text{e}\cdot\text{nm}$.

Region I, the regime of weakest coupling between the SQD and MNP, is discussed extensively in [20], but here is a brief overview for completeness. In the

strong field limit, the exciton is strongly driven at resonance, overcomes the damping, and the population difference, Δ, is zero. The energy absorption spectrum of the MNP displays an asymmetrical Fano shape (see Figure 3.3). It occurs when there is interference between the applied field and the induced field produced by the SQD at the MNP.

In this region, the dominant component of the field acting on the MNP is E_C, with E_S being negligible at weak coupling. It is important to note that in region I, E_C is dominated by the applied field. Although there is interference, E_0 is always greater than $\frac{s_\alpha \mu}{2\pi\epsilon_B \epsilon_{\text{effS}} R^3} A$ (in region II, the local field can be larger than the driving field). The interference changes from constructive to destructive at resonance where the sign of A changes (see Figure 3.3). Below resonance A is positive and above resonance it is negative. Since A is the real part of the SQD dipole moment it determines the phase of the local field acting on the MNP. Thus, below resonance the local field is in phase with the applied field and above resonance the local field is 180° out of phase with the applied field. This type of phase change is a common feature of a damped driven oscillator.

3.4 Region II: Exciton Induced Transparency (EXIT)

When the coupling is increased by increasing μ, the character of the Fano response becomes more complicated. Region II is characterized by an additional peak that appears in the Fano line shape of region I (see Figure 3.4). This second peak occurs where the minimum of E_C in (3.9) crosses through zero (in this region

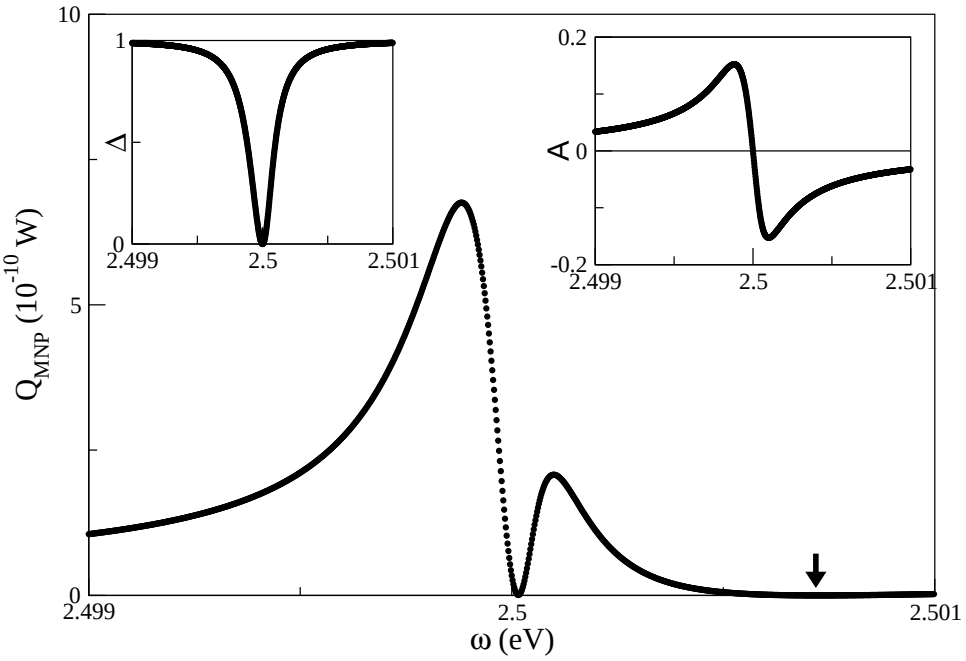

Figure 3.4: Region II. Absorption rate of the MNP, Q_{MNP}, shows an exciton induced transparency due to the phase change in the dipole moment of the SQD when the local field incident on the MNP from the SQD is larger than the applied field. Right inset shows the real part of the SQD dipole moment which undergoes a phase change at resonance. Left inset shows the dip in the population difference at resonance. All three plots show a general broadening relative to region I. The arrow indicates the second dip in Q_{MNP} which is cannot be discerned on this scale. $R = 13$ nm, $a = 3\,\text{nm}$, $\mu = 2\,\text{e}\cdot\text{nm}$.

of parameter space, E_S is still an order of magnitude smaller) (see Figure 3.5). For this sign change to occur, the magnitude of the local field, $\frac{s_\alpha \mu}{2\pi\epsilon_B \epsilon_{\text{effS}} R^3} A$, must be larger than the applied field, E_0, over a range of frequencies and must be out-of-phase with E_0 over these frequencies. As a consequence, E_C changes sign just above resonance (the dip in Figure 3.4). E_C changes sign again, well above resonance (the barely visible second dip in Figure 3.4), when the induced local field again becomes weaker than the applied field. When E_C changes sign at these two locations, the field on the MNP is nearly completely canceled and the metal becomes reflective. The absorption remains finite only because the small out-of-phase component E_S is non-zero. Because this is an interference effect between the driving field and the field produced by the SQD, this is an exciton induced transparency (EXIT) in the MNP that is due to the phase change at resonance of the driven SQD oscillator.

By setting $E_C = 0$, we find the line separating region I from region II to be

$$\mu(a) = -\frac{2\pi\epsilon_0 \epsilon_{effS} R^3 E_0}{s_\alpha A}. \tag{3.10}$$

A varies with a slowly over the parameter space and thus $\mu(a)$ is approximately constant as a function of a. At the frequency where this double peak occurs, A has a typical value of -0.15. Using this value for A, we can estimate this line to be approximately $\mu = 0.59$ e nm.

When this line is found by numerically solving the differential equations repeatedly for different values of a and μ in this region, this line is determined to be $\mu(a) = 0.574$ e nm plus a small exponential term (negligible for $a < 10$ nm). This agrees extremely well with the value calculated by analyzing the behavior of

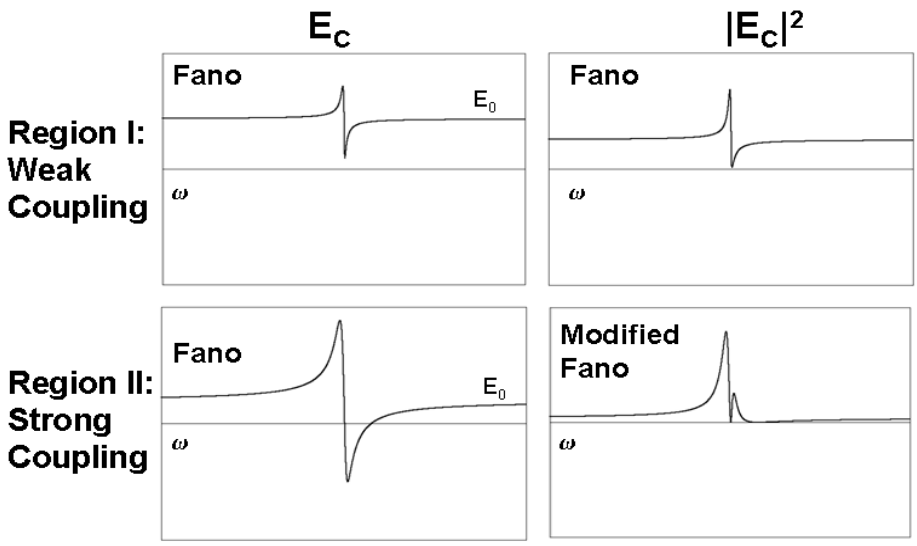

Figure 3.5: The emergence of the modified Fano shape is due to E_C crossing zero. This occurs when the internal field can be larger than the external field. When this field is then squared to find the absorption, the location where E_C crosses zero can produce a transparency.

E_C. Note that for all calculations presented in [20], the value of μ that was used in numerical calculations was 0.65 e nm, which falls nearly on this boundary.

When we let μ and a vary in such a way as to approach region I from region II, this second peak decreases in size. Conversely, moving away from region I, just inside region II, this second peak becomes larger. The transition between these two regions is smooth i.e., the extra peak vanishes at the transition boundary (see Figure 3.5).

3.5 Transition Region: Suppression

In region I and II, interference between the applied field and the induced field due to the polarization of the SQD caused a phase shift in the net electric

field incident on the MNP at resonance and an asymmetry in the response of the MNP. However, this asymmetry is not manifested in the response of the SQD, i.e. Δ, (see Figure 3.4 for example) because the SQD does not couple directly to the field produced by the polarization of the SQD. However, this field does couple to the MNP, which in turn polarizes and produces a field that couples to the SQD. This self-interaction of the SQD is G in Eq. (3.5). If the self-interaction becomes significant, there will also be non-negligible interference of the electric fields at the SQD. The interference then can suppress or enhance the response of the SQD.

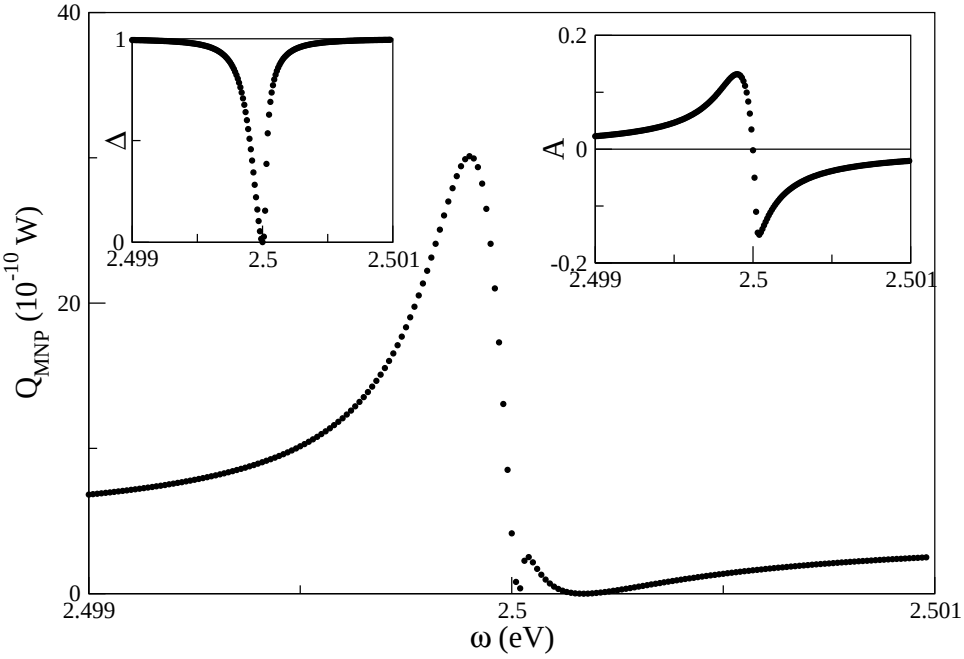

Figure 3.6: Transition region: weak suppression. Here we see the beginning of the suppression in the response of the SQD, apparent in a slight asymmetry in Δ. $\Gamma_b = 98\ \mu$eV, $\Gamma_a = 37\ \mu$eV, with suppression factor $S = 2.65$. The double peaked EXIT structure is still visible, but the second peak is much smaller relative to the main peak. The system response is also much broader than in region I or II. Parameter values $R = 13\,$nm, $a = 7\,$nm, and $\mu = 1\,$e·nm.

The transition region between regions II and III is characterized by this suppression of the response of the SQD above resonance. To measure the extent of the suppression, we measure the width of Δ, both above and below resonance at half maximum (half width, half max). We label these two half widths, Γ_a and Γ_b, for above and below resonance respectively. We then define the suppression factor, S, to be ratio of these two widths, $S = \Gamma_b/\Gamma_a$. We choose $S = 2$ to define the boundary of the suppression region. However, note that the characteristic double peaked EXIT structure still exists for S values greater than 2. The double peak structure of region II disappears only once the suppression becomes so strong that the response function becomes discontinuous.

For a fixed value of the MNP radius (a=7 nm) and with a small value of the SQD dipole moment ($\mu = 1\,\mathrm{e{\cdot}nm}$), we see the beginning of the suppression above resonance ($S = 2.65$). The population difference, Δ, is continuous as is the SQD dipole moment (see Figure 3.6). Furthermore, we see that the double peaked EXIT structure is still present, but the second peak is much smaller relative to the main peak, and the window of transparency has shrunk. This last effect is due to the system response also being much broader than in region I or II.

To see how the suppression develops, we need to look at the composition of the electric field that is incident on the SQD. The field felt by the SQD, (Equation (3.5)), is composed of two parts, $\rho_{12}G$ and Ω. Ω consists of the direct coupling to the applied field, E, as well as the response of the MNP to the applied field. The self-interaction term scales as $\sim \mu^2\, a^3$ and the response of the MNP to the applied field scales as $\sim \mu\, a^3$. As μ is increased, the self-interaction becomes a

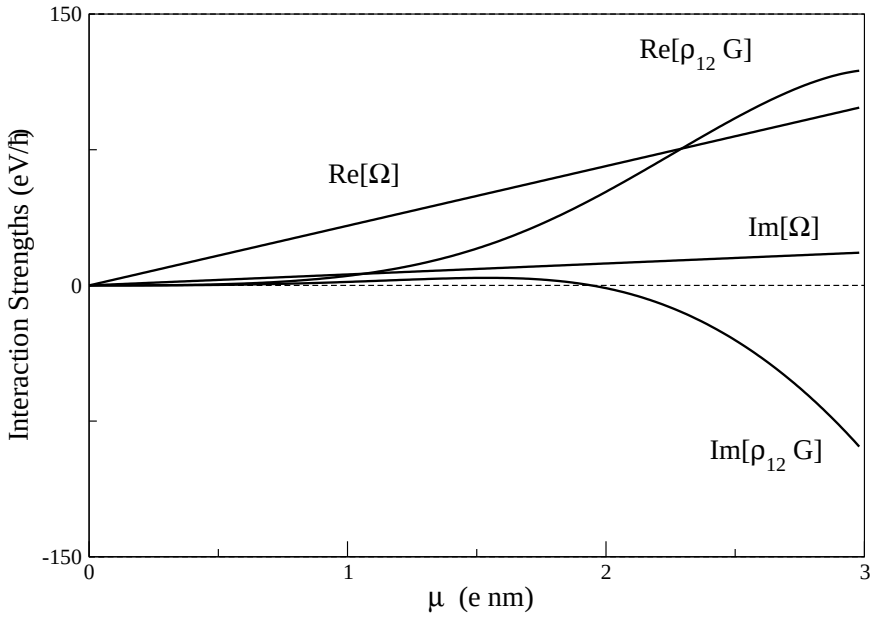

Figure 3.7: The relative strengths of the two main interactions that drive the SQD. $\rho_{12}G$, the self interaction, and Ω, the applied field and the MNP response to the applied field, vs μ for fixed MNP radius ($a = 7\,\text{nm}$) and frequency ($\omega = 2.5\,\text{eV}$). Note: G and Ω are nearly constant over the range of frequencies that we are interested in due to the broad plasmon peak.

significant contribution to the total field (see Figure 3.7). For weak suppression, $a = 7\,\text{nm}$, $\mu = 1\,\text{e·nm}$ (as in Figure 3.6) we see that the self-interaction is an order of magnitude smaller than Ω. Because the phase of the self-interaction depends on the phase of ρ_{12}, we again have interference, this time at the SQD between the self-interaction and the driving field (including the indirect contribution through the MNP).

As μ is increased to $2\,\text{e·nm}$ we see the above resonance suppression grows so strong ($S = 72.3$) that it forces a discontinuity in response of the MNP and the diagonal density matrix elements, as well as in the off-diagonal elements (the dipole

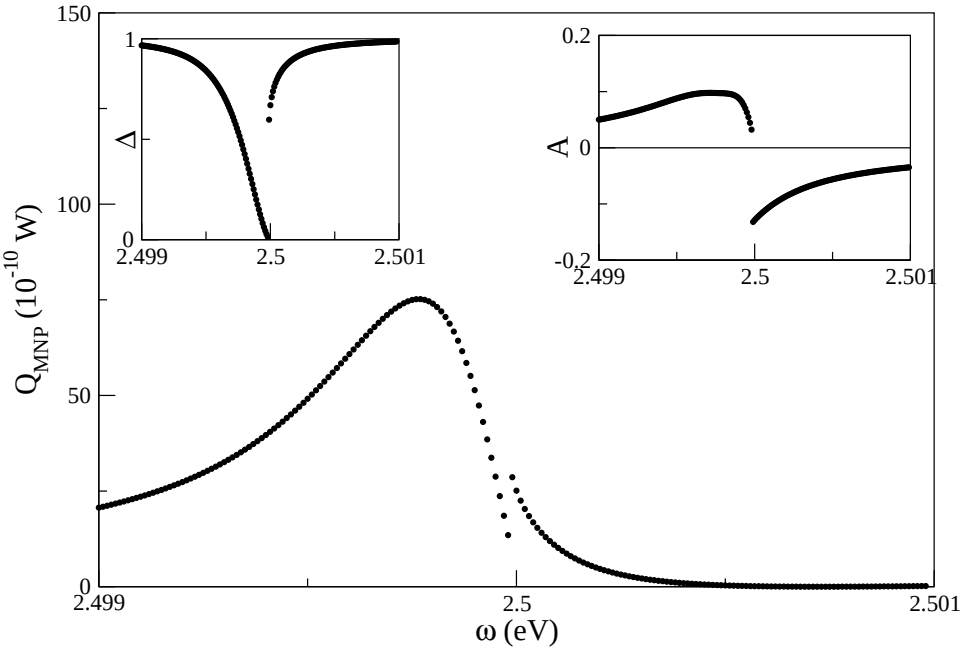

Figure 3.8: Transition region: Strong suppression. Here the suppression has grown large enough that a discontinuity has developed in the diagonal and off-diagonal density matrix elements as well as the energy absorption of the MNP. Also, the transparency in the response due to EXIT no longer approaches zero due to extreme broadening of the response. $\Gamma_b = 217$ μeV, $\Gamma_a = 3$ μeV, $S = 72.3$. Parameters: $R = 13$ nm, $a = 7\,\text{nm}$, $\mu = 2\,\text{e}\cdot\text{nm}$.

moment of the SQD) (see Figure 3.8). In this regime of strong suppression, we see that the self-interaction is of the same order of magnitude as Ω (see Figure 3.7).

As μ is further increased, the suppression increases along with the discontinuity, and the resonance of the SQD begins to shift to lower energies. The location of phase change in ρ_{12} also splits based on the initial conditions of the system (see Figure 3.13 and section 3.7.1), much like we will see in region III (which is discussed in section 3.6). Further increase in μ results in further shifts to the resonance of the SQD. This causes the suppression to eventually disappear. The discontinuity however, remains locked in for certain initial conditions, causing the bistability we will see in the next section. As we will see there, at a large value of the dipole moment, $\mu = 3.5\,\mathrm{e{\cdot}nm}$, which is just inside region III, S is reduced to 1.7 (see Figure 3.9).

3.6 Region III: Bistability

When the coupling is further increased by increasing both μ and a, a region of bistable response emerges (region III). In this limit, the field that is produced by the SQD and then reflected off the MNP and back onto the SQD (the self-interaction of the SQD) is sufficiently strong to introduce nonlinear effects into the response. This, combined with an increased broadening due to the increased field strength, causes the double peaked EXIT structure to disappear (see Figure 3.9).

Most importantly, region III is characterized by bistability in the steady state solutions. For the same values μ and a, different initial conditions of ρ lead to different steady states (compare Figures 3.9 and 3.10). This bistability only exists

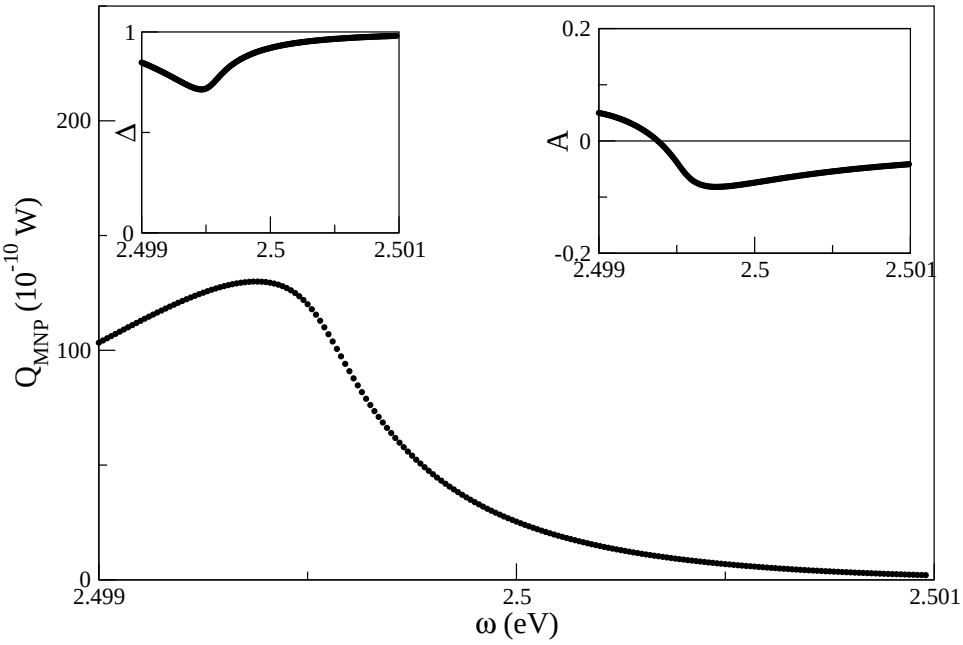

Figure 3.9: Region III. Power absorption density of the MNP with $R = 13\,\text{nm}$, $a = 7\,\text{nm}$, $\mu = 3\,\text{e nm}$ and the initial conditions $A(0) = 0$, $B(0) = 0$, $\Delta(0) = 1$. Left inset shows a population difference of about 0.8 at resonance and a very broad and suppressed response in the SQD that is shifted 0.5 meV from the bare resonance of the SQD. Right inset shows that the dipole moment of the SQD slowly changes sign at this shifted resonance.

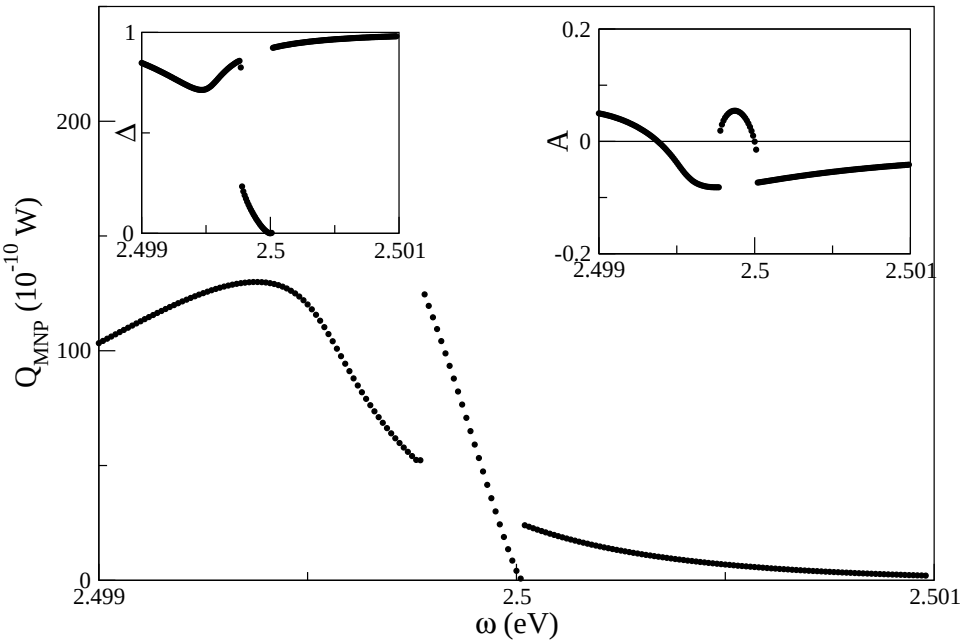

Figure 3.10: Region III. Power absorption density of the MNP with $R = 13\,\text{nm}$, $a = 7\,\text{nm}$, $\mu = 3\ \text{e}\,\text{nm}$ and the initial conditions $A(0) = 0$, $B(0) = 0$, $\Delta(0) = 0$. The bistability causes discontinuities in the responses of the MNP, the SQD and the population difference.

near the resonance frequency of the SQD, away from resonance all initial conditions lead to identical steady states. For $R = 13\,\text{nm}$, $a = 7\,\text{nm}$ and $\mu = 3.5\,\text{e}{\cdot}\text{nm}$ the width of bistability is $0.25\,\text{meV}$ for the mixed state initial conditions ($A(0) = 0$, $B(0) = 0$, $\Delta(0) = 0$) (see Figure 3.10). As the values of a and μ get closer to the transition region, this window in ω-space shrinks.

Outside the frequency window of this nonlinear behavior, the steady state equations, which are of third order in Δ, give one physical, real valued solution and two unphysical, complex valued solutions. Inside this window all three solutions are real and we must work with the full differential equations to explore the dynamics.

This region is defined by the relative strengths of G and Ω. If these two fields

are comparable, then $\frac{\Omega}{G} \approx 1$ implies that

$$\mu(a) = 2\pi\epsilon_0 E_0 \Big(\frac{\epsilon_{effM}\ \epsilon_{effS}}{s_\alpha^2 \gamma}\ \frac{R^6}{a^3} + \frac{\epsilon_{effS}}{s_\alpha}\ R^3 \Big). \tag{3.11}$$

Putting in typical values for ϵ_{effM}, ϵ_{effS} and γ and taking the magnitude of the first term, we get the following approximation

$$\mu(a) = 0.22\ \frac{E_0 R^6}{a^3} + 0.46\ E_0 R^3.$$

A fitting based on data taken from numerical simulations puts this line at

$$\mu(a) = 1.10\ \frac{E_0 R^6}{a^3} + 1.54\ E_0 R^3. \tag{3.12}$$

We see that bistability occurs once G becomes a significant factor when compared to Ω. When E_0 and R increase, this region shrinks and this bistable state eventually becomes physically inaccessible. It would appear that the easiest way to find this region of bistability is when E_0 becomes small in the weak field limit. However, in this limit, one finds that while most choices of a and μ lead to a bistability, the frequency width of the bistability is negligible making this feature experimentally unmeasurable. Thus this bistable state is only accessible in the regime that has been discussed here.

As we approach the boundary of Region III from the Suppression Region, the width of the second peak in the exciton induced transparency shaped response decreases, while the magnitude remains. At the boundary, this peak becomes pinched with negligible width for one of the steady state solutions resulting in the discontinuous jump evident in Figure 3.10. This transition is not smooth due to the nonlinear nature of region III.

3.6.0.1 Analysis of Initial Conditions

In the region of bistability (both in a vs. μ-space and in ω-space) there are three solutions. One of these three solutions, which we will call γ_1, is smooth and continuous as a function of ω and displays a very broad asymmetrical Fano shape (see Figure 3.9). In this steady state, the dot is in the ground state ($\rho_{11} = 1$) when away from resonance and only weakly excited near resonance. The second solution, similarly named γ_2, is the same broad asymmetrical Fano shape away from resonance with a discontinuous jump near resonance in the energy absorption spectrum(see Figure 3.10). In this steady state, the dot becomes strongly excited near resonance ($\rho_{11} \approx \rho_{22} \approx \frac{1}{2}$). The third solution, γ_3, turns out to be unstable (initial conditions arbitrarily close to this point evolve to a different steady state).

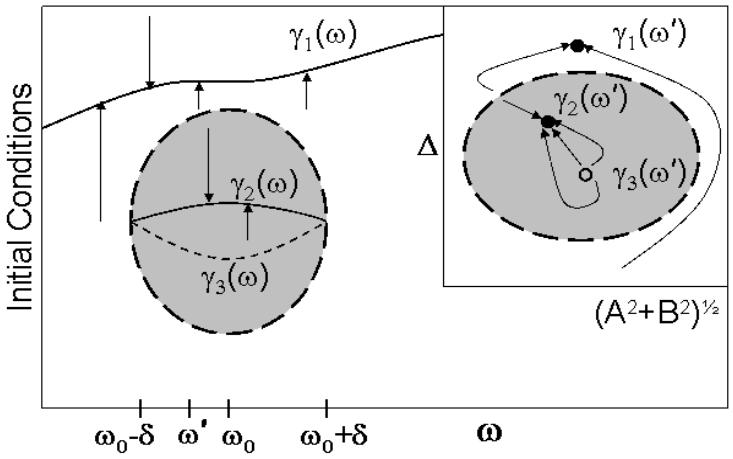

Figure 3.11: Schematic representation of initial conditions vs. frequency. γ_1 represents the continuous steady state, γ_2 represents the discontinuous steady state and γ_3 represents unstable steady state. Note that γ_2 and γ_3 only exist inside the frequency interval $(\omega_0 - \delta, \omega_0 + \delta)$. Arrows show how particular initial conditions evolve to one of the three solutions. Inset show a cross section in ω-space. Points arbitrarily close to γ_3 evolve to γ_2.

The space of initial conditions can be divided into 2 regions, one for each of the two possible, stable, steady-state solutions. For a particular choice of parameters ($R = 13\,\mathrm{nm}$, $a = 7\,\mathrm{nm}$, $\mu = 3.5\ \mathrm{e\,nm}$) the region with the discontinuous solution is an ellipsoid centered at $A(0) = 0$, $B(0) = 0$, $\Delta(0) = 0$ and is found through numerical calculations to be approximately given by the relation

$$4\Big(A(0)^2 + B(0)^2\Big) + \Delta(0)^2 \leqslant 0.07 \tag{3.13}$$

with the region outside this ellipsoid having the smooth solution. The unstable solution is a line through this space parameterized by ω in the interval $(\omega_0 - \delta,\, \omega + \delta)$. It can begin inside or outside of the region given by (3.13), but near resonance is always inside for cases we looked at (see Figure 3.11). For initial conditions exactly on this line, the state remains unchanged as it evolves in time. All other initial states evolve to γ_1 or γ_2.

As the initial conditions get close to the boundary of this region, the width ($\delta\omega = 2\delta$) shrinks. Numerically, the relationship between the initial conditions and this width was found to be approximately

$$\left[4\Big(A(0)^2 + B(0)^2\Big) + \Delta(0)^2\right]^2 + \left(\frac{\delta\omega}{4 \cdot 10^{-3} eV}\right)^2 = 0.005\ .$$

3.6.1 Calculation of the Resonance Shift

We saw in section 3.5 that as the coupling between the SQD and the MNP is increased and the transition is made into region III, there is a redshift in the resonance of the SQD. Accompanied with this redshift, there was a broadening of the response and a small population of the exciton excited state, i.e. Δ at resonance

is no longer nearly zero (see Figure 3.9 for an example of both of these effects).

We can model both the redshift and the new minimum of Δ. Starting with (3.7), we set the left hand side to zero to arrive at the steady state equations. Taking the first two equations and solving for A and B in terms of Δ we have

$$\begin{aligned} A &= -\Delta\Big(\frac{k\Omega_I + \delta\omega\Omega_R}{k^2+\delta\omega^2}\Big) \\ B &= -\Delta\Big(\frac{k\Omega_R - \delta\omega\Omega_I}{k^2+\delta\omega^2}\Big) \\ \Delta &= 1 + \tau_0\Big(4\Omega_I A + 4\Omega_R B + 4G_I(A^2+B^2)\Big) \end{aligned} \tag{3.14}$$

where we have defined

$$\begin{aligned} k &= \Delta G_I + \frac{1}{T_0} \\ \delta\omega &= \omega - \omega_0 + \Delta G_R \ . \end{aligned}$$

We now take the derivative with respect to ω for each of the equations in (3.14). To find the minimum of Δ, we evaluate them at the critical point $\omega = \omega_c$ and set $\Delta'(\omega_c) = 0$.

$$A' = \Delta\Big(\frac{2\delta\omega k\Omega_I - (k^2-\delta\omega^2)\Omega_R}{(k^2+\delta\omega^2)^2}\Big) \tag{3.15}$$

$$B' = \Delta\Big(\frac{2\delta\omega k\Omega_R + (k^2-\delta\omega^2)\Omega_I}{(k^2+\delta\omega^2)^2}\Big) \tag{3.16}$$

$$\Delta' = \tau_0\Big(4\Omega_I A' + 4\Omega_R B' + 8G_I(AA' + BB')\Big) \equiv 0 \tag{3.17}$$

Note that G and Ω are nearly constant over the range of frequencies that we consider because the plasmon peak is broad in comparison, thus we take their derivatives with respect to ω to be zero. Putting (3.15) and (3.16) into (3.17), and after a bit of algebra, we arrive at the result

$$0 = \Delta_c \ \delta\omega \ ,$$

where $\Delta_c \equiv \Delta(\omega_c)$. Δ_c cannot take a value of zero in the steady state, except in the limit that $\tau_0 \to \infty$ (this is easy to check), so we must have $\delta\omega = 0$. Using this result, we find that at $\omega = \omega_c$ we have $A = -\Delta_c \frac{\Omega_I}{k}$ and $B = -\Delta_c \frac{\Omega_R}{k}$. Then,

$$\Delta_c = 1 - 4\frac{\tau_0(\Omega_R^2 + \Omega_I^2)}{G_I}\Big(\frac{\Delta_c G_I}{k} - \frac{\Delta_c^2 G_I^2}{k^2}\Big) .$$

Note, that the only assumption we have made thus far is that the steady state exists. To proceed further, we now look at the region of parameter space where the resonance frequency shifts relative to the natural frequency ω_0. Since we are interested in the case in which a shift is seen in the resonance frequency (recalling that this coincides with Δ no longer being nearly zero), we take Δ_c to have a value greater than 0.01 and we have that $1/T_0\Delta_c G_I < 1$. Thus, we can expand k^{-1} and k^{-2}. In this case, we have

$$\Delta_c \approx 1 - 4\frac{\tau_0(\Omega_R^2 + \Omega_I^2)}{T_0 G_I^2 \Delta_c} .$$

Solving this quadratic equation for Δ_c and expanding the square root of the discriminant we have

$$\Delta_c \approx 1 - 4\frac{\tau_0(\Omega_R^2 + \Omega_I^2)}{T_0 G_I^2} + ... \tag{3.18}$$

So, our resonance occurs at

$$\omega_c = \omega_0 - G_R\Big(1 - 4\frac{\tau_0(\Omega_R^2 + \Omega_I^2)}{T_0 G_I^2}\Big) . \tag{3.19}$$

Using these approximations for Δ_c and ω_c, for typical parameters $\mu = 4\,\text{e·nm}$ and $a = 7$ nm, our approximations give $\Delta_c = 0.84$ and $\omega_c - \omega_0 = -0.82$ meV. Solving the differential equations numerically we find these two quantities to be

$\Delta_c = 0.81$ and $\omega_c - \omega_0 = -0.79$ meV, respectively, in excellent agreement with our approximations.

Looking at our expressions that describe the redshift and the minimum of Δ, we see that the turning on of these effects is controlled by the ratio $(\Omega_R^2 + \Omega_I^2)/G_I^2$. As we'll see in the next section, this ratio will largely determine the strength of the coupling to the imaginary component of the SQD dipole moment, B, with respect to the coupling to A. This increase in the coupling to the imaginary part of the SQD dipole moment (which has a damping effect on the system) causes the redshift in the SQD resonance and the decrease in the exciton population at resonance. In the next section, we'll see that this also causes the suppression to turn off.

3.7 Running (the) Interference: Phasors and Interaction Strengths

To better understand these interference effects, it is helpful to view the fields as phasors in the complex plane (see Figure 3.12). First consider a case of weak coupling (small μ). For weak coupling, Ω is much larger than G and we can ignore the effect of G (as was shown in Figure 3.7). Thus our resultant field on the SQD is mostly in the direction of Ω which is along the real axis both above and below resonance (see Figure 3.12). This has the effect of driving the SQD mostly by the real field, i.e. the SQD couples more strongly to A than to B.

However, when the coupling is increased so that G is no longer negligible, the field the SQD sees from the self coupling is $\rho_{12}G$. Below resonance, $\rho_{12}G$ is in phase with the applied field, but above resonance, it is out of phase with the

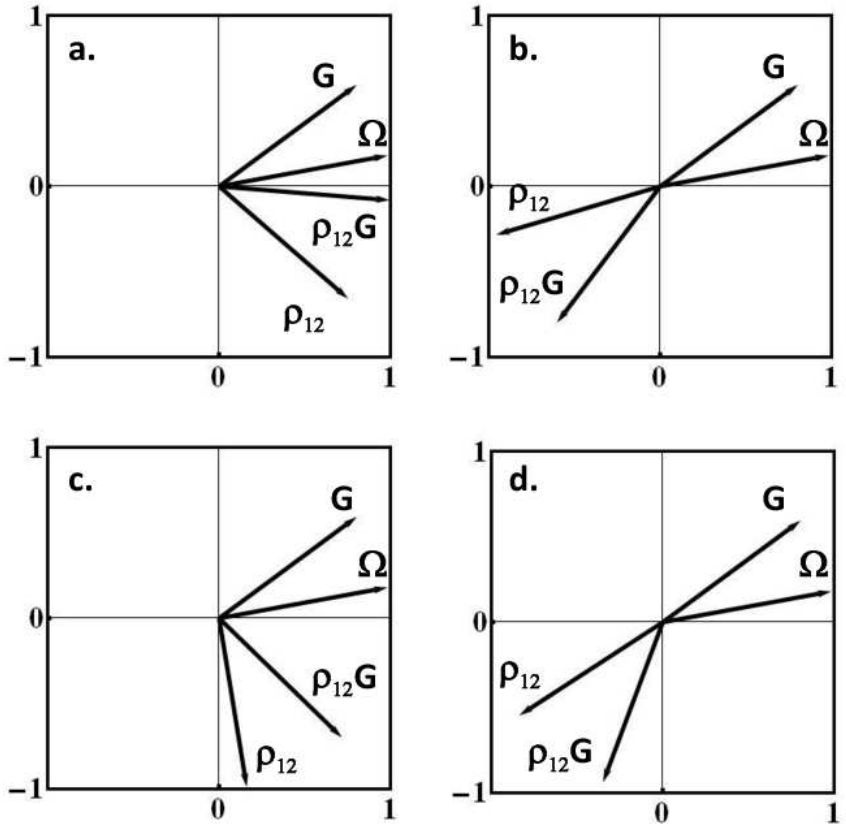

Figure 3.12: Depiction of phasors in the complex plane for $a = 7\,\text{nm}$. (a. and b.) $\mu = 2\,\text{e·nm}$. Suppression region. (a) below resonance ($\omega = 2.4999\,\text{eV}$) and (b) above resonance ($\omega = 2.5001\,\text{eV}$). (c. and d.) $\mu = 3\,\text{e·nm}$. Region III. (c) below resonance ($\omega = 2.4996\,\text{eV}$) and (d) above resonance ($\omega = 2.4999\,\text{eV}$) (note: resonance has shifted to $2.49975\,\text{eV}$ at this point). The phase of G and Ω are nearly constant. Moving left to right (i.e. below to above resonance), we see the real part of ρ_{12} changes sign. This is the phase shift associated with a damped, driven harmonic oscillator.

applied field. The SQD sees a weaker overall field above resonance than it does below resonance (where $\rho_{12}G$ and Ω remain relatively in phase) and thus the SQD response is suppressed above resonance.

Because G is more rotated in the complex plane than Ω, the introduction of G also has the effect of rotating the net electric field on the SQD toward the imaginary axis, 90° out of phase with the applied field. This allows a stronger coupling to B, the imaginary component of the SQD dipole. The increase in B, causes a further shift in $\rho_{12}G$ towards the negative imaginary axis. This, in effect, decreases the phase difference in the effective field above and below resonance, shutting off the suppression. Looking at Figure 3.12 and comparing the two diagrams on top, we see that the phase difference between $\rho_{12}G$ above and below resonance is $\approx 120°$. When the self coupling becomes stronger (bottom two diagrams), we see the phase angle between $\rho_{12}G$ above and below resonance is smaller ($\approx 60°$).

3.7.1 The Phase Change of ρ_{12}

When the coupling is strong enough to form a discontinuity in the response, the frequency at which ρ_{12} changes sign becomes dependent on the initial conditions of the system. For $a = 5.8\,\text{nm}$, $\mu = 4\,\text{e·nm}$ this shift in the crossing at $t = 10$ ns is approximately $0.2\,\text{meV}$ (see Figure 3.13).

To find the location of this phase shift, we begin with our steady state equa-

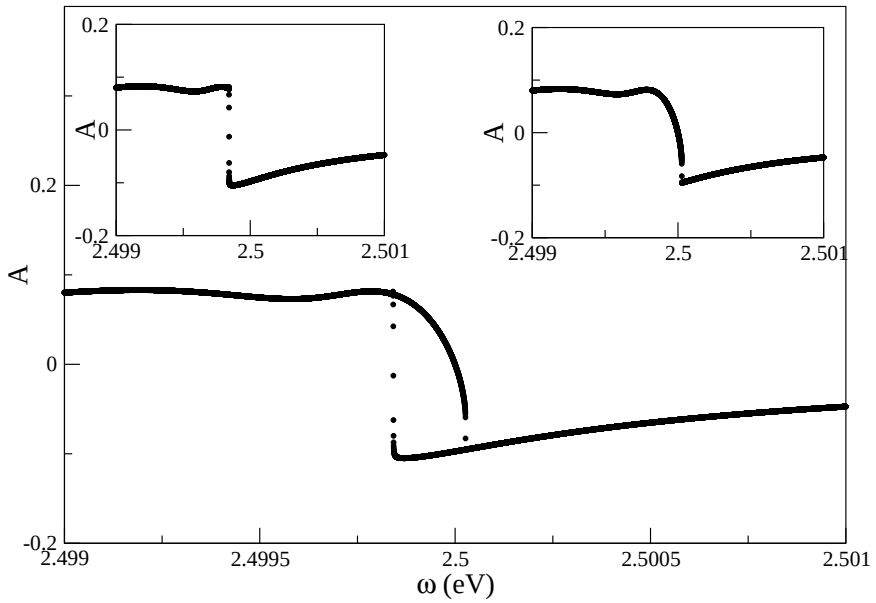

Figure 3.13: A, the real part of the SQD dipole moment for $\mu = 4\,\mathrm{e{\cdot}nm}$, $a = 5.8$ nm at $t = 10$ ns. Left insert: The system starts in the ground state. Right insert: The system starts in a mixed state, $\Delta = 0$. Center: an overlay of the two. The location of the phase crossing for the SQD dipole moment is dependent on the initial conditions.

tions (Eq. (3.14)). At the phase change, $A = 0$, and we have the system of equations

$$\begin{aligned} 0 &= B\Delta G_R + B(\omega - \omega_0) - \Delta\Omega_I \\ 0 &= -\Delta G_I B - \frac{B}{T_0} - \Delta\Omega_R \\ 0 &= 4G_I B^2 + 4\Omega_R B + \frac{1-\Delta}{\tau_0} \ . \end{aligned} \tag{3.20}$$

Solving the first for B, we have

$$B = \frac{\Delta\Omega_I}{\omega - \omega_0 + \Delta G_R} \ .$$

The solving the second for Δ, we have

$$\Delta = -\frac{\Omega_I + \Omega_R T_0(\omega - \omega_0)}{T_0(G_I\Omega_I + G_R\Omega_R)} \ .$$

Inserting these results in the third equation yields,

$$0 = \frac{4(G_I\Omega_I + G_R\Omega_R)(\Omega_I + \Omega_R T_0(\omega - \omega_0))}{(G_R + G_I T_0(\omega_0 - \omega))^2} + \frac{(G_I T_0 + 1)\Omega_I + T_0(G_R + \omega - \omega_0)\Omega_R}{T_0\tau_0(G_I\Omega_I + G_R\Omega_R)} \ . \tag{3.21}$$

This is a cubic equation in $\omega - \omega_0$. In general, for the steady state, we will have either 3 real solutions, or 1 real and 2 complex solutions. For example, we plot the roots of this equation for a fixed value of $\mu = 4\,\mathrm{e{\cdot}nm}$, letting a vary, in Figure 3.14. When $a > 6.3$ nm, we do in fact have 3 real solutions (see top of Figure 3.14). For $a < 6.3$ nm, the only real solution is $\omega - \omega_0 = 0$.

Looking again at Figure 3.13, it appears that for $\mu = 4\,\mathrm{e{\cdot}nm}$, $a = 5.8$ nm, there are in fact at least 2 distinct locations where A can change sign at $t = 10$ ns, even though only one crossing is predicted for steady state. When we take the calculation to larger times, we see that not only is there a slight shift in the location of the crossing for the mixed state initial condition, but that the the crossing becomes increasing sharp and in the steady state limit ($t \to \infty$) this crossing becomes a discontinuous jump (see bottom of Figure 3.14). There is a second location where A can undergo a sign change. However, at this second location, in the steady state, A is not equal to zero.

When all three solutions to equation (3.21) are real, working backwards, we see that we have then 3 real solutions of A, B, and Δ. This is exactly how we have defined region III previously, and we let this condition on the solutions to Equation (3.21) determine the boundary between the suppression regime and region III.

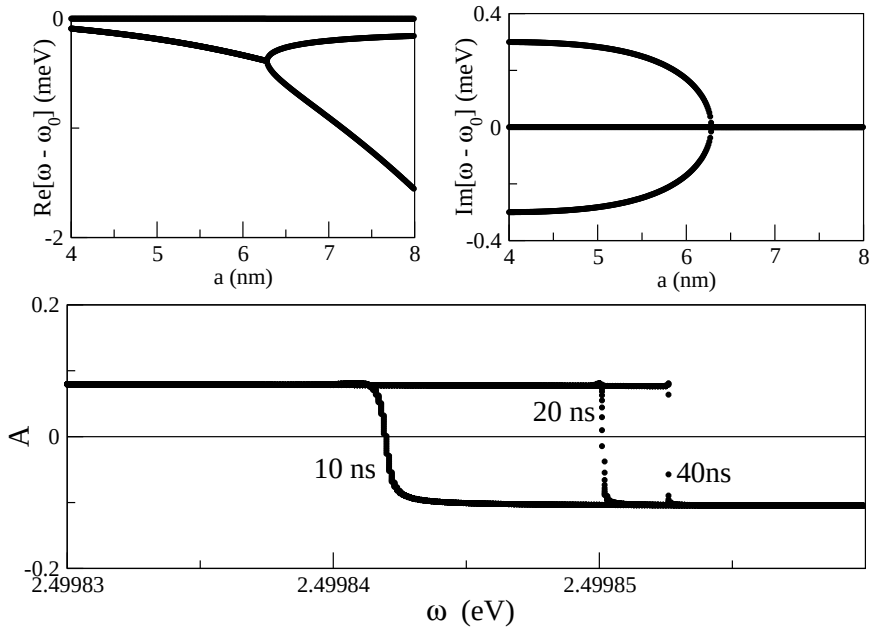

Figure 3.14: (Top) The real and imaginary parts respectively of solution to the cubic equation that determines the frequency at which A changes sign (plotted for $\mu = 4\,\mathrm{e{\cdot}nm}$). Up to $a = 6.3\,\mathrm{nm}$, there is one real solution and two complex solutions (which are conjugates of each other). In this region, the only real solution is $\omega - \omega_0 = 0$. For $a > 6.3\,\mathrm{nm}$, three real solutions exist. (Bottom) The real part of SQD dipole moment for $\mu = 4\,\mathrm{e{\cdot}nm}$, $a = 5.8\,\mathrm{nm}$, plotted for 10 ns, 20 ns and 40 ns evolutions respectively. We see that although for finite time, A has a continuous crossing through zero, as the system evolves to the steady state, the crossing becomes discontinuous.

3.8 The Effect of Polarization

So far, we have taken the applied field parallel to the major axis of the MNP-SQD molecule ($s_\alpha = 2$). There are two effects when the polarization is perpendicular to the main axis. First, the shape of the structures are reversed (see Figure 3.15). For parallel polarization with the induced dipoles of the SQD and MNP aligned end-to-end, the response is enhanced below resonance. For perpendicular polarization with

the induced dipoles aligned side-by-side, the response is enhanced above resonance. This accounts for the shape reversal.

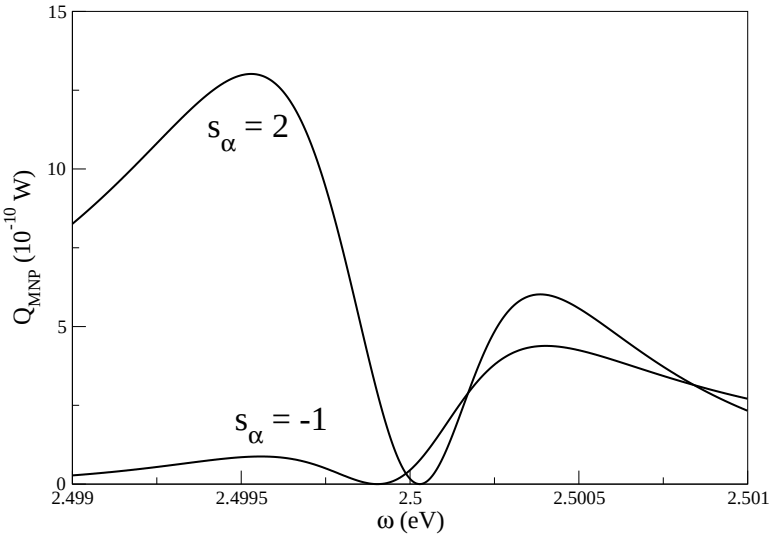

Figure 3.15: The effect of polarization on the response of the MNP in region II ($R = 13$ nm, $a = 3$ nm and $\mu = 3$ e nm). Curve labeled $s_\alpha = 2$ is for the applied field parallel to the main axis of the molecule, $s_\alpha = -1$ for perpendicular polarization. Both show an EXIT structure.

Second, is the shift upwards of the boundaries of regions I, II and III, as described by equations (3.10) and (3.11), by a factor of 2 to 4 (note in (3.10), A also reverses sign with s_α). The boundaries are defined by the relative magnitudes of the direct coupling, the induced field and the self-interaction. These relative magnitudes are different for the two polarizations. This results in the existence of points in parameter space that change from one region to another when the polarization is switched.

3.9 A Summary of Findings

To summarize, in this chapter we have investigated the optical response of a semiconductor quantum dot coupled with a metal nanoparticle. We have probed the strong applied electric field limit, where local induced fields are comparable to the driving field. We treated the SQD quantum mechanically in the density matrix formalism and the MNP as a classical spherical dielectric. We saw that the behavior of this system is highly dependent on the relative sizes of the MNP and SQD and by varying, μ and a, we found four distinct regimes of behavior in the strong field limit which each exhibit novel properties. By numerically probing parameter space we were able to set bounds on each of these regions. Furthermore, we were able to connect these numerical approximations of these boundaries to relationships amongst the various coupling strengths which allowed for a deeper understanding of how these behaviors emerge.

In the region of weak coupling, region I, we found that the energy absorption spectrum displays an asymmetrical Fano shape as previously predicted. It occurs when there is interference between the applied field and the internal field produced by the SQD at the location of the MNP. In the strong coupling regime, we saw that the behavior was more complex. As the SQD is increased in size (thus the coupling is increased), the asymmetrical Fano effect of region I is modified by the appearance of an additional peak with a deep minimum between the peaks. Here, the induced local field at the MNP becomes larger than the applied field, for frequencies near the SQD resonance. As such, the interference of the field from the SQD with the

applied electric field now results in a sign change in the net electric field at the MNP above resonance where the two fields are out-of-phase. An exciton induced transparency (EXIT) arises in the MNP response when there is nearly complete destructive interference between these two fields acting on the MNP.

A further increase in coupling strength moves the system into a transition regime, where the EXIT structure is modified with a discontinuous jump in response of the system (in both the diagonal and off-diagonal density matrix elements) and the response of the SQD is highly suppressed above resonance in this transition. This suppression comes about because the response of the SQD is that of a driven, damped harmonic oscillator. Specifically, this behavior is seen in the response of SQD dipole moment. As in the case of the classical damped driven oscillator, the behavior of the system is determined by the whether the driving frequency is above or below the resonance frequency of the system. Below resonance the dipole moment of the SQD is in phase with the driving field, and above resonance it is 180° out of phase. Since the phase of the self interaction of the SQD is determined by the phase of its own dipole moment, there is destructive interference above resonance and constructive interference below resonance, between the applied field and the self interaction field. EXIT is determined by the interference between the fields that drive the MNP. Suppression is determined by the interference among the fields that drive the SQD. In both cases, the phase of some of the fields changes at resonance, leading to a crossover from constructive to destructive interference. The fields that do change phase at resonance originate from the phase change in the SQD dipole moment that occurs at resonance.

As the coupling is further increased by increasing the sizes of both the SQD and MNP, the self-interaction of the SQD becomes significant in region III. Here, we found an extreme broadening of the response that washes out the second peak of the EXIT. More interestingly, we found that the response is nonlinear. This nonlinearity is due to the significant self interaction of the SQD (feedback through the MNP). In this regime, we found the existence of multiple steady state solutions leading to a bistability where one of the two stable solutions has a discontinuous energy spectrum. Furthermore, we saw that coupling to the imaginary part of the SQD dipole moment largely determines whether EXIT, suppression or bistability in the system is visible.

We have predicted phenomena that could emerge from an SQD-MNP hybrid molecule, and just as importantly, we have located in parameter space where these phenomena occur, and what causes them to emerge. How the various system fields interfere, constructively and destructively, is central in determining system response. This understanding is critical if one is to know how to generalize these results to similar system and more complicated structures. In the next chapter we will see how this knowledge could be exploited in order to engineer MNP-SQD systems that are tailored towards a desired system behavior. In particular, we will show how to engineer hybrid systems that will best display this behavior.

Chapter 4

Engineered SQD-MNP Systems with Extended Geometries

So far we have studied the interactions between an SQD and a spherical MNP, using the dipole approximation for the field emitted from the MNP. The geometry of these hybrid systems determines the nature of the local fields and couplings, which in turn determines the system behavior. Useful devices that will utilize these structures will require more complicated geometries than what we have previously explored. To consider more complex MNP structures, for example, nanorods and nanowires, chains of MNPs, and SQDs at various positions in the structure, a more complete calculational method for the local fields needs to be employed than was used in the previous chapter (i.e. using a non-retarded, dipole approximation for the MNP response). In this chapter we will utilize the boundary element method (BEM) to fully account for the response electric fields of such complex structures.

4.1 Introduction

There are two basic interactions that the SQD participates in. One is the coupling due to an applied plane wave driving field (both directly with the driving field and from the response of the MNP to the applied plane wave). The second is the self-interaction of the SQD in which the MNP responds to the polarization field of the SQD and in turn produces a field felt back at the SQD. As we saw in

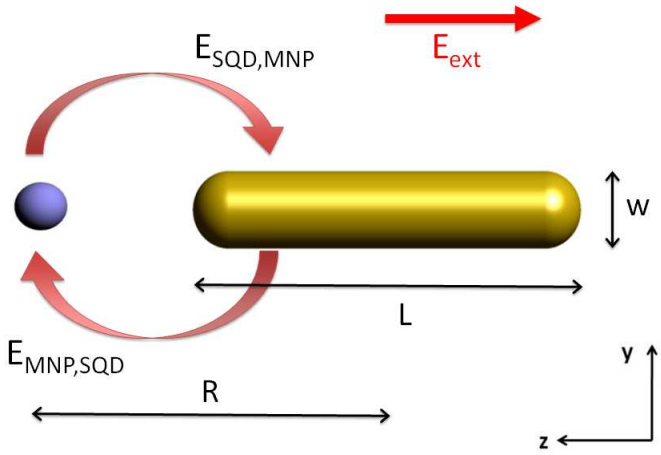

Figure 4.1: An applied field polarizes both the MNP and SQD which in turn allows them to couple.

the previous chapter, the behavior of the system is determined by the ratio of these two couplings. This provides an avenue that can be exploited to engineer systems (by tuning both the coupling strengths and geometry) to bias the response towards a particular regime of behavior or to enhance the behavior, as we will discuss here.

In chapter 3, these two coupling strengths were varied by changing the radius of the MNP as well as the dipole moment of the SQD. However, in practical situations the SQD dipole moment would be difficult to control. To reach the strongest coupling regimes discussed in chapter 3, large and perhaps unreasonable values of the SQD dipole moment were needed. By utilizing structures with a more complex geometry we will see how even small values of the SQD dipole moment can be used to reach the strongest coupling regimes. This will allow us to tailor the response of the system by engineering metal nanoparticle shape and the exciton resonance of an

SQD in order to control the individual local near-fields that couple the MNP and the SQD.

The effect of MNP size, shape and SQD placement will be analyzed to determine the regimes where the local multipolar response becomes significant. We will identify regimes where dark modes and higher order multipolar modes can influence the hybrid response. External fields do not directly drive MNP dark modes, so SQD/MNP coupling is dominated by the local induced coupling, providing a situation in which the induced self-interaction could be probed using near field techniques. All of these aspects could enhance the capabilities of metal nanostructures to provide spatial and spectral control of the optical properties of single emitters.

In section 2 we discuss the hybrid molecule in detail, allowing for a more complex structure. The MNP is taken as a classical dielectric with a response calculated with the BEM. Upon finding the resultant fields acting on the SQD, we use a density matrix approach to treat the SQD. Once the behavior of the SQD is found, we then use that information to calculate the local near fields of our hybrid molecule. We also calculate the energy absorption of the MNP and provide details on how numerical calculations were carried out. In section 3 we discuss the conditions when a full electrodynamical calculation should be used for a spherical MNP rather than a multipole expansion or dipole approximation. We also apply the BEM to study the response of a nanorod. In section 4 we discuss how coupling the SQD to a nanorod allows the system to be engineered toward a particular regime of behavior. Here we exploit coupling to the dark states of the nanorod to investigate the self-interaction of the SQD. We present our conclusions in section 5.

4.2 Setup

We consider hybrid molecules consisting of a spherical SQD, radius r, interacting with a MNP structure which has cylindrical symmetry about the axis joining the SQD and the MNP structure. The MNP structure could be a nanorod or a nanosphere, or a linear chain of those. In this chapter we will consider the MNP to be a nanorod, constructed with a cylinder making up the length of the MNP, capped with hemispherical ends, with a total length L and width w (see figure 4.1. As before, the SQD and MNP are separated by a distance R and entire system is subject to an applied electric field $E = E_0 \cos(\omega t)$. We treat the SQD quantum mechanically in the density matrix formalism with exciton energy $\hbar\omega_0$, dipole moment μ and dielectric constant ϵ_S. In the dipole limit only the three bright excitons (one for each optical axis) participate in the interaction. By choosing the direction of the applied field to be either perpendicular or parallel to the axis of our system, we again only excite one of the three excitons.

The optical response of the MNP is calculated by means of the boundary element method in a full electromagnetic calculation, including retardation. Retardation must be included because we consider structures with lengths that can be comparable to the wavelength of incident light. In the BEM, Maxwells equations for inhomogeneous media with sharp boundaries between regions with different dielectric constants are solved in terms of charges and currents distributed on the surfaces and interfaces. Boundary conditions are imposed via surface integrals along the boundaries between different media. Each region is characterized by a local

dielectric function. The external fields interact self-consistently with the induced boundary charges and currents, which are determined by discretizing the surface integrals and solving the appropriate matrix equations. In this approach, the scattered field due to an incident external field is calculated directly. We calculate, in this way, both the near and far fields for a given MNP from both a plane wave source as well as from a dipole source (the SQD). In handling the dipole source, we take a quasi-static approach and do not include the time dependence of the dipole moment in Maxwell's equations.

As before, our Hamiltonian for the two level SQD, $\mathcal{H}_{SQD}$, is

$$\mathcal{H}_{SQD} = \hbar\omega_0 \hat{a}^\dagger \hat{a} - \mu E_{SQD} \left(\hat{a} + \hat{a}^\dagger\right), \tag{4.1}$$

where $\hat{a}$ and $\hat{a}^\dagger$ are the exciton annihilation and creation operators. E_{SQD} is the total electric field felt by the SQD and consists of the applied, external field, E, and the induced, internal field, produced by the polarization of the MNP. The MNP is polarized by the applied plane wave and we denote the response field as $E_{planewave}$. The MNP is also polarized by the dipole field produced by the SQD and this response field we denote E_{dipole}. Taking into account screening, we can then write E_{SQD} as

$$E_{SQD} = \frac{1}{\epsilon_{\text{effS}}} \left(E + E_{planewave} + E_{dipole}\right), \tag{4.2}$$

where $\epsilon_{\text{effS}} = \frac{2\epsilon_B + \epsilon_S}{3\epsilon_B}$. ϵ_B is a background dielectric constant which would correspond to the medium in which the system is embedded. Writing the applied field as $E = E_0 \cos(\omega t) = \frac{E_0}{2} e^{-i\omega t} + \frac{E_0}{2} e^{i\omega t}$ and the response from the MNP due to a unit plane wave with positive frequency as E_p (which will be calculated using BEM),

then

$$E_{planewave} = \frac{E_0}{2} E_p \, e^{-i\omega t} + \frac{E_0}{2} E_p^* \, e^{i\omega t}.$$

We make use of the density matrix ρ to calculate the polarization of the SQD. We label the ground state of our SQD (no exciton) as level 1 and the excited state (one exciton) we label as level 2. We then have for the polarization, $P_{SQD} = \mu(\rho_{12} + \rho_{21})$ (see [48]). Factoring out the high frequency time dependence of the off-diagonal terms of the density matrix, we define

$$\begin{aligned} \rho_{12} &= \widetilde{\rho}_{12} \, e^{i\omega t} \\ \rho_{21} &= \widetilde{\rho}_{21} \, e^{-i\omega t} \, . \end{aligned} \tag{4.3}$$

We write the response of the MNP due to a dipole source with positive frequency at the location of the SQD as E_d (again calculated with BEM and evaluated at the location of the SQD). Taking into account the screening at the dipole, we then have,

$$E_{dipole} = \frac{\mu}{\epsilon_{\text{effS}}} \widetilde{\rho}_{21} E_d \, e^{-i\omega t} + \frac{\mu}{\epsilon_{\text{effS}}} \widetilde{\rho}_{12} E_d^* \, e^{i\omega t}.$$

Putting these expressions for $E_{planewave}$ and E_{dipole} into equation (4.2), as well as writing out the applied field explicitly, we have

$$E_{SQD} = \frac{1}{\epsilon_{\text{effS}}} \Big(\frac{E_0}{2}(1 + E_p) + \frac{\mu}{\epsilon_{\text{effS}}} \widetilde{\rho}_{21} E_d \Big) \, e^{-i\omega t} + h.c., \tag{4.4}$$

In order to write this in a more familiar form, we make the following definitions

$$\begin{aligned} G &= \frac{\mu^2}{\hbar \epsilon_{\text{effS}}^2} E_d \\ \Omega &= \frac{\mu E_0}{2\hbar \epsilon_{\text{effS}}} (1 + E_p), \end{aligned}$$

in terms of the responses, E_p and E_d, to a unit plane wave and unit dipole, respectively. Once we know E_p and E_d, the theory proceeds as it did in chapter 3. Again we can identify G as the self-interaction of the SQD, the first term in Ω as the direct coupling to the applied field and the second term in Ω as arising from the MNP response to the applied field. We again write the field acting on the SQD as,

$$E_{SQD} = \frac{\hbar}{\mu}\Big\{(\Omega + G\,\widetilde{\rho}_{21})\,e^{-i\omega t} + (\Omega^* + G^*\,\widetilde{\rho}_{12})\,e^{i\omega t}\Big\}. \tag{4.5}$$

We solve the master equation

$$\dot{\rho} = \frac{i}{\hbar}[\rho, \mathcal{H}_{SQD}] - \Gamma(\rho)\,, \tag{4.6}$$

where $\Gamma(\rho)$ is the relaxation matrix with entries $\Gamma_{11} = \frac{\rho_{11}-1}{\tau_0}$, $\Gamma_{12} = \Gamma_{21}^* = \frac{\rho_{12}}{T_{20}}$ and $\Gamma_{22} = \frac{\rho_{22}}{\tau_0}$. Again we separate real and imaginary parts, and write the density matrix elements as

$$\widetilde{\rho}_{12} = A + iB$$

$$\widetilde{\rho}_{21} = A - iB$$

$$\Delta = \rho_{11} - \rho_{22}\,.$$

To solve (4.6), we make the rotating wave approximation. When changing the Hamiltonian to the interaction picture we keep terms that oscillate like $e^{i(\omega-\omega_0)t}$ and neglect terms that oscillate like $e^{i(\omega+\omega_0)t}$. Making use of our definitions and the rotating wave approximation, we have the same set of coupled differential equations,

$$\begin{aligned}
\dot{A} &= -\frac{A}{T_{20}} + (\omega-\omega_0)B - \Big(\Omega_I + G_I A - G_R B\Big)\Delta \\
\dot{B} &= -\frac{B}{T_{20}} - (\omega-\omega_0)A - \Big(\Omega_R + G_R A + G_I B\Big)\Delta \\
\dot{\Delta} &= \frac{1-\Delta}{\tau_0} + 4\Omega_I A + 4\Omega_R B + 4G_I(A^2+B^2),
\end{aligned} \tag{4.7}$$

where G_R, G_I, Ω_R and Ω_I are the real and imaginary parts of G and Ω respectively. We solve this set of differential equations as we did previously in chapter 3.

4.2.1 System Energy

As before, the rate at which energy is absorbed by our system consists of two parts, Q_{SQD} and Q_{MNP}. The SQD absorbs energy by the creation of an exciton followed by a non-radiative decay. The rate is just $Q_{SQD} = \hbar\omega_0\rho_{22}/\tau_0$. To calculate the energy absorbed by the MNP, we take the time average of the volume integral, $\int \mathbf{j}\cdot\mathbf{E}\, dv.$, where $\mathbf{j}$ is the local current density. To calculate the fields inside the MNP we again employ the BEM. We denote the field inside the MNP due to the dipole field of the SQD as $E^{(inside)}_{dipole}$. This field includes the field due to the polarization induced in the MNP as well as the dipole field of the SQD. Similarly, we denote the field inside the MNP due to the applied plane wave as $E^{(inside)}_{planewave}$ and this field includes the field due to the polarization induced in the MNP as well as the applied field. These fields with positive frequency can be determined once E^i_d (the field inside the MNP due to a unit dipole with positive frequency at the SQD) and E^i_p (the field inside the MNP due to a unit incident plane wave with positive frequency) are known. We write

$$E^{(inside)}_{dipole} = \frac{\mu}{\epsilon_{\text{effS}}}\widetilde{\rho}_{21}E^i_d\, e^{-i\omega t} + \frac{\mu}{\epsilon_{\text{effS}}}\widetilde{\rho}_{12}(E^i_d)^*\, e^{i\omega t}$$

$$E^{(inside)}_{planewave} = \frac{E_0}{2}E^i_p\, e^{-i\omega t} + \frac{E_0}{2}(E^i_p)^*\, e^{i\omega t}\,,$$

in a notation similar to what we have previously employed. Thus the field inside the MNP is just the sum of these two fields. We calculate the current density, j as

we did in chapter 3, $j = -\epsilon_m(\omega)\frac{\partial E}{\partial t}$ and again take the time derivatives of $\widetilde{\rho}_{12}$ and $\widetilde{\rho}_{21}$ to be zero and we then have for the local current, j,

$$j = i\omega\Big\{\epsilon_m(\omega)\Big(\frac{E_0}{2}E_p^i + \frac{\mu}{\epsilon_{\text{effS}}}\widetilde{\rho}_{21}E_d^i\Big)e^{-i\omega t} - \epsilon_m(\omega)^*\Big(\frac{E_0}{2}(E_p^i)^* + \frac{\mu}{\epsilon_{\text{effS}}}\widetilde{\rho}_{12}(E_d^i)^*\Big)e^{i\omega t}\Big\}.$$

We can now calculate $\mathbf{j}\cdot\mathbf{E}$,

$$\begin{aligned}\mathbf{j}\cdot\mathbf{E} =& i\omega\Big\{\epsilon_m(\omega)\Big(\frac{E_0}{2}E_p^i + \frac{\mu}{\epsilon_{\text{effS}}}\widetilde{\rho}_{21}E_d^i\Big)^2 e^{-2i\omega t} \\ &+ \epsilon_m(\omega)^*\Big(\frac{E_0}{2}(E_p^i)^* + \frac{\mu}{\epsilon_{\text{effS}}}\widetilde{\rho}_{12}(E_d^i)^*\Big)^2 e^{2i\omega t} \\ &+ 2i\text{Im}[\epsilon_m(\omega)]\Big|\frac{E_0}{2}(E_p^i) + \frac{\mu}{\epsilon_{\text{effS}}}\,\widetilde{\rho}_{12}\,(E_d^i)\Big|^2\Big\}.\end{aligned}$$

Taking the time average of this result over the period of fast oscillation and integrating over the volume of the MNP yields Q_{MNP},

$$Q_{MNP} = 2\omega\text{Im}[\epsilon_m(\omega)^*]\int\Big|\frac{E_0}{2}(E_p^i) + \frac{\mu}{\epsilon_{\text{effS}}}\widetilde{\rho}_{21}(E_d^i)\Big|^2 dv.$$

We calculate this integral numerically using the BEM to find (E_p^i) and (E_d^i) and equation (4.7) to find $\widetilde{\rho}_{21}$ in the steady state limit.

4.2.2 Numerical Calculations in the Large Field Limit

In this paper we take our MNP to have cylindrical symmetry about the z-axis and we take the dielectric constant of the background to be $\epsilon_B = \epsilon_0$. We model the MNP as a cylinder with hemispherical ends, with total length L and total width w (see Figure 4.1). Thus, in the case of $L = w$, we have a sphere of radius $w/2$. The SQD is placed on the positive z-axis a distance R from the center of the MNP. We

consider the large field limit (intensity of $10^3\,\mathrm{W/cm^2}$) and we take the polarization of the applied electric field parallel to the axis of our SQD-MNP molecule (the $\hat{z}$ direction) with the propagation along the $\hat{x}$ direction. We take $\epsilon_m(\omega)$ as the bulk dielectric constant of gold as found experimentally [55]. For the SQD, we take $\epsilon_S = 6\,\epsilon_0$ and the exciton resonant frequency to be in the range of $1 - 4\,\mathrm{eV}$. For the relaxation times of the SQD we take $\tau_0 = 0.8\,\mathrm{ns}$ and $T_{20} = 0.3\,\mathrm{ns}$.

4.3 Advantages of Using a Full Electrodynamical Description

Previously, calculations have been done on a system consisting of an SQD interacting with a spherical MNP in the dipole limit[20, 21, 22] as well as in the multipole limit[23], both of which are a non-retarded approach. In the dipole limit, the ratio of MNP radius, a, to MNP-SQD separation, R, should be small (as the multipole expansion is a power series in $(\frac{a}{R})^2$). For $a = 7\,\mathrm{nm}$, $R = 13\,\mathrm{nm}$, the first order correction is nearly 30%.

In [23] it was shown that for $a = 15\,\mathrm{nm}$, $R = 20\,\mathrm{nm}$, the sum of the first 10 terms of the multipole expansion of the coupling strength between the MNP and SQD is almost 7 times greater than that given by only the first term in the series (the dipole limit). The most interesting hybrid molecules are those with strong coupling. One manner of increasing the coupling strength between the MNP and SQD is to place the SQD very close to the MNP, thus, the correction due to higher order multipole terms will be important in the systems we most wish to study.

4.3.1 Comparison Between a Full Electrodynamical Calculation and a Non-Retarded Multipole Expansion for Spherical MNPs

In order to compare the results obtained using the BEM with those given by the quasi-static multipole expansion, we compare the values of G given by the two methods, because there is no multipolar correction to the response due to the applied plane wave. In the multipole limit, G is given by the expression (see ref. [23])

$$G = \sum_{n=1}^{\infty} \frac{s_n \gamma_n a^{2n+1} \mu^2}{4\pi\epsilon_B \, \hbar \, \epsilon_{\text{effS}}^2 \, R^{2n+4}} \,, \tag{4.8}$$

where

$$\gamma_n = \frac{\epsilon_m(\omega) - \epsilon_B}{\epsilon_m(\omega) + \frac{n+1}{n}\epsilon_B},$$

and $s_n = (n+1)^2$ or $P_n'(1)$ for polarization parallel or perpendicular to the z-axis and P_n' is the first derivative of the Legendre function. When we take only the term with $n = 1$, we recover the dipole approximation. In order to calculate the fields in the multipole expansion for systems where the total separation is very nearly equal to the radius of the MNP ($R \approx a$), many terms are needed for convergence of (4.8).

For a spherical MNP with $R = 60\,\text{nm}$ and $a = 40\,\text{nm}$, we see an enhancement in the imaginary part of G of nearly a factor of two. We also see a slight enhancement of $\approx 25\%$ and a red shift on the order of $0.1\,\text{eV}$ in the peak of the real part of G (see figure 4.2). When this calculation is carried out over a large subset of MNP sizes and separation, this enhancement increases as the MNP radius is increased for fixed separation up to a MNP radius of approximately $50\,\text{nm}$ (except in the most extreme cases of very small separation) or if the separation is increased for fixed

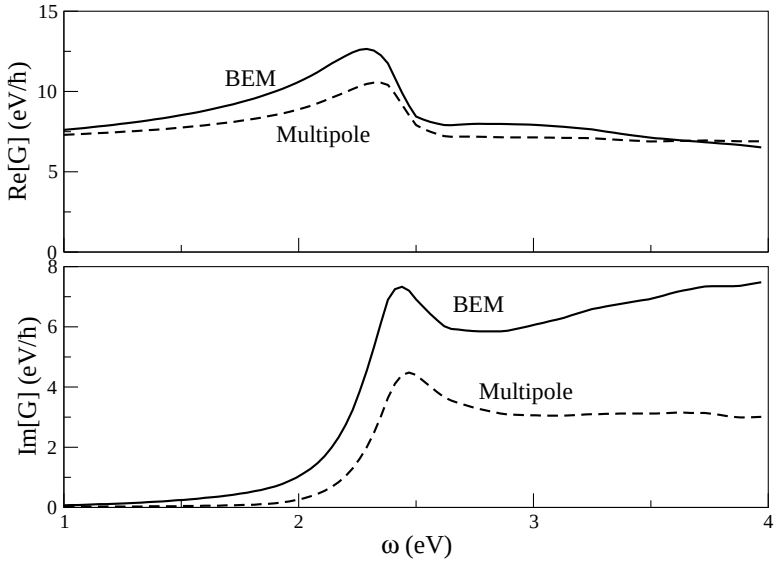

Figure 4.2: The real and imaginary parts of G with $R = 60\,\text{nm}$ and $a = 40\,\text{nm}$, shown for both a full electrodynamical calculation using the boundary element method (labeled as BEM) and a non-retarded multipole expansion (labeled Multipole). In this case we see an enhancement in the imaginary part of G, and a slight enhancement and red shift of the peak in the real part of G.

MNP radius (see figure 4.3). However, as the separation between the SQD and the surface of MNP becomes small ($R \approx a$), the calculations from the boundary element method and the multipole expansion yield the same results. However, note that in these extreme cases, as many as 500 terms of the expansion are needed for the sum to converge.

To understand these results, it is beneficial to think in terms of the image charges induced in the MNP by the SQD rather than the self-interaction. The image charges induced in the MNP should arise from the polarization of the dipole mode of the MNP, with image charges at both ends of the MNP, one nearest to the SQD and one at the furthest point. In the retarded limit, these two image charges can be out of phase with each other owing to their spatial separation. For very

small surface to surface separation, the SQD is very near to the closer image charge, with much stronger coupling to that image charge, and much weaker coupling to the charge at the other end. In this case, any phase difference is unimportant and the retarded and non-retarded limits are the same, as seen on the near edge of figure 4.3. However, as the SQD and MNP are separated, the effect of the image charge on the backside of the MNP also becomes significant, screening the effect of the image charge nearest to the SQD. In the retarded limit, when there is a phase difference between these two image charges, the screening is less effective and thus a full electrodynamical calculation yields a larger value of the field than the non-retarded limit.

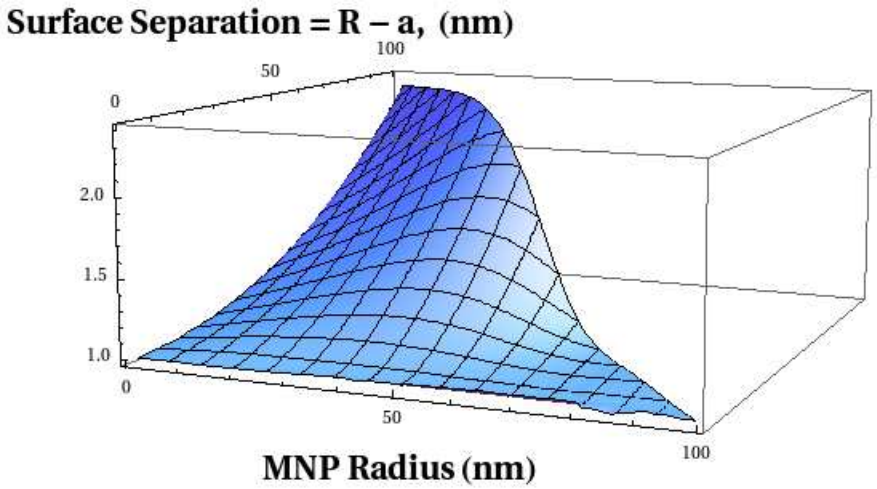

Figure 4.3: Ratio of the magnitude of G as calculated with a full electrodynamical calculation using the BEM to that of the multipole expansion at a frequency of 2.5 eV which is near the plasmon resonance for an Au sphere. The value given by the BEM increases in relation to that of the multipole as the MNP radius is increased for fixed separation up to a MNP radius of approximately 50 nm (except in the most extreme cases of very small separation) or if the separation is increased for fixed MNP radius.

4.3.2 From Spheres to Rods

For most systems of interest involving a spherical MNP and a SQD (i.e. for small separation), both the multipole method and the BEM will yield similar results. The main advantage of using the BEM is that we can study any shape of MNP we choose. Also, one can study the effects of placing the SQD off the symmetry axis. Moreover, the multipole expansion only has a simple form in the cases that the applied field is perpendicular or parallel to the molecular axis.

When we replace the spherical MNP with a nanorod the effect on coupling can be quite dramatic (see Figure 4.4). Holding the width of the nanorod fixed at 14 nm, as we move from a wire of length 14 nm (which is a 7 nm radius sphere) to a wire of length 150 nm, we see an enhancement in the value of Ω_R of approximately an order of magnitude, and of Ω_I of nearly 25 times at the peak value (see figure 4.4). Whereas the peak values of G remain relatively unchanged, we do see higher order modes appear in the spectrum. At $L = 150$ nm a total of 3 peaks have appeared in G (at 1.1, 1.7 and 2.1 eV) whereas there are only 2 in Ω (at 1.1 and 2.1 eV). We also note a redshift in the principle plasmon peak for both G and Ω.

As we saw last chapter, the ratios of the various components of G and Ω are key in determining the behavior of the SQD-MNP molecule. The more complicated spectrum provided by a wire, yields a much broader range of system behavior. The enhancement provided by a wire also allows for the regimes of strongest coupling to be more easily accessed experimentally.

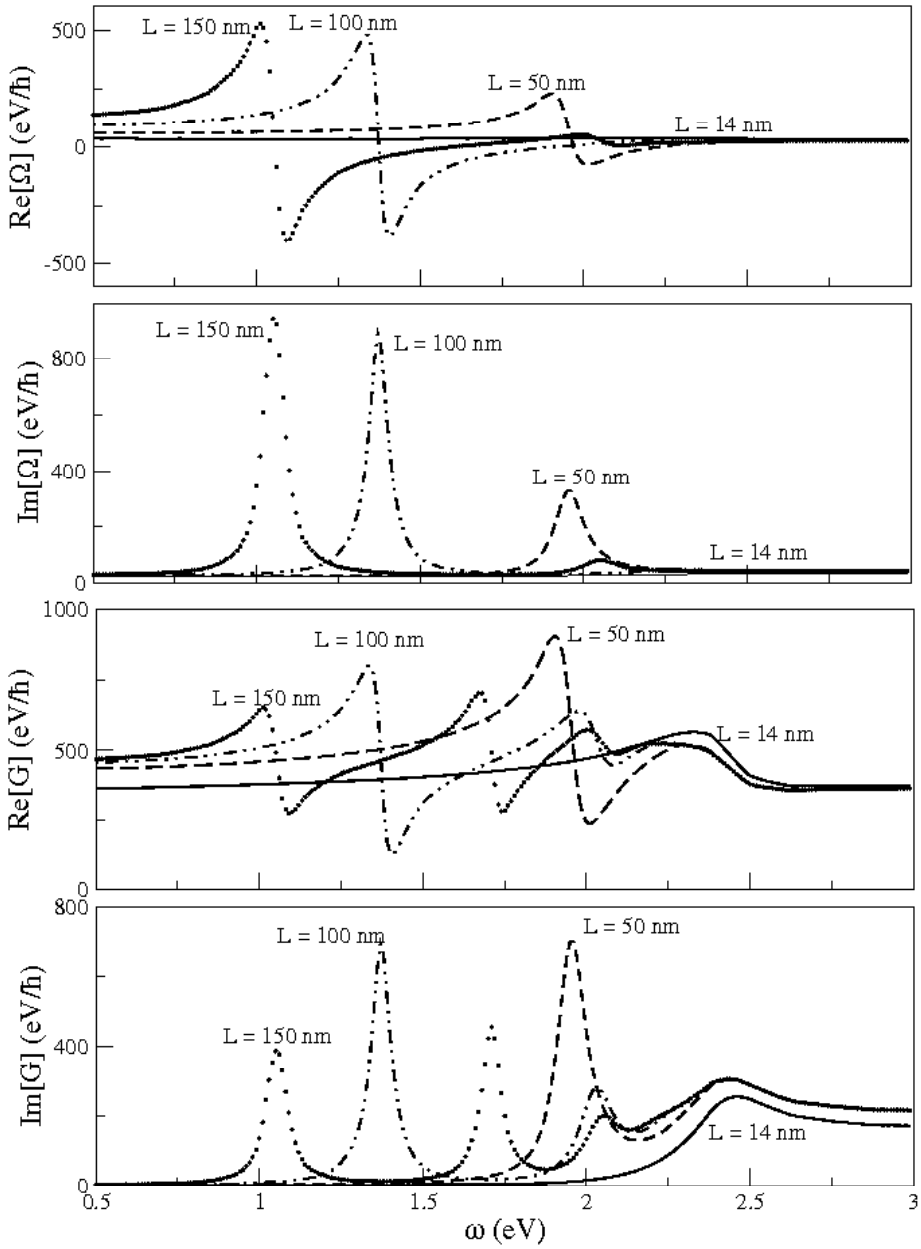

Figure 4.4: The real and imaginary components of G and Ω for various values of the wire length. The width of the wire was fixed at 14 nm, thus the $L = 14$ nm setup is that of a 7 nm radius sphere. Ω shows a redshift as well as an enhancement in the response as the length is increased. G shows a redshift as well as the appearance of higher order modes. For $L = 150$ nm, Ω has 2 peaks, one at 1.1 eV and one close to 2.1 eV. However, in addition to those 2 peaks, G shows an additional peak around 1.7 eV for $L = 150$ nm.

4.3.2.1 Coupling to Dark States vs. Bright States

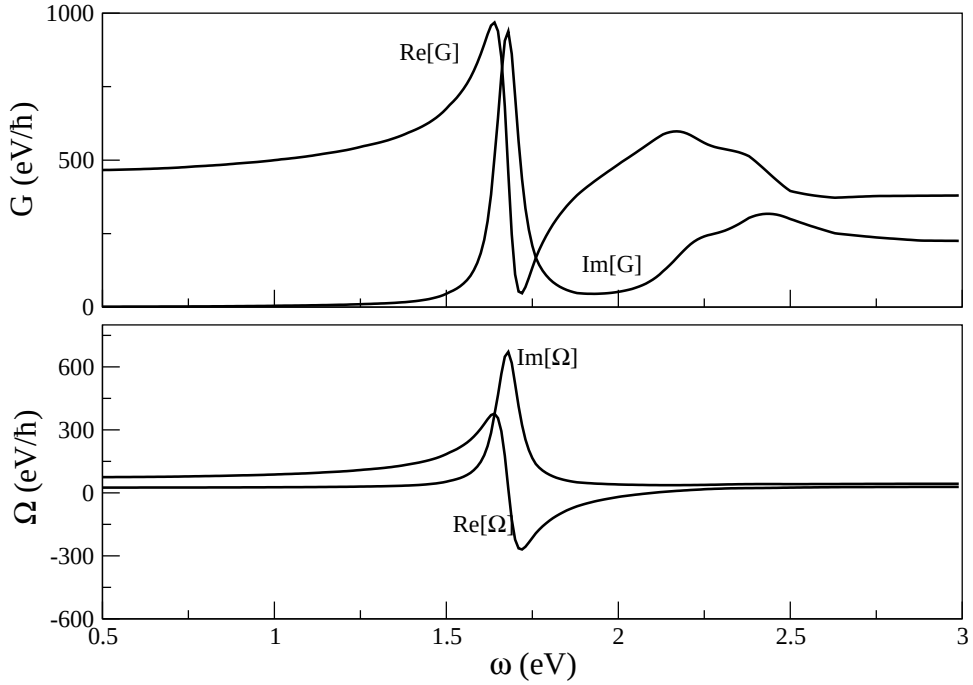

Figure 4.5: Response of a 70 nm wire. Both G and Ω are peaked near 1.6 eV. However, we also see a strong response in G between $2 - 2.5$ eV, whereas there is no appreciable response in Ω over that range of frequencies. The peak near 2.2 eV in the real part of G is evidently a "dark" mode.

As we increase the length of the nanorod, higher order modes appear in the response. Even order dipole-forbidden modes do not appear in the response to a plane wave source (Ω), due to symmetry considerations, but they do appear in the response to a dipole source (G). Such states are called dark states.

For a 70 nm wire, we see that both G and Ω are peaked around 1.6 eV. However, we also see a strong response in G between 2 and 2.5 eV, whereas there is no appreciable response in Ω over that range of frequencies (see Figure 4.5). Thus at this frequency, the MNP is not polarized by the applied field, so the only coupling

between the SQD and the MNP is via the self-interaction (G). Coupling to these dark states will then allow us to study more closely the self-interaction of the SQD (which is controlled by G).

To better illustrate what occurs here, we next consider the near field response (magnitude of the time average of the electric field squared) of the nanorod to a plane wave and dipole source respectively. We place the dipole source 5 nm above the tip of the wire with a dipole moment of 1 e nm. The coupling to a plane wave source in this situation can be a full order of magnitude smaller for a dark state compared to that of a bright state (see figure 4.6). Whereas the bright state has regions of large electric field in the vicinity of each end of the wire (over 20 times that of the applied field), the dark state only has a slight increase in field strength near the wire (about twice that of the applied field). However, the response to the dipole only shows a drop of approximately a factor of 2, when comparing the response in the bright state to that of the dark.

4.4 Engineered Systems

Once the values of G and Ω are obtained, the differential equations for the SQD evolution (equation 4.7) can be solved either dynamically, or in the steady state limit. Once the density matrix is obtained, those results can then be used to calculate the SQD polarization, and from that the total electric field at any location in space, for any particular value of the applied plane wave frequency. Furthermore, these local fields can be calculated at any instance of the system evolution.

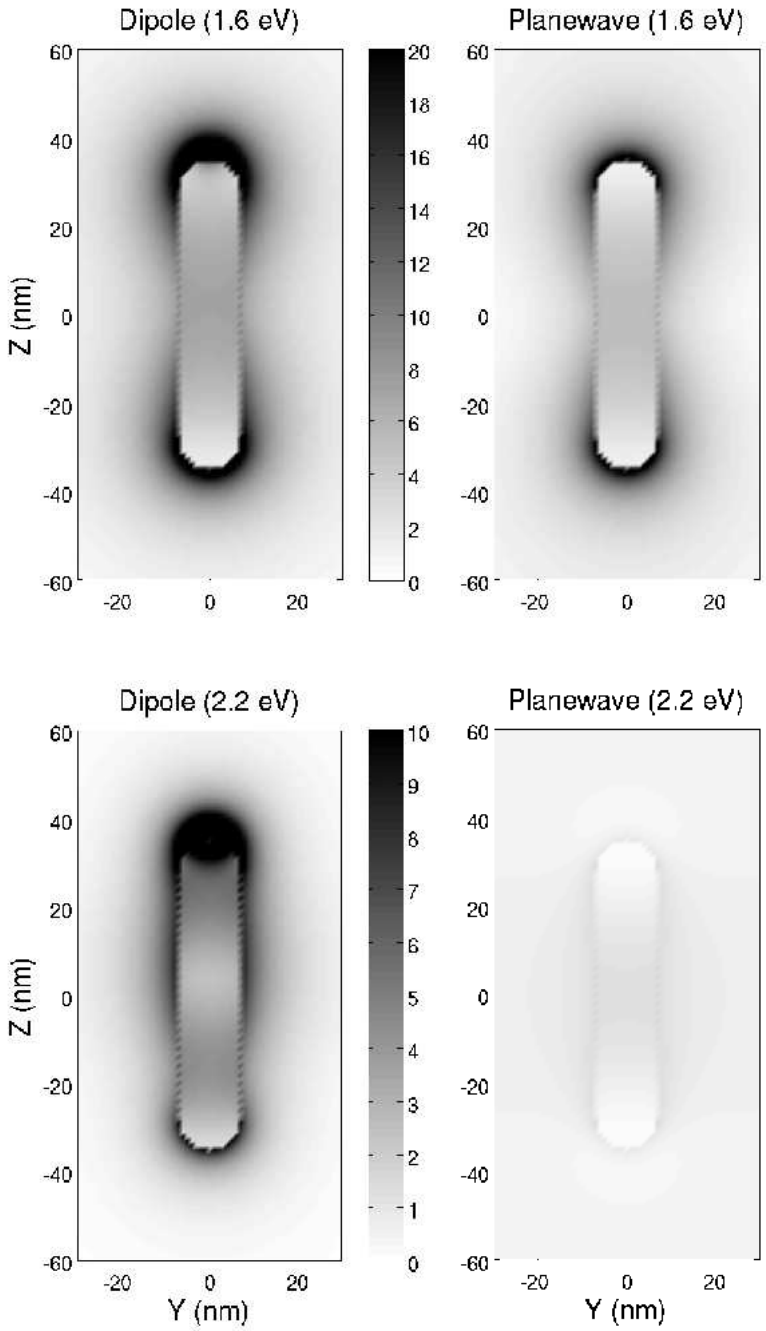

Figure 4.6: Magnitude of time average of electric field squared of 70 nm nanorod excited by a planewave and dipole source. The dipole source was placed 5 nm above the tip of the wire with a dipole moment of 1 e nm. (top) For the bright mode at 1.6 eV, there are hot spots in excess of 20 times the applied electric field for both the dipole and planewave. (bottom) The dark mode at 2.2 eV responds to the dipole source, but shows nearly no response to the planewave.

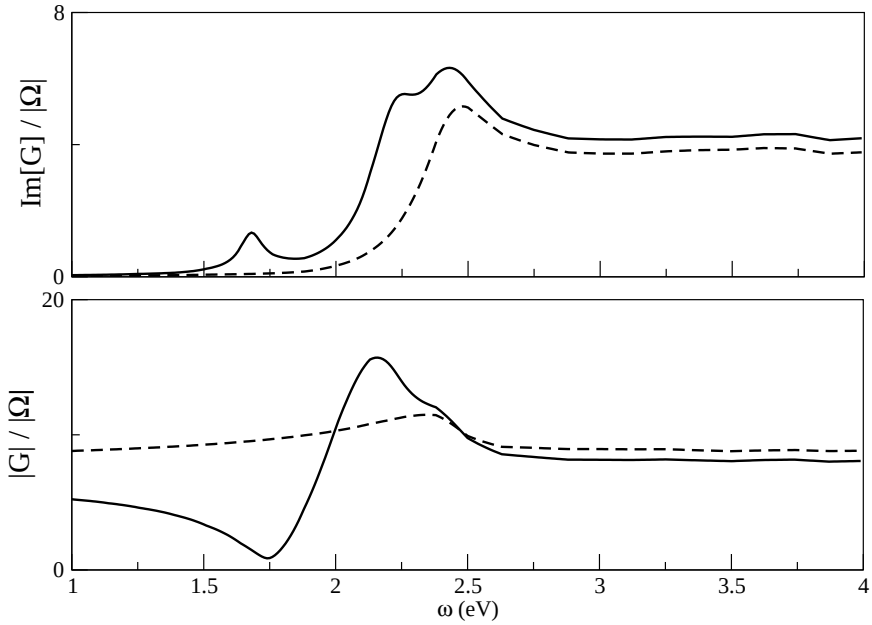

Figure 4.7: The ratios of G/Ω and G_I/Ω shown for a 70 nm length, 14 nm width nanorod (solid line) and a 7 nm radius spherical MNP (dashed line), with $\mu = 1.0$ e·nm. These two ratios play a large role in determining the system behavior.

4.4.1 Dynamics of a 70 nm Nanorod

Last chapter, we showed that by varying the SQD dipole moment and the radius of a spherical MNP, a large variety of system behavior is achievable. However, to reach the regimes of strongest coupling, relatively large values of the SQD dipole moment were needed, $\mu > 3$ e·nm (see Figure 3.2 in chapter 3). Such large values of the SQD dipole moment might not be experimentally possible due to the limit imposed by the SQD size and the relationship of SQD size to the exciton resonance. We will show for a nanorod rather than a spherical MNP, that the large local response of the wire makes the strong coupling regime accessible for smaller SQD dipole moments that are much more experimentally viable.

Here we illustrate a paradigm for designing systems biased towards specific

behavior with the example of a 70 nm length nanorod with a total width of 14 nm. We fix the SQD dipole moment at $\mu = 0.5$ e·nm. We have shown previously that suppression in the response of the SQD is controlled by the ratio of G/Ω and bistability in the system is turned on by the ratio G_I/Ω. We thus use the values of these two ratios to predict system behavior at a given frequency. As shown in figure 4.7, for a 70 nm nanorod, these two ratios can take on a larger range of values compared to those of a spherical MNP. In particular, the minimum of the ratio of the self-interaction to the coupling to the applied field, G/Ω, is nearly a order of magnitude smaller (9 to 1) for the nanorod, while it's maximum is approximately 40% larger.

Primary Plasmonic Peak (Bright State)

As shown in Figure 4.6, the bright state exhibits a large response in the MNP due to the dipole field of the SQD as well as to the plane wave. When the response of the nanorod is compared to that of a sphere, Ω is much larger than for a sphere (see figure 4.4). This enhancement of the local fields at the tips of the nanorod is simply due to a lightening rod effect. On the other hand, the differences in G between a nanorod and sphere are small compared to those in Ω. Thus, for the bright state, we expect the SQD to couple more to the plane wave than the self-interaction, and, due to the local field enhancement, to exhibit characteristics of much stronger applied field (such as increased broadness in the response).

When we take the exciton resonance to coincide with the bright plasmon peak (≈ 1.6 eV), we see a very broad response in the SQD (see figure 4.8), as well as a

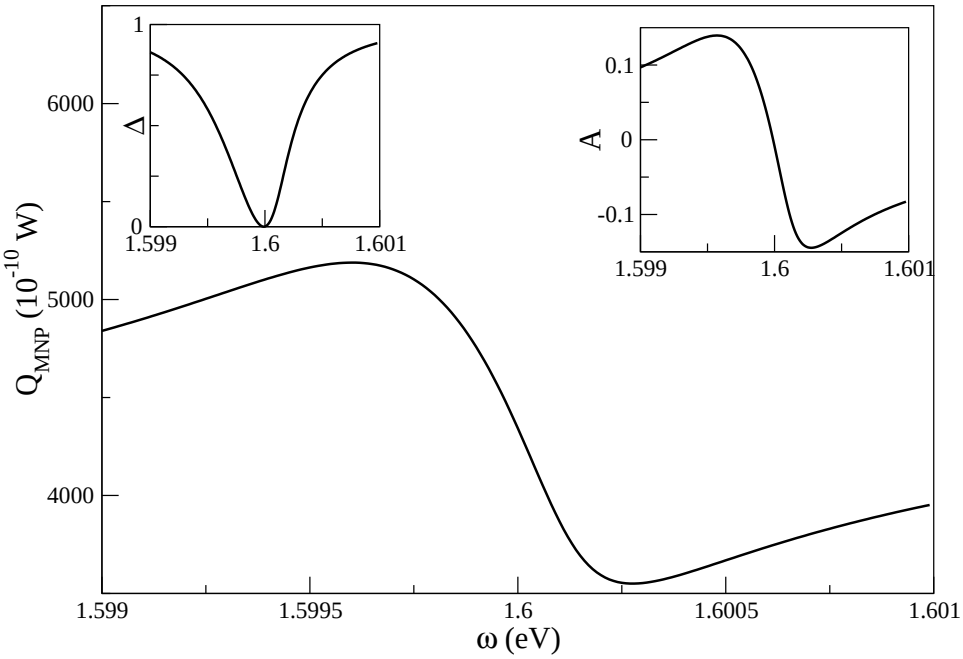

Figure 4.8: Bright state, with an exciton energy level at 1.6 eV, $L = 70$ nm, $w = 14$ nm, $\mu = 0.5$ e·nm. Absorption rate of the MNP, Q_{MNP}, population difference, Δ, and the real part of the SQD dipole moment, A, all show a very strong and broad response of the system.

broad Fano-like line shape in the absorption of the MNP, despite a rather modest value of the SQD dipole moment ($\mu = 0.5$ e·nm). When we compare this to a system consisting of a spherical MNP and a similarly sized SQD, the width of the population difference, Δ, is a full order of magnitude larger for a nanorod of this length (1 meV compared to 0.1 meV). This is due to the much stronger local near fields in the vicinity of the MNP incident on the SQD. This enhancement is due the increased response of the nanorod to a plane wave in comparison to that of a sphere.

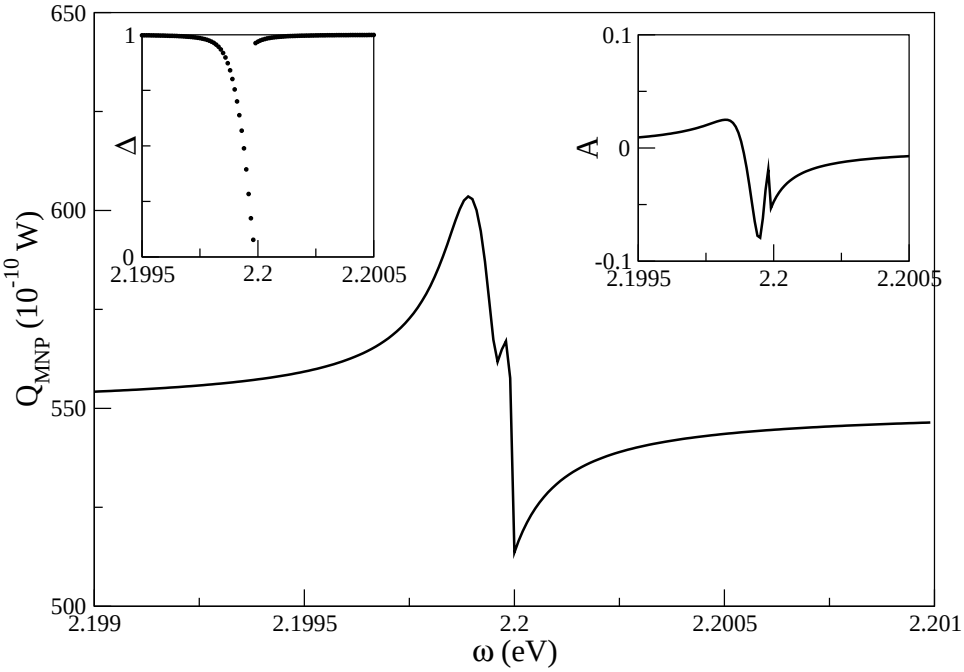

Figure 4.9: Dark state, with an exciton energy level at 2.2 eV, $L = 70$ nm, $w = 14$ nm, $\mu = 0.5$ e·nm. Absorption rate of the MNP, Q_{MNP}, and the real part of the SQD dipole moment, A, both show a bistability in the system. The population difference, Δ, shows a discontinuity and strong suppression in the excitation of the SQD.

Dark State

As shown in figure 4.6, the dark state is characterized by a large response in the MNP due to the dipole field of the SQD, but with little response to the plane wave. When we choose our exciton resonance to coincide with the frequency of the dark state, the SQD responds strongly to the self-interaction. Because the suppression regime as well as the bistable regime are controlled by the self-interaction strength relative to the coupling to the applied plane wave, both regimes of behavior are very easy to reach in this case.

With an SQD dipole moment of only $\mu = 0.5$ e·nm, we see very strong sup-

pression in the SQD response as well as the beginnings of bistability (see figure 4.9). Whereas with a spherical MNP with radius 7 nm would need a SQD with dipole moment of $\mu = 3\,\mathrm{e{\cdot}nm}$ to elicit a similar response[22].

Comparing the response of the dark state to that of the bright state, we see that the MNP absorption is an order magnitude greater for the bright state. For both the bright and dark states we have a Fano resonance in Q_{MNP}, which according to our previous investigations indicated the weakest level of coupling between the MNP and SQD. However, suppression and bistability of the SQD response evident in Figure 4.9 would indicate the strongest coupling regime. Thus, we see that these different types of hybrid behavior can coexist for an MNP nanorod.

4.4.2 Exciton Induced Transparency in the non-Retarded Limit

We found in the last chapter that for a spherical MNP in the dipole limit, the appearance of an exciton induced transparency is determined by the relation

$$\mu(a) \geqslant -\frac{2\pi\epsilon_B\epsilon_{\mathrm{effS}}R^3E_0}{s_\alpha A}\ , \tag{4.9}$$

which defines when the field from the SQD cancels the applied field inside the MNP. Note that this approximation applies because the field inside the MNP is constant and equal to the value at the center of the MNP. It is worth showing that this feature does in fact survive when a more thorough calculation is performed for a sphere utilizing a full electrodynamical calculation using the BEM.

For a spherical MNP with $a = 7\,\mathrm{nm}$ coupled to an SQD with a dipole moment of $\mu = 1\,\mathrm{e{\cdot}nm}$, we plot the square of the time average of the electric field (see figure

4.10). When the system is below resonance, we see a large response from the SQD as its dipole moment is very large and in phase with the applied field. We also see the dipole field extend into the MNP to a depth of $\approx 2\,\text{nm}$. At resonance, as the off-diagonal density matrix elements are nearly zero, the SQD dipole moment is much smaller, and we see a weaker dipole moment in the SQD. Also, the interference inside the MNP now causes a near cancellation of the field inside the MNP and we see an exciton induced transparency as we have previously predicted. Above resonance, the dipole field of the SQD is once again strong, but is now out of phase with the applied field.

For nanorods, the appearance of EXIT is problematic. From the relation describing the appearance of EXIT (equation 4.9), we expect that, with the large center to center separation inherent when using a nanorod as the MNP, EXIT will be attainable only for extremely large values of the SQD dipole moment. Also, the spatial variation of the field over a nanorod MNP is not properly accounted for in the dipole limit (which was used to generate this relation). When the full calculations are performed, EXIT is found to be very difficult to produce in a system with a nanorod. The spatial variation of the dipole field (from the SQD), over the length of a nanorod, can no longer cancel out the constant, applied field inside the MNP. The absorption still has a Fano-like line shape, but now the magnitude of the interference is too small in comparison to the applied field in order to produce a transparency.

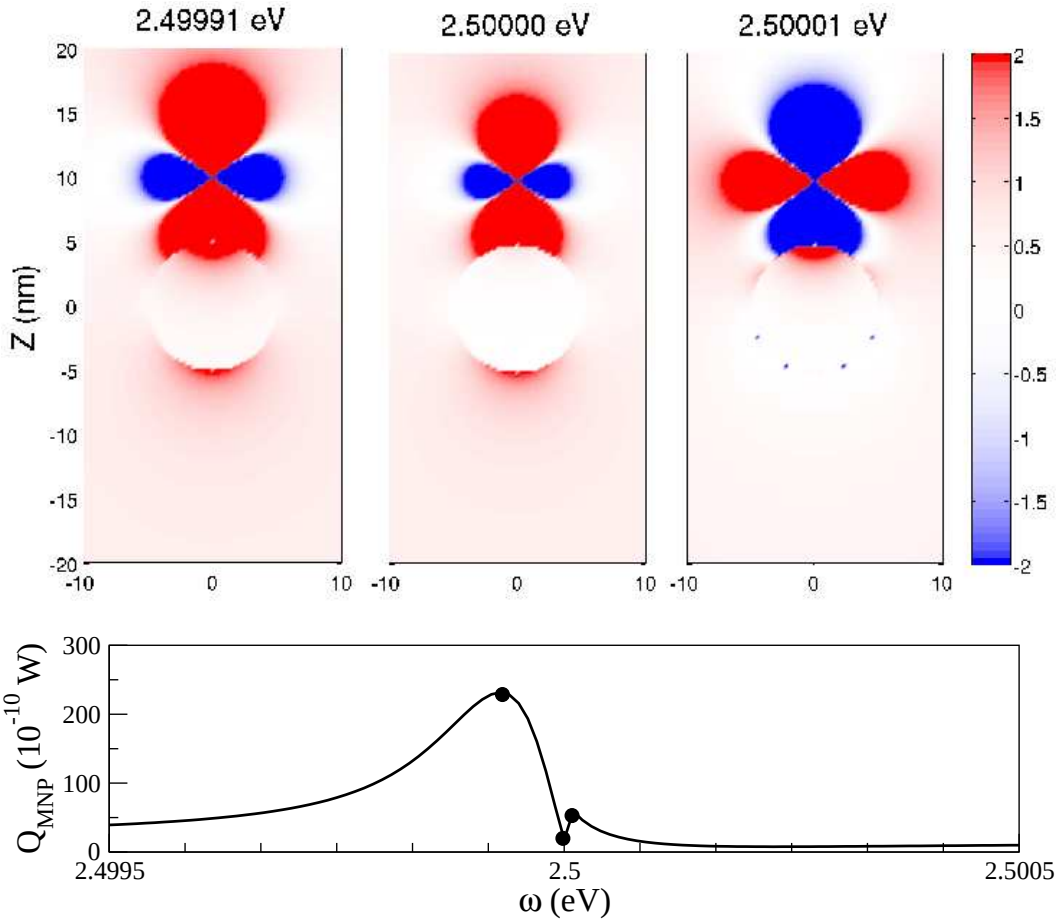

Figure 4.10: Near field of a 5 nm radius spherical MNP interacting with a SQD located 10 nm away from center for 3 values of applied frequency. Shown in color is the z component of the electric field. The first plot shows a strong dipole field from the SQD, in-phase with the applied field that penetrates the MNP to a depth of ≈ 2 nm. The middle plot show the system at resonance and the appearance of the exciton induced transparency in the MNP. The third plot shows a strong dipole field from the SQD, now out-of-phase with the applied field, that again penetrates the MNP to a depth of ≈ 1 nm.

4.5 Concluding Remarks

In this chapter, we have employed a full electrodynamical calculations of the near fields for MNP-SQD hybrid molecules based on the boundary element method (BEM). The method allows for tackling more complex geometries with a full description of the retarded optical response. Fields calculated were compared between those given by the BEM, those from a multipolar expansion, and those from the dipole approximation, and we examined the limits which can necessitate such a treatment.

Calculations performed on systems consisting of an SQD and a nanorod MNP showed that a broad range of system behavior can be reached experimentally much more easily than previously thought thanks to the field enhancement from the nanorod geometry. Furthermore, we saw how the response of the system could be tailored by engineering metal nanoparticle shape and the SQD resonance to manipulate the individual local near-fields that couple the MNPs and SQDs.

We also identified regimes where dark modes can influence hybrid response. Strong local field coupling via dark modes changes the interference and self-interaction effects dramatically. The external applied field does not directly drive this MNP dark mode, so SQD-MNP coupling is dominated by the SQD self-interaction. All of these aspects could enhance the capabilities of metal nanostructures to provide spatial and spectral control of the optical properties of single emitters.

Chapter 5

Multiple SQD Systems

In the previous two chapters we studied systems consisting of a single SQD coupled to MNPs of various shape. We now turn our attention to the response of a hybrid nanostructure molecule consisting of two SQDs and a single MNP. In particular, we will model the system using different approximation techniques. In doing so, we will identify and address issues in modeling the system using a semiclassical approach.

We will see that a semiclassical approach in modeling the coupling between the SQDs can lead to unstable, oscillatory and chaotic behavior in a strong SQD-SQD coupling regime. This nonlinear behavior is due to a breaking of the identical particle symmetry. Additionally, we will see that this chaotic behavior is closely related to the type of decoherence present in the system, specifically, whether the decoherence is collective or non-collective between the two SQDs. This provides insight into proper accounting of these important, but often neglected interactions.

We will then model the system using a more quantum mechanical approach, and note that this chaotic regime is absent. Finally, we will compare the two models on a system with a strong plasmon-mediated interaction between the SQDs and a weak direct interaction between them. In this case, we will see that while the results of the two models are similar, dipole blockade and the level splitting of the single

exciton states in the quantum model are non-trivial effects, even in this regime.

The layout of this chapter is as follows. We begin in section 1 with a quick review of recent work on this and similar systems. In section 2, we look at the SQD-MNP-SQD molecule in detail and discuss the ways in which we can model it. In section 3, we use a simple semiclassical approach to model the system and find a regime of highly chaotic behavior in the case of identical SQDs. We explore this behavior in detail and see that it is due to a symmetry breaking induced by non-collective decoherence. Additionally, we find that this chaotic behavior is removed from the system with an increased coupling to the MNP. The coupling to the classical plasmon of the MNP in this model effectively washes out the nonlinear effect. In section 4, we replace the semiclassical SQD-SQD direct coupling term with a quantum mechanical interaction term consistent with molecular quantum electrodynamics. In this case, we note the absence of the chaotic behavior. In its place, we find a dipole blockade induced by the splitting of the symmetric and antisymmetric SQD eigenstates. We then take a closer look at the dipole blockade and compare the two models in the weak SQD-SQD coupling regime. Finally, we present our conclusions in section 5.

5.1 Introduction

Recently, several theoretical investigations have gone beyond the semiclassical limit in studying this system by treating the plasmon-exciton interaction with quantum mechanical methods, such as treating the plasmon in the quasi-mode formal-

ism commonly employed in cavity quantum electrodynamics (QED) [58]. When the semiclassical results of a single quantum dot interacting with a metal nanoparticle are compared to a cavity QED treatment, the semiclassical results can be corrected by properly accounting for dephasing by using a random phase jump method [59]. Also, by using a Green's function approach to study a system comprised of two quantum emitters coupled through a nanorod, an optimal emitter-wire separation for excitation-plasmon conversion was found and plasmon mediated coupling between the two emitters was studied [60]. In addition to quantizing the local field produced by the metal particle, progress has been made in better understanding the inherent quantum properties of very small metal particles, including size quantization effects [61, 62] and the plasmon coupling to atomic-scale transport [63].

We discuss here the response of a hybrid nanostructure molecule consisting of two SQDs and a metal nanoparticle (MNP) subject to an applied electric field. The field couples to both of the SQDs as well as the MNP and all three constituents interact with each other through a dipole-dipole coupling. In order to model such a complex system, a number of approximation schemes must be employed. Different choices for the approximations made can result in predictions that differ both qualitatively and quantitatively. Therefore, a careful examination of the various techniques that are commonly employed is needed.

Furthermore, with two SQDs being considered as part of an open quantum system, the nature of the coupling to the bath is of increased importance. Two identical quantum objects, coupled in phase to the *same* bath mode, will decohere collectively. However, a slight detuning of their resonances will introduce a deco-

herence in each object independent of the other (and thus non-collective). Coupling to bath modes *internal* to each object respectively (exciton-phonon coupling inside a quantum dot for example [64]) introduces an additional source of non-collective decoherence. This question of collective vs non-collective decoherence can determine if and how a particle exchange symmetry can be broken, further complicating the modeling of the system.

The focus of this chapter is to identify and address these issues in modeling hybrid systems. Using a semiclassical approach to model the coupling between the SQDs, we find that such an approximation can lead to unstable, oscillatory and chaotic behavior in the strong SQD-SQD coupling regime. This nonlinear behavior is shown to be due to a breaking of the identical particle exchange symmetry. When the system is modeled using a quantum mechanical model for the SQD-SQD coupling, this instability is removed. Additionally, we see that this chaotic behavior is closely related to the type of decoherence present in the system, specifically, whether the decoherence is collective or non-collective between the two SQDs.

5.2 SQD-MNP-SQD Hybrid Molecule

Consider a hybrid molecule composed of two SQDs with radii r_1 and r_2 interacting with a spherical MNP of radius a. The MNP is centrally located between the two SQDs, which are located at distances R_1 and R_2 respectively from the center of the MNP (see Figure 5.1). The entire system is subject to an applied electric field $E = E_0 \cos(\omega t)$.

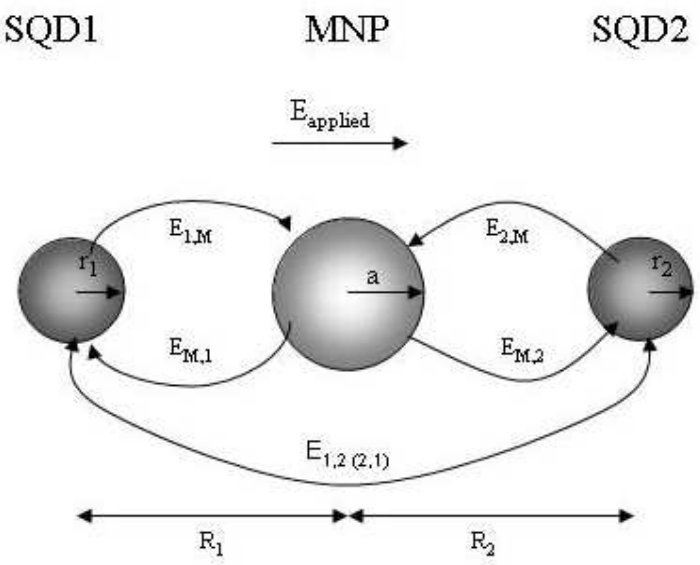

Figure 5.1: An applied field induces a polarization in the MNP and both SQDs, which in turn allows for a dipole-dipole coupling between the three particles.

As in previous chapters, we model the SQDs as spherical semiconductors with a dipole located at the center of each. We treat each SQD as effective two level quantum systems in the density matrix formalism with exciton energies $\hbar\omega_1$ and $\hbar\omega_2$, transition dipole moments μ_1 and μ_2, and dielectric constants ϵ_1 and ϵ_2. We treat the MNP as a classical spherical dielectric particle with dielectric function $\epsilon_M(\omega)$.

We now turn our attention to the interactions of our system. Each quantum dot participates in three interactions. The first is the direct coupling to the applied field. Second, each SQD interacts with the electric field produced by the MNP. Last, the SQDs interact with each other. Similarly, the MNP responds to the applied field as well as to each SQD. We solve the system self-consistently.

We begin by writing down the Hamiltonian for the system, $\mathcal{H}_{total}$, as

$$\begin{aligned}\mathcal{H}_{total} =&\hbar\omega_1\hat{a}_1^\dagger\hat{a}_1 + \hbar\omega_2\hat{a}_2^\dagger\hat{a}_2 + \mathcal{H}_{1\leftrightarrow 2} \\ &- \mu_1 E_{\text{SQD1}}\left(\hat{a}_1 + \hat{a}_1^\dagger\right) - \mu_2 E_{\text{SQD2}}\left(\hat{a}_2 + \hat{a}_2^\dagger\right)\end{aligned}$$

where $\hat{a}_{1(2)}$ and $\hat{a}_{1(2)}^\dagger$ are the exciton annihilation and creation operators for SQD1(2) and $\mathcal{H}_{1\leftrightarrow 2}$ represents the direct coupling between SQD1 and SQD2. E_{SQD1} is the electric field at the center of SQD1 that consists of the applied, external field, E, and the induced field produced by the polarization of the MNP, $E_{M,1}$. Thus E_{SQD1} is

$$E_{\text{SQD1}} = \frac{1}{\epsilon_{\text{eff1}}}(E + E_{M,1}) \ , \tag{5.1}$$

where $\epsilon_{\text{eff1}} = \frac{2\epsilon_{\text{B}}+\epsilon_1}{3\epsilon_{\text{B}}}$ is the screening factor of SQD1. The field on SQD1 from the MNP is

$$E_{M,1} = \frac{1}{4\pi\epsilon_{\text{B}}}\frac{s_\alpha P_{\text{MNP}}}{R_1^3} \ , \tag{5.2}$$

where $s_\alpha = 2(-1)$ when the applied field is parallel (perpendicular) to the major axis of the system, (E_{SQD2} is calculated similarly).

As before, working in the dipole limit, the polarization of the MNP is (see [54]),

$$\begin{aligned}P_{\text{MNP}} = (4\pi\epsilon_{\text{B}})\gamma a^3(E &+ \frac{1}{4\pi\epsilon_{\text{B}}}\frac{s_\alpha P_{\text{SQD1}}}{\epsilon_{\text{eff1}}R_1^3} \\ &+ \frac{1}{4\pi\epsilon_{\text{B}}}\frac{s_\alpha P_{\text{SQD2}}}{\epsilon_{\text{eff2}}R_2^3})\end{aligned}$$

where $\gamma = \frac{\epsilon_M(\omega)-\epsilon_{\text{B}}}{2\epsilon_{\text{B}}+\epsilon_M(\omega)}$. Making use of the density matrix ρ to calculate the polarization of the SQD, we take the ensemble average of the dipole moment. We take as our states $|1\rangle = |00\rangle$, $|2\rangle = |10\rangle$, $|3\rangle = |01\rangle$ and $|4\rangle = |11\rangle$ (where, for example, $|10\rangle$

is the state with SQD1 excited and SQD2 in its ground state). We then have $P_{\mathrm{SQD1}} = \mu_1(\rho_{12} + \rho_{21} + \rho_{34} + \rho_{43})$ and $P_{\mathrm{SQD2}} = \mu_2(\rho_{13} + \rho_{31} + \rho_{24} + \rho_{42})$(see [48]). This allows us to write down E_{SQD1}, but we still need an expression for $\mathcal{H}_{1\leftrightarrow 2}$ in order to complete our calculation of $\mathcal{H}_{total}$.

5.2.1 The SQD-SQD Interaction

We have several choices for the SQD-SQD coupling terms in our Hamiltonian. If we treat the field produced by the SQD1 as a classical electric field produced by a dipole with polarization, $P_{\mathrm{SQD1}} = \mu_1(\rho_{12} + \rho_{21} + \rho_{34} + \rho_{43})$ (similarly for SQD2), as we did in treating SQD-MNP interactions, then we have

$$\begin{aligned}
\mathcal{H}_{1\leftrightarrow 2} &= -\mu_1 \vec{\mathbf{E}}_{2\rightarrow 1}(\hat{a}_1 + \hat{a}_1^\dagger) - \mu_2 \vec{\mathbf{E}}_{1\rightarrow 2}(\hat{a}_2 + \hat{a}_2^\dagger) \\
\mathcal{H}_{1\leftrightarrow 2} &= -\mu_1 \frac{1}{4\pi\epsilon_{\mathrm{B}}} \frac{s_\alpha P_{\mathrm{SQD2}}}{\epsilon_{\mathrm{eff2}}\epsilon_{\mathrm{eff1}}(R_1 + R_2)^3} \ (\hat{a}_1 + \hat{a}_1^\dagger) \\
&\quad - \mu_2 \frac{1}{4\pi\epsilon_{\mathrm{B}}} \frac{s_\alpha P_{\mathrm{SQD1}}}{\epsilon_{\mathrm{eff1}}\epsilon_{\mathrm{eff2}}(R_1 + R_2)^3} \ (\hat{a}_2 + \hat{a}_2^\dagger) \,.
\end{aligned}$$

In taking this approach, we are assuming that we can replace a quantized field, produced by the exciton, with a mean field value computed by the density matrix. This is a semiclassical approximation.

Alternatively, we can calculate this interaction with quantum electrodynamics. Two identical, two-level molecules interacting with a common electromagnetic mode, with a radiative decay rate, $\gamma = \frac{1}{\tau}$, separated by a distance d, have an interaction Hamiltonian of the form [65]

$$\mathcal{H}_{1\leftrightarrow 2} = \hbar\,\delta\,(\hat{a}_1 + \hat{a}_1^\dagger)\,(\hat{a}_2 + \hat{a}_2^\dagger)\,, \tag{5.3}$$

where δ, the interaction energy, is calculated in the dipole limit as

$$\delta = \frac{3}{4\tau}\Bigg(\left(\cos^2(\theta) - 1\right) \frac{\cos(\zeta)}{\zeta} + \left(1 - 3\cos^2(\theta)\right)\left(\frac{\cos(\zeta)}{\zeta^3} + \frac{\sin(\zeta)}{\zeta^2}\right)\Bigg),$$

where $\zeta = \frac{\omega d}{c}$, c is the speed of light, and θ denotes the phase difference of the bath mode at the locations of the two molecules.

5.2.2 Numerical Calculations

Similar to previous chapters, we take E parallel to the axis of our SQD-MNP-SQD molecule (unless otherwise noted) i.e., $s_\alpha = 2$, and we take the dielectric constant of the background to be $\epsilon_B = \epsilon_0$. For the MNP, we take $\epsilon_M(\omega)$ as the bulk dielectric constant of gold as found experimentally [55]. For a small, spherical, gold MNP, the response has a broad plasmon peak near 2.4 eV with a width of approximately 0.25 eV. We let the radius of the MNP vary between 3 and 8 nm.

For the SQDs, we take $\epsilon_1 = \epsilon_2 = 6\,\epsilon_0$ and for the exciton resonant frequency we take it to be 2.5 eV, which is near the broad plasmon frequency of gold. For the MNP size regime we consider, the plasmon resonance for a sphere varies little with particle size. However, the size, shape and material of the SQD strongly determine both the exciton energy level and its dipole moment. In this chapter, we again consider the simplest model and ignore this size dependence.

5.3 Semiclassical Approach to SQD-SQD coupling

We first model the system using the semiclassical approximation for the SQD-SQD coupling. Our Hamiltonian becomes

$$\begin{aligned}\mathcal{H}_{total} =&\hbar\omega_1\hat{a}_1^\dagger\hat{a}_1 + \hbar\omega_2\hat{a}_2^\dagger\hat{a}_2 \\ &- 2\hbar\cos\omega t\ \Omega_1\left(\hat{a}_1 + \hat{a}_1^\dagger\right) - 2\hbar\cos\omega t\ \Omega_2\left(\hat{a}_2 + \hat{a}_2^\dagger\right) \\ &- \hbar G_1(\rho_{12} + \rho_{21} + \rho_{34} + \rho_{43})\left(\hat{a}_1 + \hat{a}_1^\dagger\right) \\ &- \hbar G_2(\rho_{13} + \rho_{31} + \rho_{24} + \rho_{42})\left(\hat{a}_2 + \hat{a}_2^\dagger\right) \\ &- \hbar F(\rho_{12} + \rho_{21} + \rho_{34} + \rho_{43})\left(\hat{a}_2 + \hat{a}_2^\dagger\right) \\ &- \hbar F(\rho_{13} + \rho_{31} + \rho_{24} + \rho_{42})\left(\hat{a}_1 + \hat{a}_1^\dagger\right)\end{aligned}$$

where, similar to previous chapters, we define

$$\begin{aligned}G_1 &= \frac{\gamma a^3\mu_1^2 s_\alpha^2}{4\pi\epsilon_{\mathrm{B}}\ \epsilon_{\mathrm{eff1}}\ \hbar R_1^6} \\ \Omega_1 &= \frac{E_0\mu_1}{2\hbar}(1 + \frac{\gamma a^3 s_\alpha}{\epsilon_{\mathrm{effM}} R_1^3}) \\ F &= \frac{\mu_1\mu_2 s_\alpha^2}{4\pi\epsilon_{\mathrm{B}}\ \epsilon_{\mathrm{eff1}}\ \epsilon_{\mathrm{eff2}}\ \hbar}\left(\frac{1}{(R_1+R_2)^3} + \frac{\gamma a^3}{R_1^3 R_2^3}\right),\end{aligned}$$

and G_2 and Ω_2 are defined similarly. G_1 arises when the applied field polarizes SQD1, which in turn polarizes the MNP and then produces a field to interact back on SQD1. This can be thought of as the self-interaction of SQD1 because this coupling to SQD1 depends on the polarization of SQD1. The first term in Ω_1 is just the direct coupling to the applied field and the second term is the field from the MNP that is induced by the applied field. F arises from the interaction between the two dots. The first term is the direct coupling and the second term is the interaction

mediated by the MNP.

We once again write down the master equation,

$$\dot{\rho} = \frac{i}{\hbar}[\rho, \mathcal{H}_{SQD}] - \Gamma(\rho) \tag{5.4}$$

where $\Gamma(\rho)$ is now the 4x4 relaxation matrix. To find the entries of $\Gamma(\rho)$, we assume the baths of our SQDs are uncorrelated. For a non-interacting system, we could write $\rho = \rho^{(2)} \otimes \rho^{(1)}$ where $\rho^{(1)}$ and $\rho^{(2)}$ are the 2x2 density matrix in the single SQD case for SQD1 and SQD2 respectively, and ρ is the 4x4 density matrix for the combined system. We use this relation and the relaxation matrix for a single SQD with entries $\Gamma_{11}^{(1)} = \frac{\rho_{11}^{(1)}-1}{\tau_1}$,$\Gamma_{12}^{(1)} = \Gamma_{21}^{(1)*} = \frac{\rho_{12}^{(1)}}{T_1}$ and $\Gamma_{22}^{(1)} = \frac{\rho_{22}^{(1)}}{\tau_1}$ where the superscript indicates this is for SQD1 (similarly for SQD2). Making use of the master equation and $\rho = \rho^{(2)} \otimes \rho^{(1)}$, we arrive at the 4x4 matrix, $\Gamma(\rho)$ for a noninteracting 2 SQD system

$$\Gamma(\rho) = \begin{pmatrix} -\frac{\rho_{22}}{\tau_1} - \frac{\rho_{33}}{\tau_2} & \frac{\rho_{12}}{T_1} - \frac{\rho_{34}}{\tau_{20}} & \frac{\rho_{13}}{T_2} - \frac{\rho_{24}}{\tau_1} & \frac{\rho_{14}}{T_1} + \frac{\rho_{14}}{T_2} \\ \frac{\rho_{21}}{T_1} - \frac{\rho_{43}}{\tau_2} & \frac{\rho_{22}}{\tau_1} - \frac{\rho_{44}}{\tau_{20}} & \frac{\rho_{23}}{T_1} + \frac{\rho_{23}}{T_2} & \frac{\rho_{24}}{T_2} + \frac{\rho_{24}}{\tau_1} \\ \frac{\rho_{31}}{T_2} - \frac{\rho_{42}}{\tau_1} & \frac{\rho_{32}}{T_1} + \frac{\rho_{32}}{T_2} & \frac{\rho_{33}}{\tau_2} - \frac{\rho_{44}}{\tau_1} & \frac{\rho_{34}}{T_1} + \frac{\rho_{34}}{\tau_2} \\ \frac{\rho_{41}}{T_1} + \frac{\rho_{41}}{T_2} & \frac{\rho_{42}}{T_2} + \frac{\rho_{42}}{\tau_1} & \frac{\rho_{43}}{T_1} + \frac{\rho_{43}}{\tau_2} & \frac{\rho_{44}}{\tau_1} + \frac{\rho_{44}}{\tau_2}. \end{pmatrix}$$

We assume that the same $\Gamma(\rho)$ applies if the two dots interact and ρ is no longer separable.

Again, from looking at the single dot case, we make the following factorizations

analogous to those made in previous chapters:

$$\begin{aligned}
\rho_{12} &= (A_{12} + iB_{12})e^{i\omega t} \\
\rho_{13} &= (A_{13} + iB_{13})e^{i\omega t} \\
\rho_{14} &= (A_{14} + iB_{14})e^{2i\omega t} \\
\rho_{23} &= (A_{23} + iB_{23}) \\
\rho_{24} &= (A_{24} + iB_{24})e^{i\omega t} \\
\rho_{34} &= (A_{34} + iB_{34})e^{i\omega t},
\end{aligned} \tag{5.5}$$

along with the reminder that $\rho_{ij} = \rho^*_{ji}$. Making use of these definitions and the rotating wave approximation, we arrive at a set of 16 coupled, nonlinear differential equations. For the SQD relaxation times in this model, we take $\tau_1 = \tau_2 = 0.8\,\text{ns}$ and $T_1 = T_2 = 0.3\,\text{ns}$.

5.3.1 Weak Field Limit

In Figure 5.2, we plot the response of the SQD-MNP-SQD system and that of the SQD-MNP system in the weak field limit (intensity of 1 W/cm^2). For each system, we plot the absorption of the SQD(s), Q_{SQD}, the absorption of the MNP, Q_{MNP}, and the absorption of the total system, Q_{total}. In all the plots, we see that the peak of the response both shifts and broadens for small values of particle separation. The shift and broadening of this resonance peak when the particles are very close shows a hybrid excitation with a shortened lifetime.

When we compare the response of the SQD-MNP-SQD system (top of Figure 5.2) to that of the the single SQD coupled to a spherical MNP (bottom of Figure 5.2),

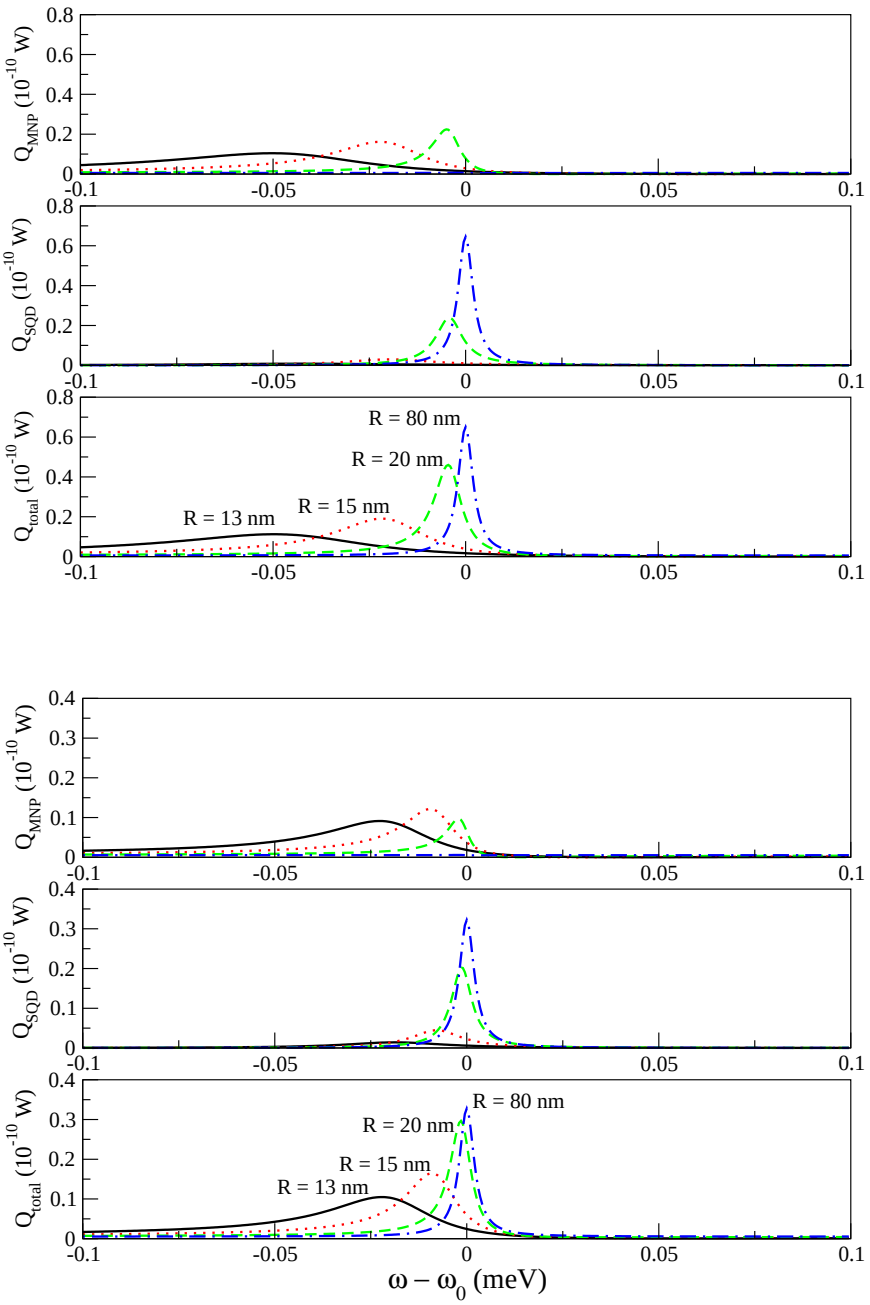

Figure 5.2: Energy absorption due to the MNP, energy absorption due to the SQD, and the total energy absorption, respectively, as a function of detuning, for two SQDs coupled to a spherical MNP (top), and for a single SQD coupled to a spherical MNP (bottom). All calculations were in the weak field limit and particle separation was varied (the two SQD case was treated symmetrically, $R = R_1 = R_2$, $\mu = \mu_1 = \mu_2$ and $\omega_0 \equiv \omega_1 = \omega_2$). In both sets of plots we take $a = 7.5$ nm and $\mu = 0.5\,\mathrm{e{\cdot}nm}$.

we find an overall enhancement of the interaction. We first note that the magnitude of the absorption is nearly doubled when compared to the single SQD case for most particle separations. When the particles are far apart, the interparticle coupling is weak, and most of the absorption is due to the SQDs. Thus, the doubling is simply the absorption of the additional SQD. When the particles are close together, the interparticle coupling is strong and most of the absorption is in the MNP. The peak of the absorption in this case is due to the constructive interference of fields at the MNP, from the SQDs. Thus, the additional SQD doubles the magnitude of this field.

In addition to enhancing the magnitude of the absorption, we also have an increase in the interparticle coupling strength. This is evident in the increased shifting and slight broadening of the response, for a given R, when compared to the single SQD case. This shifting of the resonance indicates that a smaller particle separation is needed in the single SQD-MNP molecule than in the SQD-MNP-SQD system to achieve a similar hybrid response.

5.3.2 Strong Field Limit: a vs. μ Parameter Space

We now consider the large field limit as previously defined [20] (intensity of 10^3 W/cm^2). As we did previously, by manipulating a and μ ($\mu \equiv \mu_1 = \mu_2$), which are effectively the sizes of the MNP and the SQDs, we can change the relative strengths of the local fields and, in turn, the strengths of the five different couplings (G, and the two terms that make up each of Ω and F). Looking at the solutions to

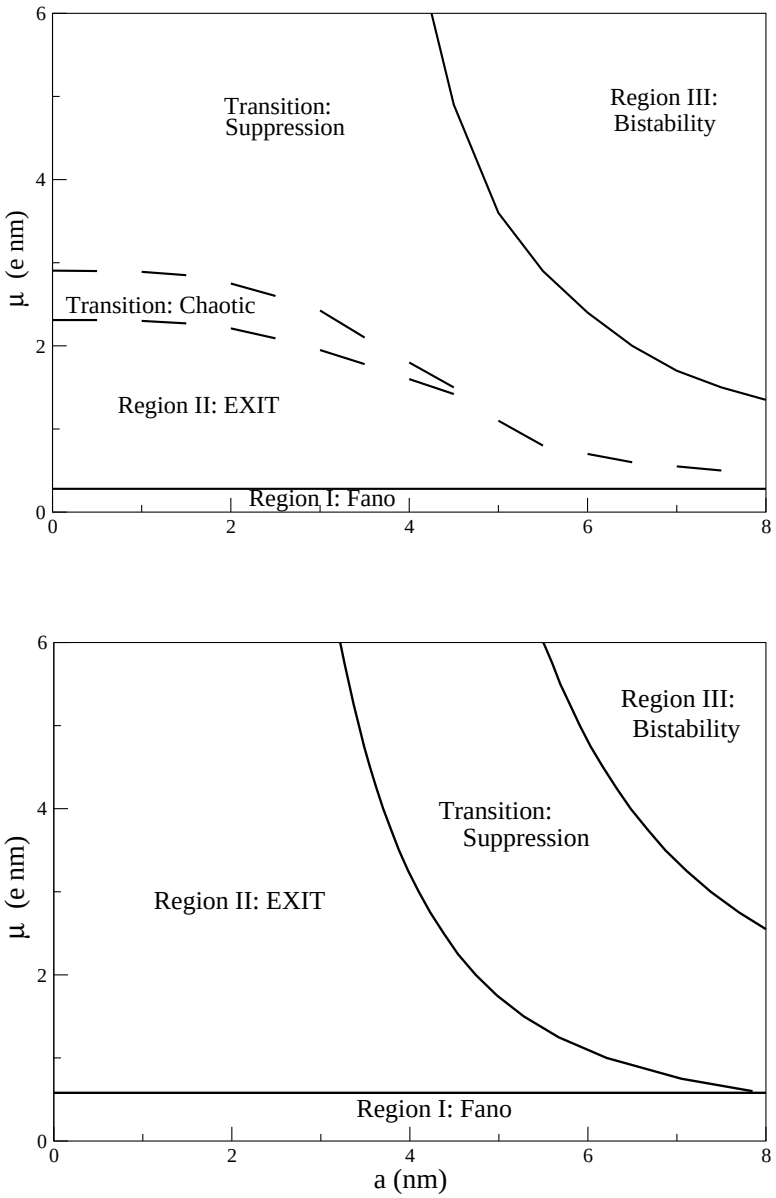

Figure 5.3: μ vs. a phase diagrams in the strong field limit for an SQD-MNP system (bottom) and an SQD-MNP-SQD system (top). Single SQD system shows 4 regimes of behavior and SQD-MNP-SQD system shows 5 regimes of hybrid behavior. In both plots, the SQD-MNP separation was 13 nm.

the differential equations, both dynamically and in the steady state limit, there are five distinct regimes of behavior in the a vs. μ parameter space for a double SQD molecule (see the top of Figure 5.3). Regions I, II and III, as well as the Suppression regime, were discussed in detail for an SQD-MNP molecule in chapter 3 (see also [21, 22]). The new regime of behavior will be discussed below.

Comparing the parameter space diagram of the SQD-MNP-SQD molecule to that of the SQD-MNP molecule (bottom of Figure 5.3), we note several differences. First, we see that the threshold separating Region I and II is at a value of μ which is about half of that in the single SQD case. We saw in chapter 3 that the appearance of an exciton induced transparency (EXIT) occurs when the induced electric fields from the SQD overtake the applied field in magnitude at the location of the MNP. However, the addition of the second SQD effectively doubles the size of this internal field, which could equivalently be produced by a single SQD with twice as large of a dipole moment. There is a similar effect that shifts regions II and III, as well as shifting the emergence of suppression.

Previously, we have shown that the appearance of bistability in the system is caused by feedback through the self-interaction of the SQD. With the addition of a second SQD, there is increased feedback through the SQD-SQD interaction, which leads to an enlargement in Region III. This SQD-SQD interaction also provides the feedback for the constructive and destructive interference that leads to suppression. We see that not only does this enhance these effects, but also allows for the appearance of suppression even without the MNP, which obviously cannot occur in the single SQD case. For an SQD-SQD molecule, the self-interaction is mediated by the

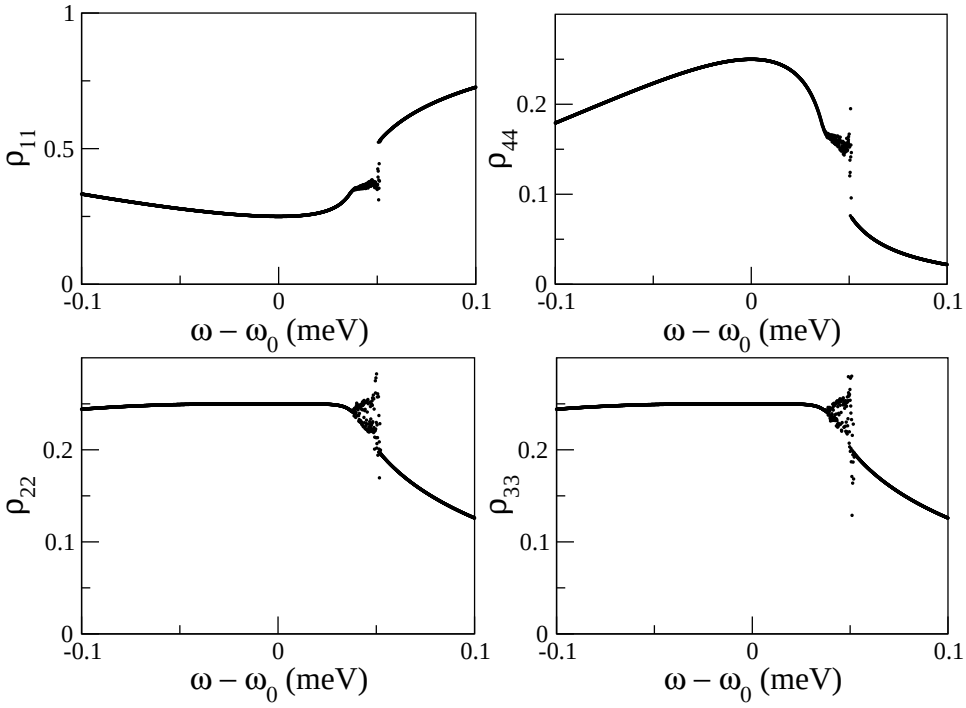

Figure 5.4: Density matrix elements plotted as a function of detuning for two interacting, strongly coupled SQDs ($a = 0\,\text{nm}$, $\mu_1 = \mu_2 = 3.0\,\text{e·nm}$ and $R_1 = R_2 = 13\,\text{nm}$). The response of the system shows discontinuity for detunings near 0.05 meV. For these frequencies, the system no longer reaches a steady state.

coupling to the other SQD.

5.3.3 Transition: Chaotic Solutions

In addition to the enhancement in the appearance of EXIT, suppression and bistability, we also note that the transition region is more complicated than in the single SQD case: chaotic behavior emerges from a strong SQD-SQD interaction. In fact, strong coupling to the MNP provides a quenching for this effect. Subsequently, it is best studied in the limit where there is no MNP ($a = 0$).

In this transition regime, for a range of frequencies just above the natural

resonance of the SQDs, the system no longer reaches a steady state (see Figure 5.4). In this frequency range ($\omega - \omega_0 \approx 35 - 50\,\mu$eV with $\omega_0 \equiv \omega_1 = \omega_2$, for $a = 0\,$nm, $\mu_1 = \mu_2 = 3.0\,$e·nm and $R_1 = R_2 = 13\,$nm), the solutions oscillate within a narrow envelope. We also note that despite the symmetry between the two SQDs, the population densities for the singly excited SQD states, ρ_{22} and ρ_{33}, are no longer identical for these solutions. Thus, we speculate that noise in the numerical calculations causes the symmetry to be broken. In fact, when the calculations are performed with increasingly greater numerical precision, much of this chaotic behavior can be eliminated. However, in all calculations performed, it could never be removed completely and the numerical precision required (less than 1 part in 10^{10}) far exceeded the amount of natural noise a realistic system would exhibit by many orders of magnitude.

5.3.3.1 Explicit Symmetry Breaking

In order to explore the effect of the SQD-SQD identical particle symmetry, we look at the effect of breaking it explicitly. Again, this can best be done without the presence of the MNP, and by slightly shifting the dipole moment, or the bare resonance frequency of one of the SQDs. However, care must be taken when detuning the SQD resonances as too large of a shift could cause them to uncouple.

When the SQD-SQD symmetry is broken explicitly, the chaotic behavior is amplified. Shown in Figure 5.5 is the response of the system under four different cases of symmetry breaking. If we compare the responses shown in Figure 5.5 to

those of Figure 5.4, we can see that the frequency range over which the system displays this oscillatory behavior increases when the symmetry is broken explicitly. As noted above, when only numerical rounding provides the symmetry breaking, the range of driving frequencies over which the system exhibits the chaotic behavior is only $15\,\mu$eV. However, when the symmetry is broken explicitly, by either shifting one of the bare SQD resonances or by increasing one of the SQD dipole moments, this frequency range increases to around $125\,\mu$eV, nearly a full order of magnitude increase. This increase occurs even when the symmetry is broken by a trivial amount (1 part in 10^8) and increasing the numerical accuracy of the calculations no longer has any effect in reducing the chaotic behavior.

We also note that varying the amount by which the symmetry is broken is largely unimportant on the size of this frequency window. Once a certain threshold is reached, the frequency range of the chaotic behavior reaches a maximum, as does the envelope in which the solutions oscillate in. One can notice, however, that there is a small transition from the behavior shown in Figure 5.4 and that in Figure 5.5, which can be seen in the two rightmost plots in Figure 5.5. The chaotic oscillations start from the edges of a frequency window with the innermost points displaying a more regular oscillatory nature.

If we focus on a particular value of detuning that leads to the chaotic behavior, we see that the time evolution for that particular frequency is complicated, but more structured than scanning over the detuning would lead one to believe (Figure 5.5). In Figure 5.6 we see that the system initially undergoes fast oscillations due to Rabi flopping and the slight detuning ($t = 0$ to $\sim 1\,$ns). The system then set-

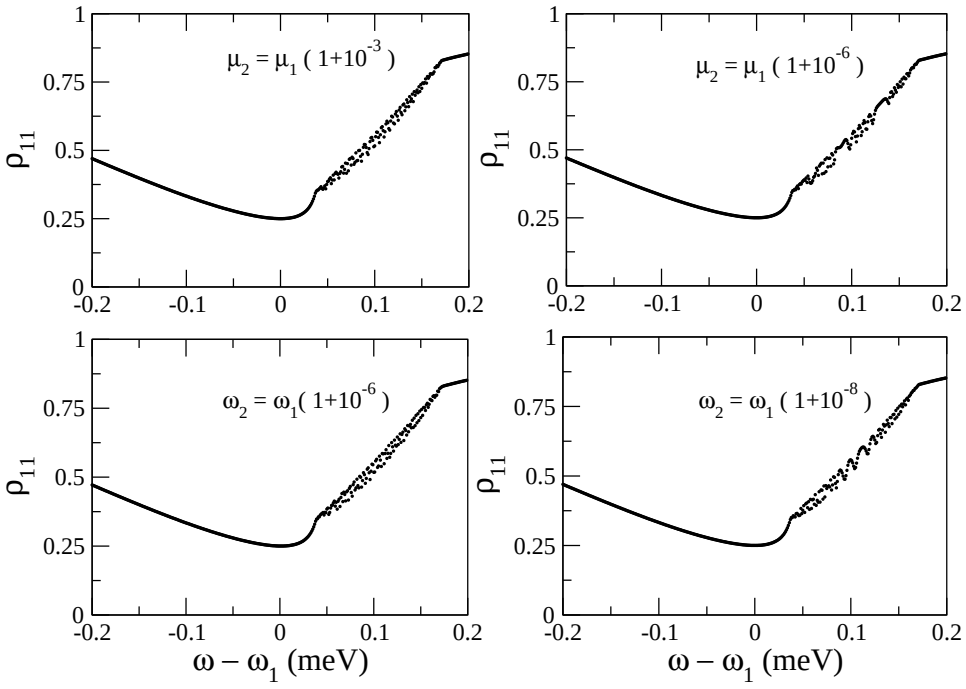

Figure 5.5: ρ_{11} plotted as a function of the detuning between the driving field and SQD1 for four cases of explicit symmetry breaking. In all cases $a = 0\,\text{nm}$, $\mu_1 = 3.0\,\text{e}\cdot\text{nm}$ and $R_1 = R_2 = 13\,\text{nm}$ were held fixed. The top two plots show $\mu_2 \to \mu_1 + \delta$ symmetry breaking with $\omega_1 = \omega_2$. The bottom two plots show $\omega_2 \to \omega_1 + \delta$ symmetry breaking with $\mu_1 = \mu_2$.

tles into what would be a typical steady state solution. Then, at a point between 2 and 5 ns, the system again acts as though it is far from equilibrium and undergoes large oscillations. Within a further 2 ns the system then settles into a stable and undamped oscillatory behavior. So, although the behavior appears to be very noisy when viewed as a function of driving frequency, for each particular frequency the behavior is very different than that of the weak coupling regime, but is still predictable.

Furthermore, the frequency of these secondary oscillations is also unaffected by the degree of the symmetry breaking present in the system (see insets of Figure 5.6).

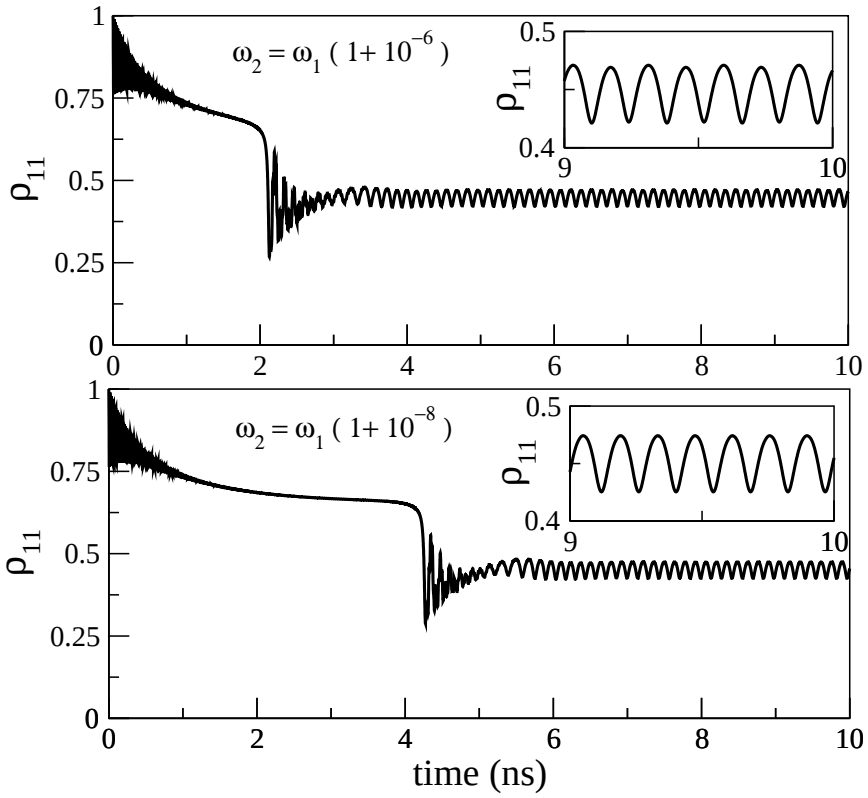

Figure 5.6: Evolution of ρ_{11} as a function of time, for $a = 0\,\text{nm}$, $\mu_1 = \mu_2 = 3.0\,\text{e·nm}$, $R_1 = R_2 = 13\,\text{nm}$, and $\omega_1 = 2.5\,\text{eV}$, for a driving frequency in the chaotic regime ($\omega - \omega_1 = 0.75\,\text{meV}$). Shown are the oscillations for an explicit symmetry breaking of $\omega_2 = \omega_1(1 + 10^{-6})$ (top) and $\omega_2 = \omega_1(1 + 10^{-8})$ (bottom). Insets shows that the frequency of oscillation does not appear to depend on the amount of the symmetry breaking.

From the time evolution of ρ_{11} (for $a = 0\,\text{nm}$, $\mu_1 = \mu_2 = 3.0\,\text{e·nm}$, $R_1 = R_2 = 13\,\text{nm}$, and $\omega_1 = 2.5\,\text{eV}$), for a driving frequency in the chaotic regime ($\omega - \omega_0 = 0.75\,\text{meV}$), we see that the oscillations for an explicit symmetry breaking of $\omega_2 = \omega_1(1 + 10^{-6})$ and $\omega_2 = \omega_1(1 + 10^{-8})$ have nearly the same frequency (to better than 1 part in 10^3). However, the onset into the oscillatory behavior can be significantly different, even for these small symmetry breaking terms, with oscillatory behavior onset earlier in

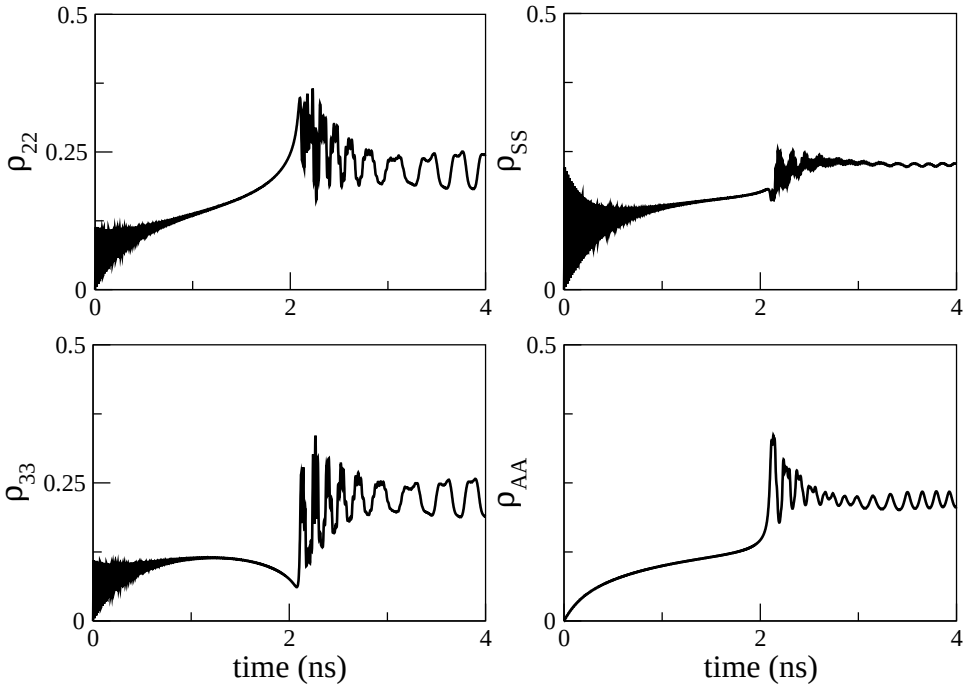

Figure 5.7: Time evolution of ρ_{22}, ρ_{33}, $\rho_{\rm SS}$ and $\rho_{\rm AA}$, for $a = 0\,\text{nm}$, $\mu_1 = \mu_2 = 3.0\,\text{e·nm}$, $R_1 = R_2 = 13\,\text{nm}$, $\omega_1 = 2.5\,\text{eV}$ and $\omega_2 = \omega_1(1 + 10^{-6})$, for a driving frequency in the chaotic regime ($\omega - \omega_1 = 0.75\,\text{meV}$). ρ_{22}, ρ_{33}, and $\rho_{\rm SS}$ are initially driven and quickly oscillate, while $\rho_{\rm AA}$ slowly fills due to relaxation.

the case of the larger symmetry breaking (2 ns compared to 4 ns). This remains the case even for increasingly large symmetry breaking.

5.3.3.2 The symmetric-antisymmetric basis

We now focus on the behavior of the two individual SQDs in this chaotic regime by looking at the probabilities that each SQD is excited (ρ_{22} and ρ_{33} respectively). In the absence of the MNP, with $\mu_1 = \mu_2 = 3.0\,\text{e·nm}$, $R_1 = R_2 = 13\,\text{nm}$, $\omega_1 = 2.5\,\text{eV}$ and $\omega_2 = \omega_1(1 + 10^{-8})$, and for a driving frequency in the chaotic regime ($\omega - \omega_1 = 0.75\,\text{meV}$), we see that the two SQDs beat out of phase (see Fig 5.7).

Due to the approximate symmetry between the dots, it is worthwhile to consider the symmetric and antisymmetric basis. We define the symmetric and antisymmetric states as

$$|\mathrm{S}\rangle = \frac{1}{\sqrt{2}}(|2\rangle + |3\rangle)$$
$$|\mathrm{A}\rangle = \frac{1}{\sqrt{2}}(|2\rangle - |3\rangle)\,.$$

With these definitions, we can calculate the density matrix components for these new basis states as,

$$\rho_{\mathrm{SS}} = \frac{1}{2}(\rho_{22} + \rho_{33} + \rho_{23} + \rho_{32})$$
$$\rho_{\mathrm{AA}} = \frac{1}{2}(\rho_{22} + \rho_{33} - \rho_{23} - \rho_{32})\,.$$

When the SQD1-SQD2 symmetry is unbroken, $|\mathrm{S}\rangle$ is coupled to the driving field, while $|\mathrm{A}\rangle$ remains uncoupled. However, there is coupling to the antisymmetric state by means of the relaxation matrix, $\Gamma(\rho)$. For example, the double exciton state, $|4\rangle$, relaxes into both the symmetric state and antisymmetric state with equal probabilities. This can be seen in the right-hand side of Figure 5.7. The symmetric state initially oscillates as the applied field drives the system, whereas the antisymmetric state slowly fills due to relaxation of $|4\rangle$, on a time scale corresponding to $\tau_1 = \tau_2 = 0.8\,\mathrm{ns}$.

In Figure 5.7, we see that initially, the system oscillates until damping causes it to begin to settle into a semi-stable steady state. At about $t = 1\,\mathrm{ns}$, the initial Rabi oscillations have damped out, ρ_{22} is nearly equal to ρ_{33}, and ρ_{SS} is nearly equal to ρ_{AA}. As the system continues to evolve, ρ_{33} begins to decrease sharply,

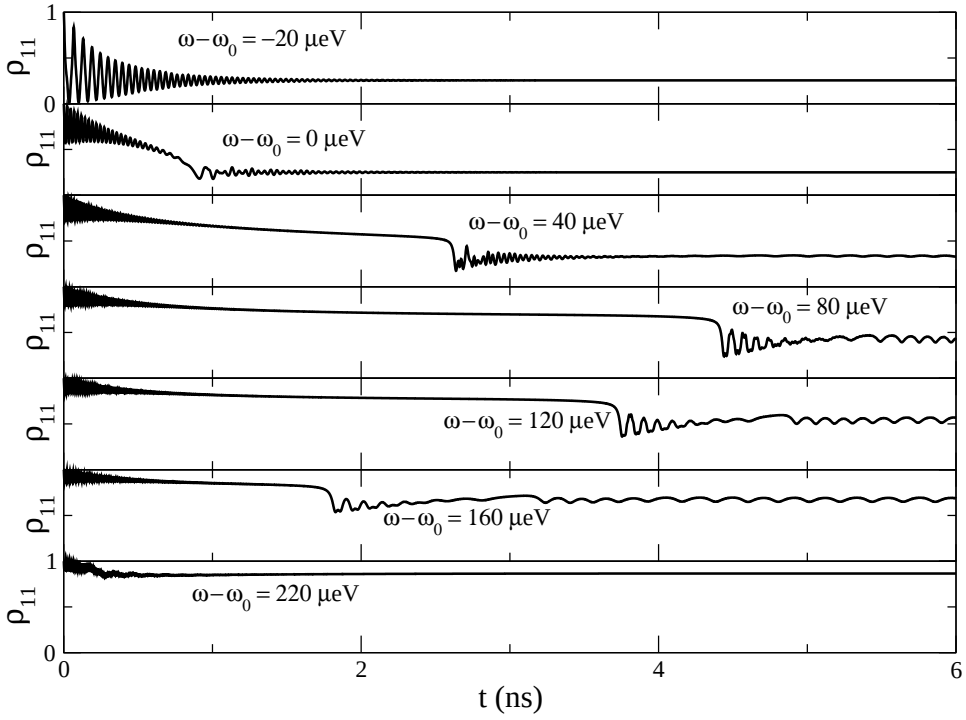

Figure 5.8: The secondary oscillations occur over a range of the applied frequencies ($\omega - \omega_0 = 0\,\mu$eV to $200\,\mu$eV, $\omega_0 \equiv \omega_1 = \omega_2$). The onset of the oscillations occurs sooner for frequencies near the end points of this window, reaching a maximum onset delay at approximately $\omega - \omega_0 = 80\,\mu$eV. In all cases the other system parameters and initial conditions are held fixed ($\mu_1 = 3.25\,\text{e·nm}$, $\mu_2 = 3.27\,\text{e·nm}$, $R_1 = R_2 = 13\,\text{nm}$, $\omega_0 = \omega_1 = \omega_2 = 2.5\,\text{eV}$)

while ρ_{22} starts to climb. Meanwhile, both ρ_{AA} and ρ_{SS} slowly increase. This eventually culminates in the oscillations occurring at $t \sim 2\,\text{ns}$. These oscillations eventually become regular as the system oscillates between two different steady states indefinitely. Returning to the a vs. μ parameter space (top of Figure 5.3) we see that the introduction of a small MNP ($a = 4\,\text{nm}$) to mediate the interaction is enough to quench the SQDs from beating.

When the degree of symmetry breaking is held fixed, and the system evolution is analyzed for particular values of the detuning inside the frequency range of chaotic

behavior, we see that the onset of the oscillations occurs sooner for frequencies near the end points of this window (see Figure 5.8). For $\mu_1 = 3.25\,\text{e·nm}$, $\mu_2 = 3.27\,\text{e·nm}$, $R_1 = R_2 = 13\,\text{nm}$, $\omega_0 \equiv \omega_1 = \omega_2 = 2.5\,\text{eV}$ the delay reaches a maximum of 4.5 ns at approximately $\omega - \omega_0 = 80\,\mu\text{eV}$. We also note that for detunings near this value, the magnitude of the oscillations is greater.

The maximum delay in the onset occurs at longer times for smaller symmetry breaking terms (see Figure 5.9). With $\mu_1 = 3.3\,\text{e·nm}$ and $\mu_2 = \mu_1(1 + 10^{-10})$, the onset can take up to 40 ns for particular values of the detuning. In fact, with $\mu_2 = \mu_1(1 + 10^{-n})$, the peak in the onset appears to increase linearly with n inside the chaotic regime. Over this range of n shown in the figure, $n = (2, 10)$, which covers 8 orders of magnitude in the symmetry breaking term, this relationship is found to be (including additional intermediate data points not shown in Figure 5.9 for clarity)

$$t_{onset}^{(max)} = \begin{cases} 1.08n + 0.11 & \text{for } \mu_1 = 3.0\,\text{e·nm}, \\ 1.66n - 0.62 & \text{for } \mu_1 = 3.1\,\text{e·nm}, \\ 4.23n - 4.15 & \text{for } \mu_1 = 3.3\,\text{e·nm}. \end{cases}$$

Thus, not only does onset increase linearly with increasing n, but it also increases with increased coupling strength (larger magnitude of μ_1, and thus μ_2). In addition to the increase in onset as the coupling strength increases, we also see that the detuning at which the peak in the onset occurs, shifts to higher energies for a fixed value of n. For example, with $n = 10$, the detuning where the peak is located shifts from $\omega - \omega_0 = 90\,\mu\text{eV}$ to $\omega - \omega_0 = 100\,\mu\text{eV}$, when μ_1 is increased from 3.0 e·nm

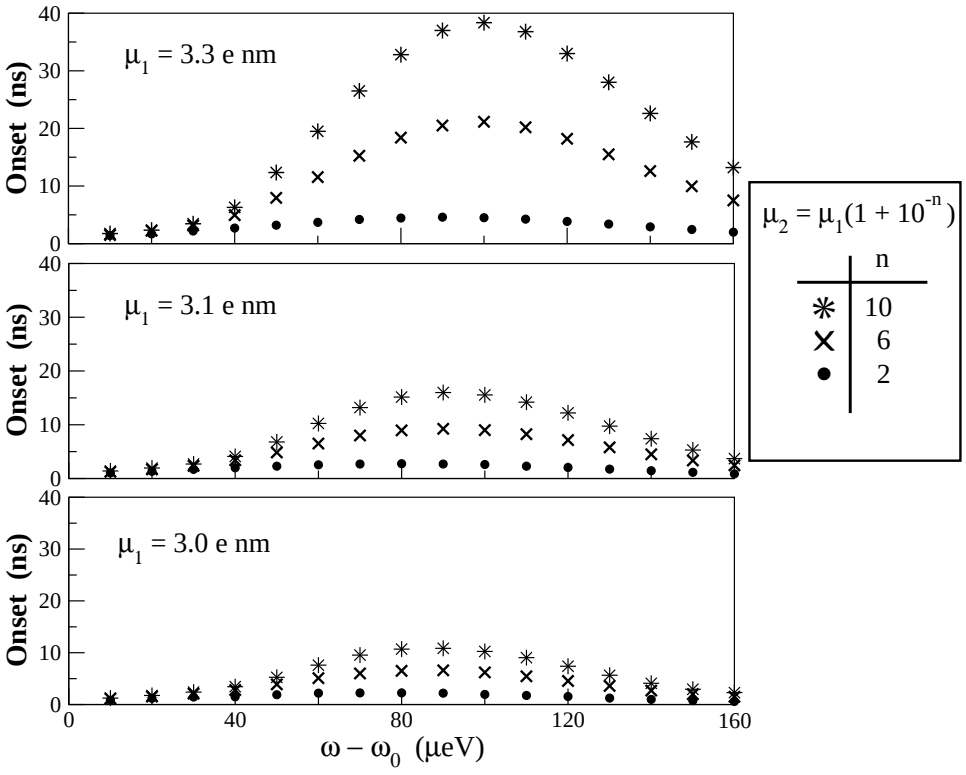

Figure 5.9: The onset of chaotic behavior as a function of detuning for three regimes of symmetry breaking, $\mu_2 = \mu_1 (1 + 10^{-n})$ with $n = \{2, 6, 10\}$, plotted for each of $\mu_1 = 3.0\,\mathrm{e{\cdot}nm}$ (bottom), $\mu_1 = 3.1\,\mathrm{e{\cdot}nm}$ (middle) and $\mu_1 = 3.3\,\mathrm{e{\cdot}nm}$ (top). For each of the three plots, we see that the delay in the onset increases as the magnitude of the symmetry breaking decreases. When the three plots are compared, the peak in the onset appears to shift to a larger detuning (from $\omega - \omega_0 = 90\,\mu\mathrm{eV}$ to $\omega - \omega_0 = 100\,\mu\mathrm{eV}$) as the magnitude of μ_1 (and thus μ_2) increases from $3.0\,\mathrm{e{\cdot}nm}$ to $3.3\,\mathrm{e{\cdot}nm}$.

to $3.3\,\mathrm{e{\cdot}nm}$.

This relationship between the degree of symmetry breaking and the delay in onset explains what we saw in Figure 5.5. There, we noticed that the plots on the right-hand side had a more regular behavior towards the middle of the frequency band that displays the chaotic behavior. However, in Figure 5.9, we see that detunings near these frequencies take much longer for the onset of chaotic behavior. In these cases, the initial semi-stable state that the system first evolves into is more

stable than for fields driving the system near the edges of the chaotic regime frequency window. Thus, a larger asymmetry must be built up in the system before the system can be knocked out of this semi-stable state, which accounts for this additional time.

Since the antisymmetric state is a higher energy state than the symmetric state, the location of the antisymmetric resonance is above the bare resonance and is in fact in this chaotic region. Since the interaction term between the two SQDs is $\hbar F$ times the transition dipole moment operator, we can estimate the splitting between the symmetric and antisymmetric state to be $2\hbar F \langle \mu \rangle$. For $\mu_1 = 3.25\,\mathrm{e{\cdot}nm}$, $\mu_2 = 3.27\,\mathrm{e{\cdot}nm}$, $R_1 = R_2 = 13\,\mathrm{nm}$, this splitting is approximately $100\,\mu\mathrm{eV}$, so we expect the antisymmetric mode to be around $\omega - \omega_1 = 50\,\mu\mathrm{eV}$ which is very close to the location of the maximum delay in the onset of secondary oscillations. However, energy splitting and level repulsion between quantum levels is obviously a quantum effect, thus we can expect that the semiclassical approximation for the SQD-SQD coupling breaks down here.

5.4 Towards A More Quantum Mechanical Approach

Previously, we took the single SQD relaxation matrix as a basis to construct the two-particle relaxation matrix in order to model the interaction with the bath. If we define the Lindblad operator as

$$\mathcal{L}(\hat{A}, \hat{B}) \equiv \hat{A}\rho\hat{B}^\dagger - \frac{1}{2}\left(\hat{B}^\dagger\hat{A}\rho + \rho\hat{B}^\dagger\hat{A}\right), \tag{5.6}$$

then this method is equivalent to taking 4 Lindblad terms, namely, relaxation of SQD1, $\mathcal{L}(\hat{a}_1, \hat{a}_1)$, relaxation of SQD2, $\mathcal{L}(\hat{a}_2, \hat{a}_2)$, dephasing of SQD1, $\mathcal{L}(\hat{a}_1^\dagger \hat{a}_1, \hat{a}_1^\dagger \hat{a}_1)$, and dephasing of SQD2, $\mathcal{L}(\hat{a}_2^\dagger \hat{a}_2, \hat{a}_2^\dagger \hat{a}_2)$. However, since we are treating the SQDs to be very closely separated and very near to each other in resonance, they can both in effect interact with the same bath. For example, both dots would interact with the same photon modes. As a consequence, spontaneous decay into these modes should occur due to the coherent response of the two dots (superradiance). Thus, there are two other Lindblad terms that we should consider, $\mathcal{L}(\hat{a}_1, \hat{a}_2)$ and $\mathcal{L}(\hat{a}_2, \hat{a}_1)$, i.e., a bath-induced interaction between the two dots. If we allow the two SQDs to interact with the same bath mode, then this should also be reflected in our Hamiltonian.

5.4.1 Quantum Mechanical SQD-SQD Coupling

We now instead use the quantum mechanical expression for the coupling between the two dots [65]. Our Hamiltonian is then

$$\begin{aligned}
\mathcal{H}_{total} =& \hbar\omega_1 \hat{a}_1^\dagger \hat{a}_1 + \hbar\omega_2 \hat{a}_2^\dagger \hat{a}_2 \\
&- 2\hbar \cos\omega t \; \Omega_1 \left(\hat{a}_1 + \hat{a}_1^\dagger\right) - 2\hbar \cos\omega t \; \Omega_2 \left(\hat{a}_2 + \hat{a}_2^\dagger\right) \\
&- \hbar G_1(\rho_{12} + \rho_{21} + \rho_{34} + \rho_{43}) \left(\hat{a}_1 + \hat{a}_1^\dagger\right) \\
&- \hbar G_2(\rho_{13} + \rho_{31} + \rho_{24} + \rho_{42}) \left(\hat{a}_2 + \hat{a}_2^\dagger\right) \\
&- \hbar F_{\mathrm{QM}}(\rho_{12} + \rho_{21} + \rho_{34} + \rho_{43}) \left(\hat{a}_2 + \hat{a}_2^\dagger\right) \\
&- \hbar F_{\mathrm{QM}}(\rho_{13} + \rho_{31} + \rho_{24} + \rho_{42}) \left(\hat{a}_1 + \hat{a}_1^\dagger\right) \\
&+ \hbar\delta(\hat{a}_1^\dagger \hat{a}_2 + \hat{a}_2^\dagger \hat{a}_1)
\end{aligned}$$

where G and Ω terms are defined as before and F_{QM} is defined as

$$F_{\mathrm{QM}} = \frac{\gamma a^3 \mu_1 \mu_2 s_\alpha^2}{4\pi\epsilon_{\mathrm{B}}\ \epsilon_{\mathrm{eff1}}\ \epsilon_{\mathrm{eff2}}\ \hbar R_1^3 R_2^3}\,. \tag{5.7}$$

δ was given previously as,

$$\begin{aligned}\delta =& \frac{3}{4\tau}\Bigg(\left(\cos^2(\theta) - 1\right) \frac{\cos(\zeta)}{\zeta} \\ &+ \left(1 - 3\cos^2(\theta)\right)\left(\frac{\cos(\zeta)}{\zeta^3} + \frac{\sin(\zeta)}{\zeta^2}\right)\Bigg)\end{aligned}$$

where $\zeta = \frac{\omega d}{c}$, c is the speed of light, and θ denotes the phase difference of the bath mode at the locations of the two molecules. We still use the semiclassical expression for the MNP mediated coupling between the dots (F_{QM}), but replace the direct coupling term with a quantum mechanical form.

To find the relaxation of the system, we now take a more complicated interaction Hamiltonian with the reservoir, $\mathcal{H}_{\mathcal{R}}$, of the form,

$$\begin{aligned}\mathcal{H}_{\mathcal{R}} =& \lambda_1 \hat{a}_1^\dagger \hat{b}_1 + \lambda_2 \hat{a}_1 \hat{b}_1^\dagger + \lambda_3 \hat{a}_2^\dagger \hat{b}_2 + \lambda_4 \hat{a}_2 \hat{b}_2^\dagger \\ &+ \lambda_5 \hat{a}_1^\dagger \hat{a}_1 \hat{b}_1^\dagger \hat{b}_1 + \lambda_6 \hat{a}_2^\dagger \hat{a}_2 \hat{b}_2^\dagger \hat{b}_2 \\ &+ \lambda_7 (\hat{a}_1^\dagger + \hat{a}_2^\dagger)\hat{c} + \lambda_8 (\hat{a}_1 + \hat{a}_2)\hat{c}^\dagger,\end{aligned} \tag{5.8}$$

where the $\hat{b}_i$'s are the operators for the internal bath of each SQD respectively (for example, coupling to the internal phonon modes of each dot), the $\hat{c}$ operators denote the bath processes that are common to both SQDs, and λ_i's are yet to be determined constants. The first 4 terms represent the non-collective portion of spontaneous emission and excitation, due to a possible symmetry breaking between the two particles as well as optical phonons inside each SQD. The next two terms

are due to scattering and give rise to pure dephasing. We imagine this process to be dominated by acoustic phonon-electron coupling[64] within each SQD separately, and thus treat it completely non-collectively. The final two terms represent the collective portion of spontaneous emission and excitation.

From equation (5.8), we make 6 Lindblad terms, ignoring those generated by $\hat{a}_1^\dagger$ and $\hat{a}_2^\dagger$, as they would represent bath induced excitation and we are imagining our bath to be at a much lower temperature than needed to induce an excitation at the optical energy scale. We can now write our relaxation matrix as

$$\begin{aligned}-\Gamma =&\frac{1}{\tau_1}\mathcal{L}(\hat{a}_1,\hat{a}_1)+\frac{1}{\tau_2}\mathcal{L}(\hat{a}_2,\hat{a}_2)+\frac{1}{T_1}\mathcal{L}(\hat{a}_1^\dagger\hat{a}_1,\hat{a}_1^\dagger\hat{a}_1)\\&+\frac{1}{T_2}\mathcal{L}(\hat{a}_2^\dagger\hat{a}_2,\hat{a}_2^\dagger\hat{a}_2)+\frac{1}{\tau_c}\mathcal{L}(\hat{a}_1+\hat{a}_2,\hat{a}_1+\hat{a}_2).\end{aligned}$$

τ_c is the collective decoherence and can be calculated with molecular QED. For two identical particles with a spontaneous decay rate $\frac{1}{\tau}$, then we find τ_c as

$$\begin{aligned}\tau_c =&\frac{2\tau}{3}\Bigg(1-\left(\cos^2(\theta)\right)\frac{\sin(\zeta)}{\zeta}\\&+\left(1-3\cos^2(\theta)\right)\left(\frac{\cos(\zeta)}{\zeta^2}-\frac{\sin(\zeta)}{\zeta^3}\right)\Bigg),\end{aligned}$$

with ζ and θ as before.

5.4.2 Numerical Results

Solving the master equation (5.4) with our quantum interaction Hamiltonian, we find that the system no longer exhibits the behavior of the chaotic regime. For example, with $\mu_1 = 3.0\,\mathrm{e{\cdot}nm}$, $\mu_2 = \mu_1(1+10^{-3})$, $R_1 = R_2 = 13\,\mathrm{nm}$, and a=0, the system shows a broad, smooth response (see Figure 5.10). However, these parameter

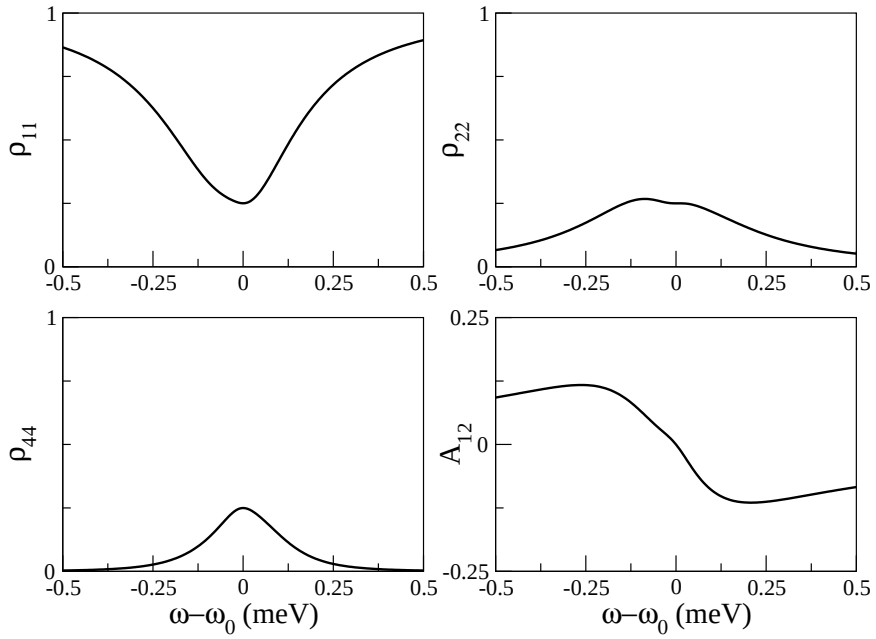

Figure 5.10: Density matrix for a quantum mechanical coupling between the dots. In this model, the chaotic regime disappears. $\mu_1 = 3.0\,\mathrm{e{\cdot}nm}$, $\mu_2 = \mu_1(1 + 10^{-3})$, $R_1 = R_2 = 13\,\mathrm{nm}$, $\omega_0 \equiv \omega_1 = \omega_2$ and a=0. Compare to the plot in the upper left-hand side of Figure 5.5.

values lead to the chaotic behavior in the semiclassical approach, as shown in the upper left plot in Figure 5.5. The chaotic behavior does not emerge even when a larger value of μ_1 is used or when the symmetry breaking is made arbitrarily large. This remains true even when the decoherence is treated completely non-collectively, as it was in the last section.

Also in Figure 5.10, we notice that the response in ρ_{11} and ρ_{22} (similarly ρ_{33}) is much more broad than that of ρ_{44}. Additionally, whereas ρ_{11} and ρ_{44} both appear to reach a resonance value near $\omega - \omega_0 = 0$, ρ_{22} has two peaks (similarly for ρ_{33}), one above and one below the frequency $\omega = \omega_0$. The reason for this asymmetry of the density matrix elements is that when a quantum mechanical coupling is used for the interaction between the two dots, this introduces a splitting between the two

singly excited states. Thus, the symmetric and antisymmetric states have different energy eigenvalues, with the symmetric being below the bare resonance, and the antisymmetric being at a higher energy than the bare resonance. This feature of the quantum mechanical coupling gives rise to a dipole blockade, which is absent in the semiclassical model, which we examine here.

5.4.3 Dipole Blockade

As the strength of the dipole-dipole coupling between the SQDs is increased (either by decreasing their separation or increasing their respective dipole moments), the symmetric (antisymmetric) eigenstate shifts to a lower (higher) energy. Thus, each of the single exciton states is further detuned from the bare resonance. However, the doubly excited state remains located at the bare resonance. Therefore, if the system is driven at this frequency, $\omega = \omega_0$, the excitation of the singly excited states would be suppressed owing to their respective detuning. This loss of population in the symmetric and antisymmetric states then results in an increase in the ground and doubly excited states, in the steady state limit. Conversely, if the system is driven near the symmetric or antisymmetric mode, then the doubly excited state, being detuned from this frequency, would be suppressed. This suppression of the doubly excited state due to the increased occupation of the single excited states is often referred to as a dipole blockade.

To expand on the idea of dipole blockade, we first consider the probability for each of the SQDs to be excited. From the density matrix, we can say that

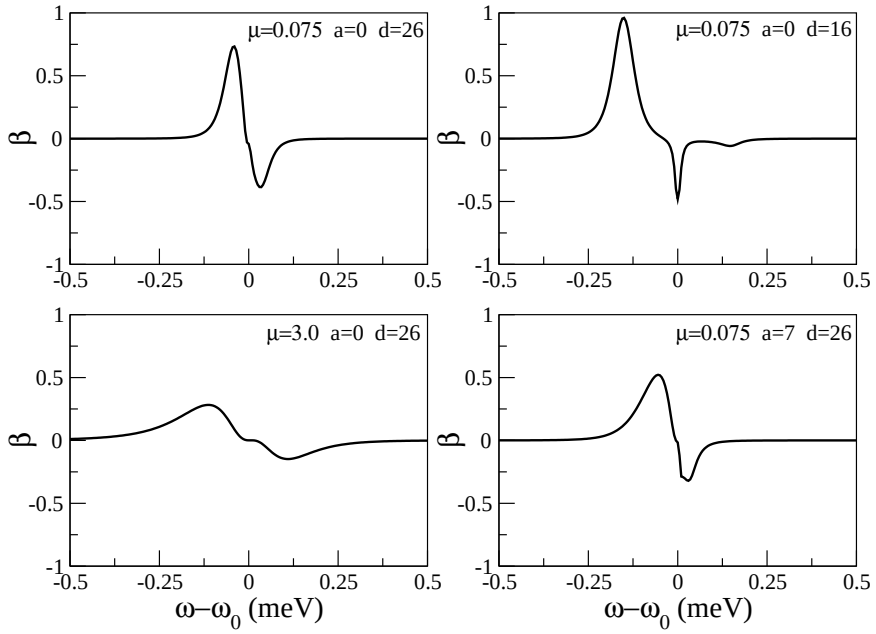

Figure 5.11: Dipole blockade measure, β, as a function of the detuning for various values of system parameters. Blockade increases with decrease in dot-to-dot separation (increased coupling) and decreases with response broadening (increased couping to the driving field or MNP). ($\omega_0 \equiv \omega_1 = \omega_2$)

$(\rho_{22} + \rho_{44})$ is the probability that SQD1 is excited and $(\rho_{33} + \rho_{44})$ is the probability that SQD2 is excited. Thus, we expect the product of these two probabilities to be approximately equal to the probability that both SQDs are excited at the same time, and therefore equal to ρ_{44}. The difference between these two probabilities can then be used as a measure of how suppressed or enhanced excitation of the double excited state is. To quantify the degree of dipole blockade in the system, we define the following measure, β,

$$\beta \equiv 9 * ((\rho_{22} + \rho_{44})(\rho_{33} + \rho_{44}) - \rho_{44}) \,. \tag{5.9}$$

The factor of 9 in the definition of β is chosen so that with full blockade, i.e., $\rho_{44} = 0$,

at saturation ($\rho_{11} = \rho_{22} = \rho_{33} = \frac{1}{3}$), $\beta = 1$. This is essentially the maximum value of β in the steady state limit (without population inversion). Conversely, if the interaction between the dots is strong enough, then their resonances will be shifted with respect to their bare resonances. In such a case, with the driving field near the bare SQD resonance, the excitation of a single SQD, ρ_{22} and ρ_{33}, will be suppressed relative to ρ_{44} and $\beta < 0$. In the actual calculations performed, values of $\beta < -0.5$ were rare.

When we plot β for various values of the system parameters, we find that blockade increases when the SQD-SQD separation is decreased as expected (see Figure 5.11). The stronger coupling between the dots increases the splitting between the two levels. For a detuning near the symmetric mode resonance, that mode is much more likely to be filled than the antisymmetric state, which is at a much higher energy. Thus double excitation of the dots is suppressed. When coupling to the driving field is increased (by increasing μ) or coupling to the MNP is increased (by increasing a), the SQD response broadens, providing more overlap between the two single exciton states and thus decreasing the dipole blockade.

5.4.4 Comparison in the Weak SQD-SQD Coupling Regime

When there is strong SQD-SQD coupling, the semiclassical and quantum approaches produce very different results. However, when the direct coupling between the SQDs is weaker, the detuning of the symmetric and antisymmetric states is smaller. Furthermore, in the presence of an MNP, the coupling mediated by the

plasmons can become more significant than the direct coupling between the SQDs. It is then expected that two approaches would be more in agreement in this regime.

In Figure 5.12, we plot the results of the two models in the regime with weak SQD-SQD coupling ($\mu_1 = \mu_2 = 0.5\,\mathrm{e{\cdot}nm}$), and strong SQD-MNP coupling ($a = 7\,\mathrm{nm}$, $R_1 = R_2 = 13\,\mathrm{nm}$). Shown for each model are the diagonal density matrix elements of the symmetric/antisymmetric basis ($\rho_{11}, \rho_{\mathrm{SS}}, \rho_{\mathrm{AA}}, \rho_{44}$) and the blockade measure, β. Also shown are the real and imaginary parts of the transition dipole moment of the symmetric state, μ_{SS}, which we calculate as $\mu_{\mathrm{SS}} = \rho_{1\mathrm{S}} + \rho_{\mathrm{S}1} + \rho_{\mathrm{S}4} + \rho_{4\mathrm{S}}$.

When the two models are compared (top vs bottom of Figure 5.12), we see similarities between the semiclassical and quantum models in the general shape of the predicted responses. However, there is significant deviation between the two models as well. In particular, the semiclassical approach does not account for the dipole blockade that occurs in the quantum model. Even with weak SQD-SQD coupling, dipole blockade can still have a significant impact on system behavior. This leads to noted differences between the two models in the regions just above and below the SQD bare resonance, where β reaches extreme values.

In the quantum model, the differences highlighted in Figure 5.12 are most notable in the slight splitting shown in ρ_{11}, very sharp peak of ρ_{44} and the enhancement in ρ_{SS} that occurs just below the SQD bare resonance. These effects are due to dipole blockade. In the case of ρ_{SS}, this enhancement is just the location of the symmetric eigenstate. Interestingly, ρ_{AA} is also peaked at this same energy and appears to be identical to ρ_{SS}. However, the reason that $\rho_{\mathrm{SS}} = \rho_{\mathrm{AA}}$ in the steady state limit is simply due to mixing between the symmetric and antisymmetric modes from the

interaction with the bath. Note that there is no corresponding peak in the response of the system above resonance where the antisymmetric eigenstate is located. This is because the antisymmetric state is not coupled to the driving field. When the system is driven near this frequency, the only single exciton state coupled to the driving field is the symmetric mode, which is far detuned in this case. Thus, the double exciton state, being closer in resonance with the driving field, is enhanced compared to ρ_{SS}. Thus $\beta < 0$ above resonance.

5.5 Conclusions

In this chapter, we have studied the response of a hybrid nanostructure molecule consisting of two SQDs coupled to a centrally located MNP, driven by an applied electric field. We have focused on identifying and addressing the issues in modeling such a system. Using a semiclassical approach to model the coupling between the SQDs can lead to unstable, oscillatory and chaotic behavior in a strong SQD-SQD coupling regime. This nonlinear behavior was shown to be due to a breaking of the identical particle symmetry. Additionally, we saw that this chaotic behavior is closely related to the type of decoherence present in the system, specifically, whether the decoherence is collective or non-collective between the two SQDs. We then modeled the system using a quantum mechanical expression for the SQD-SQD coupling, and saw that this instability in the response is absent. Whereas in the semiclassical model, a large SQD-SQD coupling lead to a chaotic response, in the quantum mechanical model, strong SQD-SQD coupling produced a large splitting between the

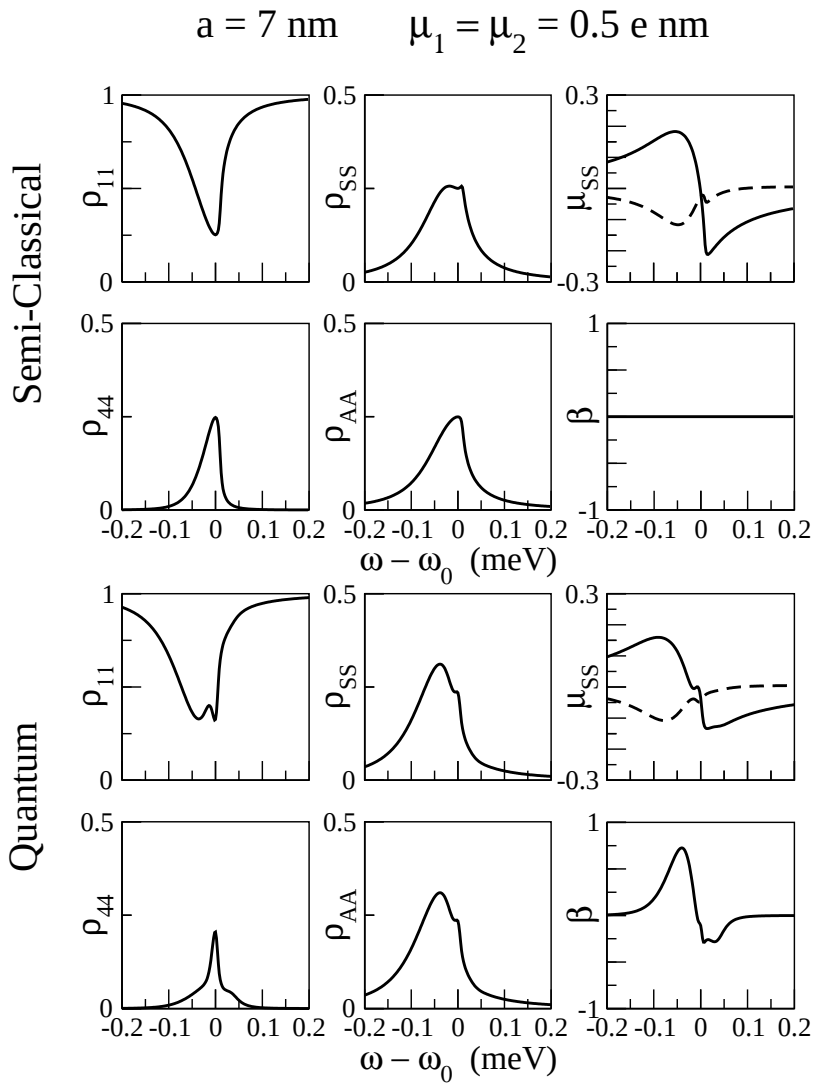

Figure 5.12: Comparison of semiclassical model (top 6 plots) and quantum model (bottom 6 plots) in the regime with weak SQD-SQD coupling ($\mu_1 = \mu_2 = 0.5\,\mathrm{e{\cdot}nm}$), and *strong* SQD-MNP coupling ($a = 7\,\mathrm{nm}$, $R_1 = R_2 = 13\,\mathrm{nm}$). Shown are the diagonal density matrix elements ($\rho_{11}, \rho_{\mathrm{SS}}, \rho_{\mathrm{AA}}, \rho_{44}$) and the blockade measure, β. Also shown are the real (solid line) and imaginary (dotted line) parts of the transition dipole moment of the symmetric state, $\mu_{\mathrm{SS}} = \rho_{1\mathrm{S}} + \rho_{\mathrm{S}1} + \rho_{\mathrm{S}4} + \rho_{4\mathrm{S}}$.

two single exciton states. We then compared the two models on a system with a strong plasmon mediated interaction between the SQDs and a weak direct interaction between them. In this case, we found that while the results of the two models were similar, dipole blockade and the level splitting of the single exciton states in the quantum model are non-trivial effects even in this regime.

Chapter 6

Concluding Remarks

In this thesis, we have studied hybrid systems consisting of SQDs and MNPs. Coupling the sharp, discrete resonance of the SQD to the broad continuum of plasmonic modes supported by the MNP with an applied driving field near the exciton resonance, should provide for dramatic signatures in the system response. We have developed theory to identify these signatures. Furthermore, the ability of MNPs to perform subwavelength confinement of light (in the form of plasmons), MNPs are a promising candidate to facilitate the directed transport of excitations and/or quantum information transfer between adjacent SQDs (or other types of quantum emitters). Our results address the physics that underlies this paradigm.

To exploit this paradigm for quantum, nanoscale transport and communication, one needs to understand how MNPs act as nanoantennas and nanoguides. One must understand the coupling between the exciton of the SQD and plasmons in the MNP. One must also understand how SQD-to-SQD quantum communication is modified by transfer via plasmons. Finally, one must understand how transfer is further modified if the metal nanoparticles are small and quantum effects can influence their response. In this thesis we have focused primarily on the effects of coupling between the SQDs and the MNPs.

Realization of nanostructures composed of SQDs and MNPs for use in nanode-

vices will require accurate theoretical models, which can predict the hybrid system response. Once these models are built, one can then use them to understand how the coupling introduced between these nano-objects, alters and modifies the behavior of each. By examining the conditions which cause different phenomena to emerge, one could then predict regions of parameter space which best exhibit novel properties of interest.

In this work, we have investigated the modification to the optical response of SQD-MNP and SQD-MNP-SQD hybrid systems. In particular, we probed the parameter space of these systems and identified a rich spectrum of phenomena: the nonlinear Fano effect, exciton induced transparency, suppressed SQD response, and bistability. We then located the regions of parameter space that lead to these distinct regimes of system behavior and set bounds on each. By considering the regions of parameter space where these phenomena occur, we were then able to deduce what causes them to emerge.

We showed how constructive and destructive interference of the local fields, internal to the system, with the external fields driving the hybrid structure is central in determining the system response. Using this knowledge, we then looked at how we could generalize these results to similar systems and more complicated structures. We then saw that this knowledge could be exploited to engineer hybrid systems, by tuning the SQD size and resonance, as well as the MNP geometry, to enhance or to bias the system response towards a particular, desired behavior. Specifically, we found that local field enhancement from nanorods can provide easier access to strong SQD-MNP coupling regimes.

The effect of MNP size, shape and SQD placement was analyzed to determine the regimes where the local multipolar response becomes significant. We identified regimes where dark modes and higher order multipolar modes could influence hybrid response. Strong, local field coupling via dark modes changes the interference and self-interaction effects dramatically. External fields do not directly drive this MNP dark mode, so SQD-MNP coupling is dominated by the local induced self-coupling. Coupling to higher order modes could be critical for long-range excitation transfer between different SQDs coupled to a nanorod.

To build realistic models that could allow for the simulation of hybrid nanostructures, we employed many techniques. We examined a number of different approximation techniques, and discussed the assumptions and implications of each. Furthermore, we employed these approximations in various coupling regimes and compared the results against models which utilize differing methods. Such checks of consistency allowed us to test the validity of our models in various limits. In particular, we saw that while a dipole approximation was sufficient to model the response of a spherical MNP with a radius that is small compared to interparticle separation, for larger spherical MNPs or elongated nanorods or wires, a more complete approach was needed. This consideration led us to use a full electrodynamical calculation, using the boundary element method to determine the local induced field produced by a nanorod. In the SQD-MNP-SQD system, we identified further issues in modeling such a system. Specifically, we saw that modeling the coupling between the SQDs semiclassically could lead to unstable and oscillatory behavior in the steady state. This chaotic behavior which arises in the semiclassical model, required a quantum

mechanical model to properly account for the coupling between the SQDs.

6.1 Looking Ahead

Work is now in progress to improve upon the models developed in this thesis. Specifically, the exact quantum nature of the SQD-MNP interaction is being explored by treating the plasmon quantum mechanically. Such quantum mechanical corrections to the semiclassical SQD-MNP model would become important for a number of reasons. For one, very small metallic structures will begin to confine the plasmons. Recently, it has been shown that even MNPs as large as 10 nm in diameter will begin to exhibit plasmon resonances which diverge from values predicted classically due to a change in particle permittivity in the quantum regime [66]. Further reducing the MNP size will eventually lead to the appearance of sharp, distinct modes replacing the broad continuous response of larger MNPs [61, 62]. Perhaps more importantly, a quantum mechanical treatment of the plasmons is necessary if we wish to investigate corrections introduced by quantum mechanical coupling for the SQD-MNP interaction. For example, the quantum nature of exciton-plasmon-exciton conversion (for either transfer between SQDs or the self-interaction of an SQD) determines the loss of quantum information that occurs in the process.

Recently, several theoretical investigations have gone beyond the semiclassical limit in studying SQD/MNP hybrids by treating the plasmon-exciton interaction with quantum mechanical methods, such as treating the plasmon in the quasi-mode formalism commonly employed in cavity QED [58, 59], or by using Green's function

techniques [67]. In the quasi-mode method, the plasmon is modeled as a single, broad, effective mode which couples to the exciton. This mode is then often traced out of the problem by invoking the very fast nature of the plasmon relaxation (compared to the relatively long lived exciton). However, in certain situations, this large hierarchy of time scales might not hold. In fact, since metallic nanostructures can have large Purcell factors, close proximity of the SQD can greatly enhance the emission rate of the exciton, by as much as a few orders of magnitude or more. This can reduce the range of time scales of the system interactions, and could lead to a more coherent coupling between SQD and MNP. Such a system would provide for fast excitation transfer, and a reduction in the loss of quantum information.

Currently, work is being done to build more advanced models to more accurately predict SQD-MNP and SQD-MNP-SQD hybrid behavior in the case where the quantum nature of the coupling is important. These models treat the plasmons in a quantum mechanical manner with a quasi-mode approach. Rather than trace over the plasmon mode, which assumes a non-coherent exciton-plasmon coupling, we retain the plasmon mode in the problem and determine the evolution of both the exciton and plasmon states. The evolution of the system is calculated using a quantum trajectory method [68], in which a system's evolution is governed by a non-Hermitian, effective Hamiltonian, and spontaneous decay is simulated by Monte Carlo-determined "quantum jumps". By treating the exciton-plasmon coupling fully quantum mechanical, one should be able to answer questions that necessitate a coherent exciton-plasmon coupling. The work presented in this thesis has been an integral component in the building of these models.

Bibliography

[1] R. P. Feynman. There's plenty of room at the bottom. *Eng. Sci.*, 23:22–36, 1960.

[2] G. Binnig, H. Rohrer, Ch. Gerber, and E. Weibel. Surface studies by scanning tunneling microscopy. *Phys. Rev. Lett.*, 49:57–61, Jul 1982.

[3] Eigler D. M. and Schweizer E. K. Positioning single atoms with a scanning tunneling microscope. *Nature*, 344:524–526, 1990.

[4] H. W. Kroto, J. R. Heath, S. C. O'Brien, R. F. Curl, and R. E. Smalley. C$_60$: Buckminsterfullerene. *Nature*, 318(6042):162–163, November 1985.

[5] HW Kroto. The stability of the fullerenes cn, with n= 24, 28, 32, 36, 50, 60 and 70. *Nature*, 329(6139):529–531, 1987.

[6] Sumio Iijima. Helical microtubules of graphitic carbon. *Nature*, 354(6348):56–58, November 1991.

[7] W.K. Leutwyler, S.L. Bürgi, and HB Burgl. Semiconductor clusters, nanocrystals, and quantum dots. *Science*, 271:933, 1996.

[8] L. Bányai and S.W. Koch. *Semiconductor quantum dots*, volume 2. World Scientific Publishing Company Incorporated, 1993.

[9] D.L. Fedlheim and C.A. Foss. *Metal nanoparticles: synthesis, characterization, and applications*. CRC, 2001.

[10] K.L. Kelly, E. Coronado, L.L. Zhao, and G.C. Schatz. The optical properties of metal nanoparticles: the influence of size, shape, and dielectric environment. *The Journal of Physical Chemistry B*, 107(3):668–677, 2003.

[11] S.H. Yu, M. Antonietti, H. Cölfen, and J. Hartmann. Growth and self-assembly of bacro4 and baso4 nanofibers toward hierarchical and repetitive superstructures by polymer-controlled mineralization reactions. *Nano Letters*, 3(3):379–382, 2003.

[12] J. Barauskas, M. Johnsson, and F. Tiberg. Self-assembled lipid superstructures: beyond vesicles and liposomes. *Nano letters*, 5(8):1615–1619, 2005.

[13] J. Lee, A.O. Govorov, and N.A. Kotov. Bioconjugated superstructures of cdte nanowires and nanoparticles: Multistep cascade förster resonance energy transfer and energy channeling. *Nano letters*, 5(10):2063–2069, 2005.

[14] Christian Gruber, Primoz Kusar, Andreas Hohenau, and Joachim R. Krenn. Controlled addressing of quantum dots by nanowire plasmons. *Applied Physics Letters*, 100(23):231102, 2012.

[15] T. Pons, I.L. Medintz, K.E. Sapsford, S. Higashiya, A.F. Grimes, D.S. English, and H. Mattoussi. On the quenching of semiconductor quantum dot photoluminescence by proximal gold nanoparticles. *Nano Lett.*, 7(10):3157–3164, 2007.

[16] A.V. Akimov, A. Mukherjee, C.L. Yu, D.E. Chang, A.S. Zibrov, P.R. Hemmer, H. Park, and M.D. Lukin. Generation of single optical plasmons in metallic nanowires coupled to quantum dots. *Nature*, 450(7168):402–406, 2007.

[17] Y. Fedutik, V. V. Temnov, O. Schops, U. Woggon, and M. V. Artemyev. Exciton-plasmon-photon conversion in plasmonic nanostructures. *Phys. Rev. Lett.*, 99(13):136802, 2007.

[18] H. Mertens, J.S. Biteen, H.A. Atwater, and A. Polman. Polarization-selective plasmon-enhanced silicon quantum-dot luminescence. *Nano Lett.*, 6(11):2622–2625, 2006.

[19] Alberto G. Curto, Giorgio Volpe, Tim H. Taminiau, Mark P. Kreuzer, Romain Quidant, and Niek F. van Hulst. Unidirectional emission of a quantum dot coupled to a nanoantenna. *Science*, 329(5994):930–933, 2010.

[20] Wei Zhang, Alexander O. Govorov, and Garnett W. Bryant. Semiconductor-metal nanoparticle molecules: Hybrid excitons and the nonlinear fano effect. *Phys. Rev. Lett.*, 97(14):146804, 2006.

[21] Ryan D. Artuso and Garnett W. Bryant. Optical response of strongly coupled quantum dotmetal nanoparticle systems: Double peaked fano structure and bistability. *Nano Lett.*, 8(7):2106–2111, June 2008.

[22] Ryan D. Artuso and Garnett W. Bryant. Strongly coupled quantum dot-metal nanoparticle systems: Exciton-induced transparency, discontinuous response, and suppression as driven quantum oscillator effects. *Phys. Rev. B*, 82(19):195419, Nov 2010.

[23] Jie-Yun Yan, Wei Zhang, Suqing Duan, Xian-Geng Zhao, and Alexander O. Govorov. Optical properties of coupled metal-semiconductor and metal-molecule nanocrystal complexes: Role of multipole effects. *Phys. Rev. B*, 77(16):165301, Apr 2008.

[24] SM Sadeghi. Tunable nanoswitches based on nanoparticle meta-molecules. *Nanotechnology*, 21:355501, 2010.

[25] A. Govorov, G. Bryant, W. Zhang, T. Skeini, J. Lee, N. Kotov, J. Slocik, and R. Naik. Exciton-plasmon interaction and hybrid excitons in semiconductor-metal nanoparticle assemblies. *Nano Lett.*, 6(5):984–994, 2006.

[26] Mu-Tian Cheng, Shao-Ding Liu, Hui-Jun Zhou, Zhong-Hua Hao, and Qu-Quan Wang. Coherent exciton-plasmon interaction in the hybrid semiconductor quantum dot and metal nanoparticle complex. *Opt. Lett.*, 32(15):2125–2127, 2007.

[27] R. Esteban, T. V. Teperik, and J. J. Greffet. Optical patch antennas for single photon emission using surface plasmon resonances. *Phys. Rev. Lett.*, 104(2):026802, Jan 2010.

[28] J. Lindberg, K. Lindfors, T. Setälä, and M. Kaivola. Dipole-dipole interaction between molecules mediated by a chain of silver nanoparticles. *J. Opt. Soc. Am. A*, 24(11):3427–3431, 2007.

[29] S M Sadeghi, L Deng, X Li, and W-P Huang. Plasmonic (thermal) electromagnetically induced transparency in metallic nanoparticle–quantum dot hybrid systems. *Nanotechnology*, 20(36):365401, 2009.

[30] M. Liu, T.W. Lee, S.K. Gray, P. Guyot-Sionnest, and M. Pelton. Excitation of dark plasmons in metal nanoparticles by a localized emitter. *Phys. Rev. Lett.*, 102(10):107401, 2009.

[31] Mark L. Brongersma, John W. Hartman, and Harry A. Atwater. Electromagnetic energy transfer and switching in nanoparticle chain arrays below the diffraction limit. *Phys. Rev. B*, 62(24):R16356–R16359, Dec 2000.

[32] D. E. Chang, A. S. Sørensen, P. R. Hemmer, and M. D. Lukin. Quantum optics with surface plasmons. *Phys. Rev. Lett.*, 97(5):053002, Aug 2006.

[33] A. Gonzalez-Tudela, D. Martin-Cano, E. Moreno, L. Martin-Moreno, C. Tejedor, and F. J. Garcia-Vidal. Entanglement of two qubits mediated by one-dimensional plasmonic waveguides. *Phys. Rev. Lett.*, 106:020501, Jan 2011.

[34] E. Altewischer, M. P. van Exter, and J. P. Woerdman. Plasmon-assisted transmission of entangled photons. *Nature*, 418(6895):304–306, 2002.

[35] Sylvain Fasel, Franck Robin, Esteban Moreno, Daniel Erni, Nicolas Gisin, and Hugo Zbinden. Energy-time entanglement preservation in plasmon-assisted light transmission. *Phys. Rev. Lett.*, 94(11):110–501, 2005.

[36] Giuliana Di Martino, Yannick Sonnefraud, Stephane Kena-Cohen, Mark Tame, Sahin K. Ozdemir, M. S. Kim, and Stefan A. Maier. Quantum statistics of surface plasmon polaritons in metallic stripe waveguides. *Nano Letters*, 12(5):2504–2508, 2012.

[37] Oriane Mollet, Serge Huant, Géraldine Dantelle, Thierry Gacoin, and Aurélien Drezet. Quantum plasmonics: Second-order coherence of surface plasmons launched by quantum emitters into a metallic film. *Phys. Rev. B*, 86:045401, Jul 2012.

[38] Ryan D. Artuso, Garnett W. Bryant, Aitzol Garcia-Etxarri, and Javier Aizpurua. Using local fields to tailor hybrid quantum-dot/metal nanoparticle systems. *Phys. Rev. B*, 83:235406, Jun 2011.

[39] Michael Faraday. The bakerian lecture: Experimental relations of gold (and other metals) to light. *Philosophical Transactions of the Royal Society of London*, 147:145–181, 1857.

[40] Gustav Mie. Beiträge zur optik trüber medien, speziell kolloidaler metallösungen. *Annalen der Physik*, 330(3):377–445, 1908.

[41] L. Rayleigh. On the scattering of light by small particles. *Philosophical Magazine*, 41(275):447–451, 1871.

[42] R. H. Ritchie. Plasma losses by fast electrons in thin films. *Physical Review*, 106:874–881, June 1957.

[43] J.D. Jackson and R.F. Fox. Classical electrodynamics. *American Journal of Physics*, 67:841, 1999.

[44] Matthew Pelton and Garnett W. Bryant. *Introduction to Metal-Nanoparticle Plasmonics*. John Wiley and Sons, New York, 2013.

[45] F. Assous, P. Degond, E. Heintze, P.A. Raviart, and J. Segre. On a finite-element method for solving the three-dimensional maxwell equations. *Journal of Computational Physics*, 109(2):222 – 237, 1993.

[46] G. Mur. Absorbing boundary conditions for the finite-difference approximation of the time-domain electromagnetic-field equation. *IEEE Trans. Electromag. Compat.*, 23(4):377–382, 1981.

[47] F. J. Garcia de Abajo and A. Howie. Relativistic electron energy loss and electron-induced photon emission in inhomogeneous dielectrics. *Phys. Rev. Lett.*, 80:5180–5183, Jun 1998.

[48] A. Yariv. *Quantum Electronics*. John Wiley and Sons, New York, 1975.

[49] C. Gardiner and P. Zoller. *Quantum Noise*. Springer-Verlag, Berlin Heidelberg, 2004.

[50] G. Lindblad. On the generators of quantum dynamical semigroups. *Communications in Mathematical Physics*, 48:119–130, 1976. 10.1007/BF01608499.

[51] A. Kossakowski. On quantum statistical mechanics of non-hamiltonian systems. *Reports on Mathematical Physics*, 3(4):247 – 274, 1972.

[52] Hongxing Xu, Xue-Hua Wang, Martin P. Persson, H. Q. Xu, Mikael Käll, and Peter Johansson. Unified treatment of fluorescence and raman scattering processes near metal surfaces. *Phys. Rev. Lett.*, 93(24):243002, Dec 2004.

[53] M Durach, A Rusina, V I Klimov, and M I Stockman. Nanoplasmonic renormalization and enhancement of coulomb interactions. *New Journal of Physics*, 10(10):105011, 2008.

[54] L.D. Landau, E.M. Lifshitz, and L.P. Pitaevskii. *Electrodynamics of Continuous Media*. Butterworth-Heinemann Ltd, Oxford, 1984.

[55] P. B. Johnson and R. W. Christy. Optical constants of the noble metals. *Phys. Rev. B*, 6(12):4370–4379, Dec 1972.

[56] K. L. Silverman, R. P. Mirin, S. T. Cundiff, and A. G. Norman. Direct measurement of polarization resolved transition dipole moment in ingaas/gaas quantum dots. *Applied Physics Letters*, 82(25):4552–4554, 2003.

[57] T. H. Stievater, Xiaoqin Li, D. G. Steel, D. Gammon, D. S. Katzer, D. Park, C. Piermarocchi, and L. J. Sham. Rabi oscillations of excitons in single quantum dots. *Phys. Rev. Lett.*, 87(13):133603, Sep 2001.

[58] A. Ridolfo, O. Di Stefano, N. Fina, R. Saija, and S. Savasta. Quantum plasmonics with quantum dot-metal nanoparticle molecules: Influence of the fano effect on photon statistics. *Phys. Rev. Lett.*, 105:263601, Dec 2010.

[59] Edo Waks and Deepak Sridharan. Cavity qed treatment of interactions between a metal nanoparticle and a dipole emitter. *Phys. Rev. A*, 82:043845, Oct 2010.

[60] David Dzsotjan, Anders S. Sørensen, and Michael Fleischhauer. Quantum emitters coupled to surface plasmons of a nanowire: A green's function approach. *Phys. Rev. B*, 82:075427, Aug 2010.

[61] E. Prodan and P. Nordlander. Exchange and correlations effects in small metallic nanoshells. *Chemical Physics Letters*, 349(12):153 – 160, 2001.

[62] Emily Townsend and Garnett W. Bryant. Plasmonic properties of metallic nanoparticles: The effects of size quantization. *Nano Letters*, 12(1):429–434, 2012.

[63] Peng Song, Peter Nordlander, and Shiwu Gao. Quantum mechanical study of the coupling of plasmon excitations to atomic-scale electron transport. *The Journal of Chemical Physics*, 134(7):074701, 2011.

[64] J. Förstner, C. Weber, J. Danckwerts, and A. Knorr. Phonon-assisted damping of rabi oscillations in semiconductor quantum dots. *Phys. Rev. Lett.*, 91:127401, Sep 2003.

[65] R. H. Lehmberg. Radiation from an n-atom system. i. general formalism. *Phys. Rev. A*, 2:883–888, Sep 1970.

[66] J.A. Scholl, A.L. Koh, and J.A. Dionne. Quantum plasmon resonances of individual metallic nanoparticles. *Nature*, 483(7390):421–427, 2012.

[67] A. Manjavacas, F. J. Garcia de Abajo, and P. Nordlander. Quantum plexcitonics: Strongly interacting plasmons and excitons. *Nano Letters*, 11(6):2318–2323, 2011.

[68] M. B. Plenio and P. L. Knight. The quantum-jump approach to dissipative dynamics in quantum optics. *Rev. Mod. Phys.*, 70:101–144, Jan 1998.